Toward an Atom Laser: Cold Atoms in a Long, High-gradient Magnetic Guide

by

Rahul Ramdas Mhaskar

A dissertation submitted in partial fulfillment
of the requirements for the degree of
Doctor of Philosophy
(Applied Physics)
in The University of Michigan
2008

Doctoral Committee:

Professor Georg A. Raithel, Chair
Professor Paul R. Berman
Professor Bradford G. Orr
Professor Duncan G. Steel
Professor Kim A. Winick

This work is dedicated to my parents Sarita and Ramdas Mhaskar and to Trupti Sonavane,
without whose encouragement, this would have been infinitely hard.

ACKNOWLEDGEMENTS

I would like to acknowledge all the people who have contributed to my success and encouraged me through my research, provided joyous and thoughtful moments and talked me through the days of being a labrat, and sometimes a slacker. First of all, I would like to thank Georg Raithel for his excellent guidance, seemingly infinite patience and the funding he has provided me, and most of all for the wisdom and knowledge of physics that he shared with me. It would be no exaggeration to say that he transformed into a scientist and a physicist capable of independent thought and research and gave me the tools to help me succeed. I would like to thank Jeff Guest and Kevin Teo for their mentoring at the beginning of my research career. Alisa Walz-Flannigan, Natalya Morrow and David Feldbaum helped me get familiarized with the lab when I first started my research. I would like to thank Tara Cubel-Liebisch for being a friend and a mentor throughout my time at the lab. I would like to acknowledge my labmates Brenton Knuffman, Rui Zhang, Aaron Reinhard, Rachel Sapiro, Kelly Younge and Andrew Schwarzkopf for the thoughtful discussions and various lab tips, tricks, treats and good times that we shared together. It has been a pleasure working with Cornelius Hempel, Varun Vaidya and Mallory Traxler on this project over the last year. Varun's help has been much appreciated during the setup of the new lab. Cornelius has been and continues to be one of the best friends I have had, and I think have learned a lot more from him regarding worldly matters. With the experiment in Mallory's hands now, I'm sure she will fulfill the

goals the experiment was made for. I would like to thank Spencer Olson for the his friendship, mentoring and guidance. I learned much from him from the time we spent setting up the experiment, taking data and analyzing the results, as well as from the computer knowledge he tried to impart to me. This project owes its existence to the dedication and efforts he put into it.

Saving the best for the last, I would like to thank my parents Sarita and Ramdas Mhaskar, and to Trupti Sonavane. I owe much of my success to their love and encouragement, to the joys they gave me and the difficult times they shared with me, though separated by thousands of miles. To them I dedicate this thesis.

This project received financial support from Office of Naval Research, the Army Research Organization, the National Science Foundation center for Frontiers in Coherent and Ultrafast Science (FOCUS) and the Physics Department at the University of Michigan. I would like to thank the Applied Physics Program at the University of Michigan for funding through my sixth semester.

TABLE OF CONTENTS

CHAPTER

LIST OF TABLES

Table

LIST OF FIGURES

Figure

LIST OF SYMBOLS

δ	Laser detuning from atomic transition	57
δ_D	Doppler detuning	57
δ_l	Laser detuning from an unperturbed atomic transition	62
δ_{total}	Laser detuning from atomic transition including electric/magnetic field perturbations and Doppler shift	56
Γ_{scat}	Scattering rate	56
$\left\lvert\vec{\mathbf{B}}\right\rvert$	Magnitude of local magnetic field	59
μ_B	Bohr magneton = 1.4 MHz-G $^{-1}$	58
ω_0	Unperturbed atomic transition angular frequency.	
ω_a	Atomic transition angular frequency in presence of perturbing fields.	
ω_{field}	Atomic transition angular frequency shift in presence of perturbing fields.	
ω_l	Laser angular frequency	57
τ	Excited state lifetime	56
$\vec{\mathbf{k}}_l$	Laser wave-vector	56
$\vec{\mathbf{v}}_a$	Velocity of an atom	57
F_{rad}	Radiation force	56
g_F	Electron gyromagnetic ratio a hyperfine manifold $\lvert F\rangle$	58
I_{sat}	Saturation intensity of atomic transition	57
s_0	Saturation parameter	57
v_{recoil}	Recoil velocity	56

ABSTRACT

The propagation of an atomic beam through a 1.7 m long magnetic guide with magnetic field gradient of up to 2.7 kGauss-cm^{-1} has been demonstrated. The guide is side-loaded with an atomic beam from a Pyramidal MOT Low-velocity Intense Source. The atomic beam observed at the end of the guide has a flux of 3×10^7 atoms-s^{-1} with a velocity of 1.2 m/s, a transverse temperature of 420 ± 40 μK and a longitudinal temperature of 1 mK. The guided atomic beam was mode-filtered by selective removal of high-energy atoms using radio-frequency coupling to magnetically untrapped states. We found that the phase-space density of the atomic beam was very low for evaporative cooling to be functional.

An imaging technique was developed to characterize the guided atomic flow in the presence of a high magnetic field gradient. This technique utilizes the open-channel transition to obtain nearly constant photon yield per atom independent of the location of the atom in the guide, providing a mapping of the fluorescence images to the atomic-density profiles. This technique was theoretically studied using Quantum Monte-Carlo Simulations and validated.

A Zeeman slower was constructed and characterized to be used as the primary source of atoms to the magnetic guide. The Zeeman slower output atomic beam has a flux of 3×10^{11} atoms-s^{-1} at a velocity of 40 m/s. We have designed a new injection scheme to transfer atoms from the Zeeman slower to the magnetic guide efficiently. The details of a new method to evaporatively cool atoms in the magnetic guide using surface adsorption are described. Finally, a new guide geometry based on a spiral structure is discussed.

CHAPTER I

Introduction

The discovery of quantum mechanics in the early twentieth century is widely regarded as the turning point in science and indeed the history of the world. Quantum mechanics brought with it ideas like non-locality, wave-particle duality and entanglement, which were difficult to grasp even by the most capable minds then. Even today, a deep understanding of quantum reality remains subject to interpretation. One of the core ideas of quantum mechanics is that all particles can be described as waves and vice versa. This wave-particle duality has some very interesting consequences. Just as light generates an interference pattern in the Young's double-slit experiment, even electrons, neutrons and atoms, which are particles in the classical sense, exhibit this interference pattern in a similar setup. Demonstration of such phenomenon, however, was limited to very small particles as those listed above, and was not observed in macroscopic systems for a long time. The realization of the Bose-Einstein condensate (BEC) in 1995 changed all that.

A BEC is a state of matter in which all particles occupy the same ground state of the confining potential. This state was first predicted by Satyendranath Bose using the statistics he developed to describe the thermodynamics of photons. This was later generalized by Albert Einstein to include all indistinguishable particles having an integral spin. Quantum mechanically, particles come in two flavors (not to be confused with QCD!). In an ensemble of particles, if exchanging two particles does not alter the state of the system, those particles are described by the Bose statistics. All integral spin particles such as photons, gravitons and atoms with an integral total spin, such as ^{87}Rb come under this category of Bosons. However, if exchanging two particles leads to a distinct state, those particles are described by the Fermi statistics. All the half-spin particles such as electrons, protons and neutrons are included in this category of Fermions. Thus, the BEC is an ensemble of atoms that can be described by a single wave-function having the dimensions of the ensemble of the constituent atoms, and has all the properties associated with a wave such as phase and coherence properties.

1.1 Atom Interferometers

Because the BEC behaves like a matter wave, it can interfere with itself. This fact has led to many proposals and implementations of atom interferometers. In atom interferometers, relative phase shifts of de Broglie matter waves can be utilized to measure atomic accelerations due to electromagnetic fields [1], gravitational fields [2], rotations [3], and interactions with other atoms [4, 5]. The recent surge of interest in atom interferometry stems from this wide range of potentially detectable phenomena and the associated high precision due to the short de Broglie wavelength of matter waves in the velocity range of interest ($\lesssim 1$ m/s to a few 10 m/s) [6]. In addition to this, atom interferometers can also be used to create a 3D holographic map of local electric and magnetic fields. One approach to build atom-interferometric devices is based on the use of magnetic atom guides, which provide narrow, conservative guiding potentials for cold atoms. In analogy with fiber-optic interferometers, which are commonly operated using lasers, guided-wave atom interferometers will presumably operate best with an atom source that injects a monochromatic continuous flow of cold atoms into the lowest transverse mode of the atom guide. However, just as white-light optical interferometry is possible using nearly matched optical path lengths, precise atom interferometry may be possible using a reasonably mono-energetic beam of atoms [7]. The second approach places some stringent requirements on the implementation of the atom interferometer. The sensitivity of an interferometer is proportional to the area enclosed by the interferometer. It is easiest to implement a large-area interferometer is the opening angle at the input beam-splitter is large, which while easy in guided beam interferometers, is not possible in atomic beam interferometers. Secondly, atomic beam interferometers rely on the fact that each atom interferes with itself. Thus the interference pattern is a stochastic average over many such individual interference patterns. This leads to a very weak contrast between the crest and the trough of the interferometer, thus decreasing the sensitivity. However, with a coherent atomic beam, the entire ensemble of atoms interferes with itself, resulting in contrast ratios approaching 100%. This boost in signal-to-noise ratio greatly increases the sensitivity of the interferometer. Interferometers using coherent matter wave pulses have been demonstrated before. However, they all suffer from phase instability issues due to mean-field pressure and finite size of the BEC. Hence, using an atom laser input to an atom interferometer would be represent a quantum leap toward the realization of increasingly sensitive sensors relying on interferometry.

1.2 Bose-Einstein Condensate

To understand how Bose statistics works, let us start with a mundane example of putting socks in drawers. If we want to arrange two pairs of socks, one red and one blue, in three drawers, there are 9 ways in which they can be arranged, as shown in the Figure 1.1. However, if both the pairs of socks are black, then there are only six arrangements. Thus, if we randomly place the two pair of socks in the three drawers, each arrangement of socks has a probability of 1/9 if the socks are distinguishable, in this case red and blue. But if the socks are indistinguishable, the probability that the socks end up in one of the arrangements is 1/6. Hence, we see that, even for a limited number of particles and limited number of states, the number of states is less if the particles are indistinguishable, making each state more probable. This is the principle behind Bose statistics. Translating that as socks being the particles trapped in a confining potential and drawers being the bound states of the potential, the particles are constantly rearranging themselves between the states due to collisions. For indistinguishable particles, the probability of occupying a particular state is high,

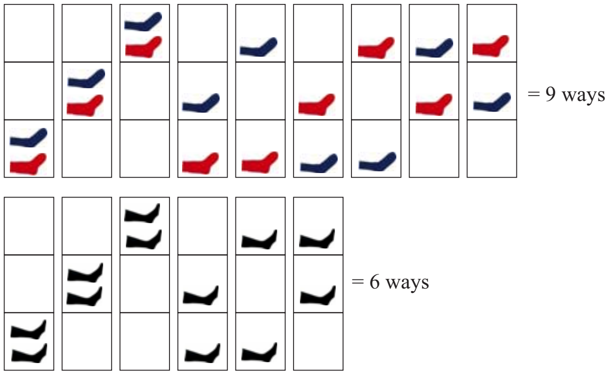

Figure 1.1: Arrangement of socks in drawers. This figure shows that there are 9 ways in which two pairs of distinguishable socks can be arranged in three drawers, as opposed to 6 ways in which indistinguishable pairs of socks can be arranged in three drawers. Thus for a large number of socks and drawers, the number of arrangements for distinguishable socks will be much larger than that for indistinguishable socks. Translated to particles and states, this is the principle behind Bose statistics.

as compared to distinguishable particles, because the density of states is very low. If the particles are occupying a few of the least energetic trap states, the probability that a collision will lead to one of the colliding atoms ending up in the ground state is proportional to $\sqrt{N+1}$ where N is the number of particles already occupying the ground state. This is known as the quantum enhancement of scattering probability into ground state, or Bosonic stimulation.

A BEC can be made in a number of different methods, using magnetic, optical or sometimes hybrid traps. However, the basic steps remain the same and are given below. In summary, atoms from background vapor at room temperature are collected and cooled in a Magneto-Optical Trap (MOT) to temperatures of a few hundred microKelvins. These atoms are then transferred to an trap which can either be a magnetic trap or an optical dipole trap. The trapped atoms are then compressed and evaporatively cooled. In the process of evaporative cooling, the hottest atoms in the trap are discarded. The remaining atoms rethermalize to lower temperature. This process is repeated, in conjunction with compressing the trap to increase the atomic density and make the rethermalization more efficient, until the BEC is achieved. These steps are explained in greater detail below.

1.2.1 Magneto-Optical Atom Trap (MOT)

The Magneto-Optical Trap (MOT) operates on the principle of optical pumping. A schematic of the MOT in 1D is shown in Figure 1.2. It consists of magnetic quadrupole field, such as that formed by two coils in an anti-Helmzoltz configuration, i. e. carrying current in opposite directions. Two counter-propagating laser beams are incident at the center of the quadrupole field, as shown in Figure 1.2 for the 1D case. The laser beams have a frequency ν_L which is detuned from the unperturbed atomic transition $|g = (J_g = 0, m_g = 0)\rangle \rightarrow |e = (J_e = 1)\rangle$ by δ_L. In presence of

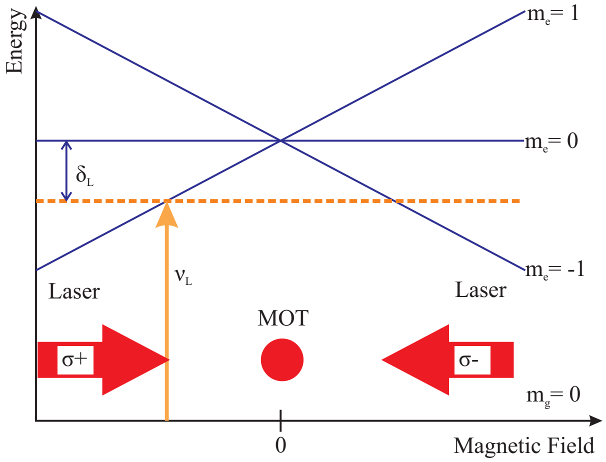

Figure 1.2: Schematic of the MOT in 1D. This figure shows Magneto-Optical Trap in a 1D configuration. The atoms are cooled and trapped near the magnetic field zero due to Zeeman shifts in the atomic transition in the inhomogeneous magnetic field, such that atoms to the right of the magnetic field zero scatter more σ^- light and are pushed toward the center of the trap.

the magnetic field, the excited state splits into three levels characterized by the m quantum number. For the field configuration shown in Figure 1.2, if an atom is moving away from the trap center on the left, for example, it sees the σ^+ polarized beam on resonance to the $|m_g = 0\rangle \rightarrow |m_e = +1\rangle$ transition due to the Zeeman shift in conjunction with the Doppler shift, and is pushed toward the trap center. At the same time, because the laser is red-detuned with respect to the unperturbed atomic resonance, the atoms are also slowed down due to Doppler cooling near the center of the trap. In 3D, the MOT both cools and localizes the atoms at the center of the quadrupole magnetic field.

1.2.2 Magnetic trapping of atoms

An atom has an intrinsic spin which is a vector sum of all the electronic and nuclear spins and the orbital angular momenta. This spin is quantized following the rules of angular momentum quantization. If an atom has a non-zero total quantized spin m, then it also has a magnetic moment associated with that spin: $\mu = gm\mu_B$, with g being the gyromagnetic ratio and μ_B being the Bohr magneton. Thus, the atom, in presence of a magnetic field $\vec{\mathbf{B}}$, possess a potential energy: $V_M = \vec{\mu} \cdot \vec{\mathbf{B}} = gm\mu_B|\vec{\mathbf{B}}|$. If the magnetic field is non-uniform, i.e. if $\nabla|\vec{\mathbf{B}}| \neq 0$, then the atom experiences a force: $\vec{\mathbf{F}}_M = -\vec{\nabla}V_M = -gm\mu_B\vec{\nabla}|\vec{\mathbf{B}}|$. Thus, if the product gm is positive, the force is opposite to the magnetic field gradient and the atom is pushed toward lower magnetic field and is said to be in a low-field seeking state. Conversely, using a similar argument, if the product gm is negative, the atom is said to be in a high field seeking state. This is a conservative force as there is no dissipation term involved.

This magnetic force can be used to trap atoms at a magnetic field minimum. Such a magnetic field can be generated in three dimensions using two coils in an anti-Helmholtz configuration, which is the same as used for a MOT. An atom can also be trapped in 2 dimensions in a 2D quadrupole field, such as that generated by two parallel wires carrying parallel currents. The Figure 1.3 shows the 2D magnetic quadrupole field generated by two parallel wires separates by 4 mm and carrying 300 A parallel currents. This gives a magnetic field gradient of 2.7 kGauss-cm^{-1} at the center, where the atoms are trapped. A profile of trapped atoms is overlayed on

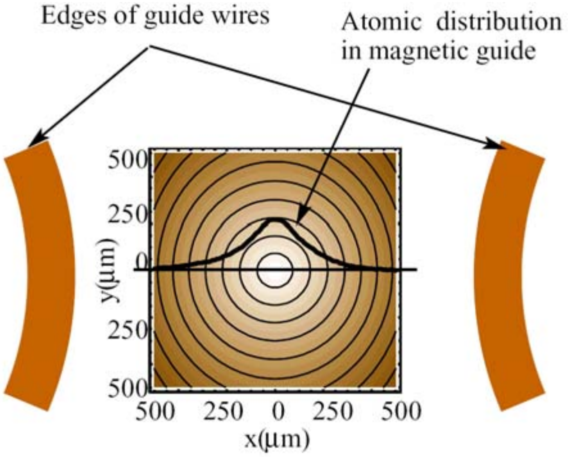

Figure 1.3: 2D quadrupole Magnetic field profile. This figure shows the 2D quadrupole magnetic field generated by two parallel wires spaces 4 mm apart, carrying parallel currents of 300 A. The resultant gradient is 2.7 kGauss-cm^{-1}. The contour lines in the figure at spaced 20 Gauss apart. A profile of atoms trapped in such a 2D quadrupole field is overlaid.

the magnetic field contour plot.

1.2.3 Evaporative cooling

The MOT is capable of cooling atoms only to Doppler temperature. At the Doppler temperature, the average velocity of the atoms is comparable to the velocity imparted by each photon scattering event, called the recoil velocity. Atoms pre-cooled in the MOT can be further cooled using sub-Doppler cooling processes such as Sisyphus cooling in an optical molasses [8]. Even then, the temperature of the atoms is too high for the BEC to form. Hence, an additional step of evaporative cooling has to be performed after optical molasses cooling. Evaporative cooling consists of discarding the most energetic atoms in the trap, as shown in Figure 1.4. The remaining atoms have a lower average energy and are hence cooler. The energy is redistributed due to collisions between the atoms such that some atoms again end up having significantly higher than average energy, which are again discarded. As the average energy of the atoms decreases, the threshold energy above which the atoms are discarded is also lowered, until all the atoms end up in the ground state of the trap.

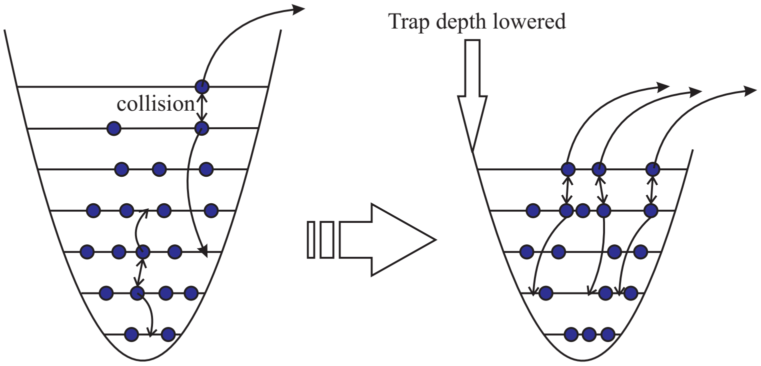

Figure 1.4: Evaporative cooling sequence. This figure illustrates the process of evaporative cooling. As atoms collide, they redistribute energy and the atoms with energies greater than trap depth are discarded. Thus, the average energy of the trapped atoms decreases and the ensemble is cooled. The trap depth is then decreased and the process repeats.

In magnetic traps, the trapped and non-trapped states can be coupled using radio-frequency electromagnetic fields. The frequency of the coupling field depends on the magnetic field strength, which in turn depends on the location inside the trap. Atoms with higher energy sample higher magnetic fields as they oscillate inside the trap, and thus an RF field with high frequency (usually tens of MHz) can couple these atoms to non-trapped states. In this sense, the trap depth can be defined in terms of the frequency of the RF field applied. Thus, introducing RF field with frequency chirped from high frequency to low frequency (usually hundreds of kHz), decreases the trap depth and thus leads to evaporative cooling.

The same mechanism can be achieved by using Raman transitions to couple the trapped and non-trapped states. In case of optical dipole traps, the trap laser intensity is decreased, thus lowering the trap depth. Evaporative cooling can also be implemented by bringing a dielectric surface close to the trap center, thus adsorbing the hottest atoms on the surface. This mechanism is discussed in more detail in Chapter VII.

1.3 Atom guide

There are two approaches toward realization of an atom laser. The first approach is to cool the atomic beam to the ground state of the 2D guiding potential. The second approach is to form a stationary BEC, replenish it using evaporatively cooled cold atoms, and out-couple it to form a coherent atomic beam, or an atom laser. The first approach, followed by a group at ENS in France [9–13] presents many conceptual difficulties. Firstly, how the longitudinal coherence will be set-up in such a scheme has not been shown either theoretiacally or experimentally. Secondly, in the presence of high collision rate, the transverse motion of the atomic beam will be coupled with the longitudinal motion, thus drastically decreasing the coherence length. It is not clear how the phase of such a beam will evolve and whether the atomic beam will be phase stable to be of any use at all. Hence, we have chosen to follow the second approach, as all the concepts involved in realizing that approach have been individually proven. The apparatus is designed such that all the steps involved in generating a BEC are implemented in a space-sequential manner, instead of the usual time-sequential manner.

In the frame of reference of the atoms propagating in the guide, all the processes happen in the same location, thus maintaining the equivalency of the two methods. A schematic of the design of an atom laser is shown in Figure 1.5. As in a time-sequential BEC generation process, we first start with a vapor-cell MOT, i.e. a MOT which collects and cools atoms from the background vapor. The atoms are then transferred to a 2D+ MOT, which is a 2D MOT with optical molasses action in the non-trapped dimension. The optical molasses is used to launch the atoms in a magnetic guide. The evaporative cooling is then implemented in the magnetic guide section, with a provision to get the BEC at the end of the guide. The atom laser is out-coupled from a stationary BEC which is continuously replenished. This leads to

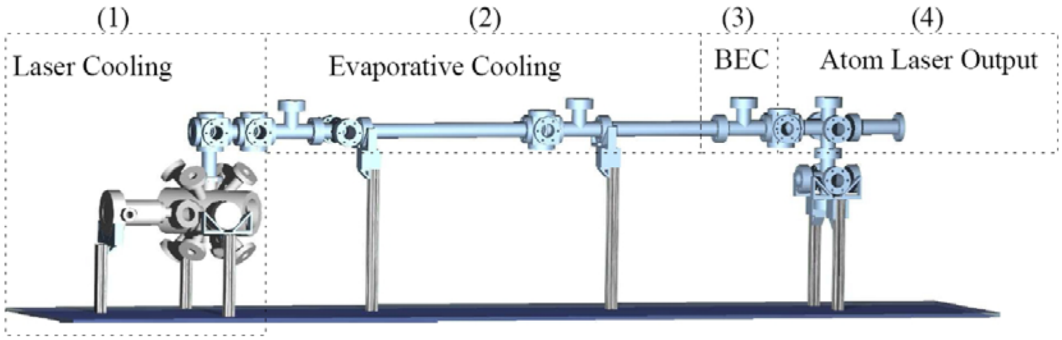

Figure 1.5: Time sequential BEC generation in an atom guide. This figure shows the schematic of the step used in generation of a BEC, applied in a space-sequential manner. The atoms are collected from background vapor and laser-cooled in section (1). They are then transferred to the magnetic guide in section (2) where they undergo evaporative cooling. A stationary BEC is formed in section (3) and output-coupled to an atom laser in section (4).

a phase-stable output, with high longitudinal coherence length.

1.4 Outline

The thesis is organized in the following manner. Chapter II describes the magnetic atom guide in detail, including the construction of the guide and the characterization of the guided atomic beam. Chapter III describes the method we devised to image the atomic beam in a manner so as to make the characterization of the atomic beam easier. Chapter V gives details of the Zeeman slower we implemented as an alternative high-flux source of slow atoms to the next generation of the atom guide. Finally, Chapter VII gives detailed plans regarding the implementation of the next generation of the guide.

CHAPTER II

Dark-state Injection of Atoms into Magnetic Guide

Tis chapter gives details of the high-gradient magnetic atoms guide we constructed to understand the magnetic guiding process and learn about the advantages and disadvantages of various techniques used to inject atoms into the guide and the guide itself. The setup reflects the steps utilized in making a Bose-Einstein Condensate in a time sequential manner. In this case, the process are separated in space, and the atoms travel through the processes, such as initial collection and cooling, optical pumping, transfer to the magnetic trap and evaporative cooling. Because we map the time sequence in space, we lose the ability to trap the atoms in one dimension, and hence a magnetically guided atomic beam apparatus is developed. The next section describes the experimental setup along with the constructional details of the guide. The scheme used to inject atoms from the atomic beam into the guide is described in Section 2.2. Gravitational slowing and magnetic compression of the atomic beam is detailed in Section 2.3.

2.1 Overview of the experimental setup

Our experimental setup consists of two laser-cooling stages that prepare atoms for a high-gradient magnetic atom guide. Atoms, first collected in a vapor-cell pyramidal magneto-optical trap (PMOT in Fig. 2.1), are transferred into and recaptured by a secondary MOT (MMOT in Fig. 2.1). This MMOT then injects the atoms into the 1.7 m long magnetic atom guide with a tunable velocity. As shown in Fig. 2.1, the guide is comprised of a vertical injection/launch section (about 0.2 m height) and a horizontal section (1.5 m length) in which RF-induced transitions are employed to selectively remove the most energetic atoms from the guided atomic flow.

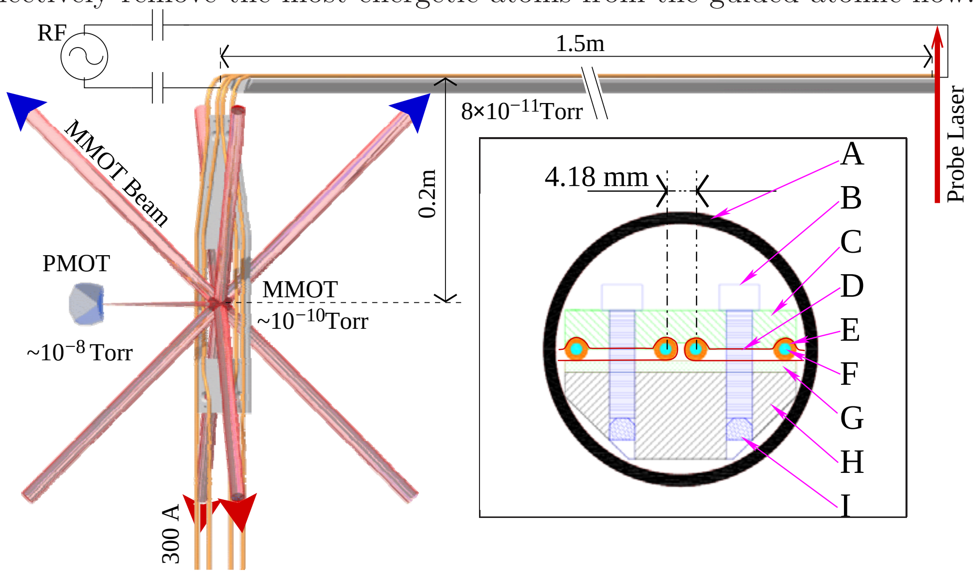

Figure 2.1: Sketch of the experimental setup. Atoms are injected from a pyramidal magneto-optical trap (PMOT) via a “Moving MOT” (MMOT) into the vertical injection/launch section of a magnetic atom guide. As the injected atomic flow rises upward, it slows under in the influence of gravity and becomes magnetically compressed. The flow then propagates into a long horizontal guide section. A radio-frequency current coupled into the horizontal guide section is used to remove the most energetic atoms from the guided atomic flow. The system has three differentially pumped vacuum regions, the values of which are shown here. The inset on the right shows a cross section through the horizontal section of the guide. (A) Vacuum chamber, (B) mounting screws, (C) aluminum spacers, (D) insulating Kapton film, (E) guide wires, (F) coolant, (G) alumina spacers, (H) guide rail, (I) lock screws.

The magnetic atom guide consists of a pair of in-vacuum hollow copper tubes with an outer diameter of 3.18 mm and a center-to-center separation as low as 4.18 mm. The copper tubes are introduced into the vacuum chamber through Swage-Lok feedthroughs with Teflon ferrules and are precision-mounted in the vacuum on a steel rail using alumina, aluminum spacers, and Kapton foil (see inset of Fig. 2.1). The mounts are designed such that a well-defined tube separation is achieved as a

Guide current	300 A
Field gradient (end of guide)	2.7 kG/cm
Dissipated power	3.2 kW
Cooling water pressure	120 PSI
Water inlet temperature	16^oC
Water temperature differential	30^oC
Vacuum pressure (horizontal guide region)	8×10^{-11} Torr

Table 2.1: Parameters of continuous-mode operation of the magnetic atom guide.

function of the longitudinal position in the magnetic guide. The aluminum-Kapton mounts are sufficiently loose so as to allow the tubes to slide longitudinally. This is necessary to provide relief for thermal expansion, which can be up to ~ 1 mm under normal operating conditions. The steel rail on which the guide tubes are mounted provides stability and rigidness to the structure. Long, periodic slots in this steel rail allow optical access to the region between the guide tubes. A precision machined rail surface minimizes washboard-like gravitational bumps along the length of the guide. The hollow guide tubes are cooled using a closed-circuit, high-pressure water flow. At a current of 300 A, the magnetic-field gradient reaches values of 2.7 kG/cm, generating accelerations of 90 g on ^{87}Rb atoms in the state $|F = 1, m_{\mathrm{F}} = -1\rangle$. The system is routinely operated using the continuous-mode parameters listed in Table 2.1.

2.2 Atomic-flow injection

2.2.1 Primary atomic beam: Side-loading the MMOT

The primary atomic beam used to load the atom guide is generated by the PMOT [14], a fluorescence image of which is shown in Fig. 2.2. Our PMOT, operated with a single laser beam of <2 MHz FWHM and 100 mW power, is a version of the MOT [15] that emits a cold atomic beam through a hole in the apex of a pyramidal mirror [16]. This is similar to a Low-Velocity Intense Source of atoms

(LVIS [17]). To initiate the atomic beam from the PMOT, the atom cloud in Fig. 2.2 is centered over the apex of the pyramid using a tunable bias magnetic field. The resultant imbalance in radiation pressure causes the atoms to be extracted through the indicated exit hole in form of a freely propagating atomic beam.

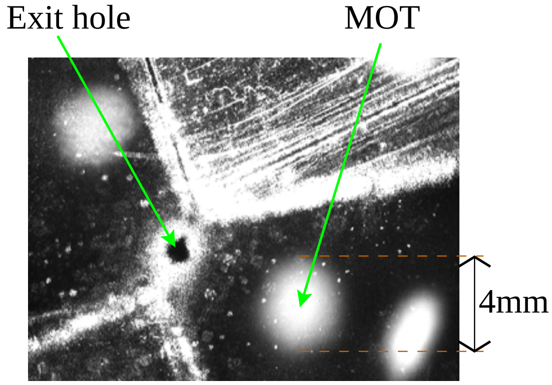

Figure 2.2: Primary pyramidal MOT (PMOT). The image shows the actual atom cloud and multiple reflections thereof in the pyramidal mirror.

To characterize the unguided beam emitted from the PMOT, we have performed a series of absorption measurements. As depicted in Fig. 2.3, a low-intensity ($\sim 0.15\, I_{\text{sat}}$ with saturation intensity $I_{\text{sat}} = 1.6\ \text{mW/cm}^2$), small-diameter, near-resonant probe beam was arranged to intersect the PMOT atomic beam at an angle $\theta = 45^o$ in the vicinity of the MMOT. The spatial profile of the PMOT atomic beam was determined by measuring the absorption for different vertical positions of the probe beam. To determine the velocity distribution, for each vertical position y the probe laser was scanned across the atomic absorption resonance, and the absorption was measured as a function of the laser frequency. Due to the Doppler effect, the laser detuning from resonance $\delta\nu$ and the velocity of the atoms v_{z} are approximately related by $\delta\nu = \cos\theta \frac{v_{\text{z}}}{\lambda}$. This allows us to plot the absorption due to the PMOT atomic beam as a function of vertical position and velocity. The data, shown in Fig. 2.4, yield an average velocity of the primary atomic beam $\langle v_{\text{z}} \rangle = 22$ m/s and a FWHM spread of Δv_{z} =16 m/s. The FWHM spread of the absorption signal in height is Δy =16 mm. Since the distance between the PMOT and the MMOT is about 16 cm, the full angular spread of the primary beam is about 100 mrad.

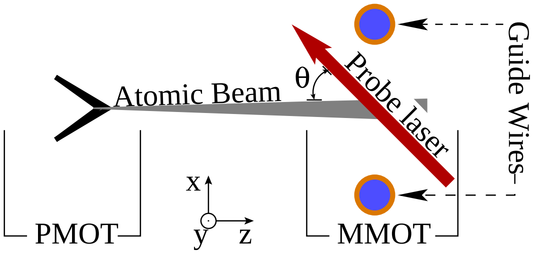

Figure 2.3: Setup for absorption measurement of LVIS beam. Setup of absorption measurement used in order to characterize the (un-guided) primary atomic beam emitted by the PMOT is shown. The current in the guide wires is turned off for this measurement.

The flux Φ_{PMOT} of the atomic beam is determined as follows. In the limit of weak absorption, the absolute power $dP(y,\nu_{\mathrm{L}})$ absorbed by the PMOT atomic beam from the small probe beam is given by

$$\begin{aligned} dP(y,\nu_{\mathrm{L}}) &= -h\nu \int_{-\infty}^{\infty} N(y,v_{\mathrm{z}})\gamma(v_{\mathrm{z}},\nu_{\mathrm{L}})dv_{\mathrm{z}} \\ &= -h\nu \int_{-\infty}^{\infty} N(y,v_{\mathrm{z}})\frac{\Gamma}{2}\left(\frac{I/I_{\mathrm{sat}}}{1+4\left(\frac{2\pi\delta}{\Gamma}\right)^2}\right)dv_{\mathrm{z}} \end{aligned} \tag{2.1}$$

where ν_{L} is the laser frequency, γ is the velocity- and frequency-dependent photon scattering rate, Γ is the line width ($2\pi \times 6$ MHz), I is the laser intensity, and $I_{\mathrm{sat}} = 1.6\,\mathrm{mW/cm^2}$. $N(y,v_{\mathrm{z}})$ is the number of atoms in the probe beam per velocity element dv_{z} at height y. The dependence of dP on ν_{L} is contained in the atom-field detuning δ seen by the atoms,

$$\delta = \frac{\cos(\theta)}{\lambda}v_{\mathrm{z}} + \nu_0 - \nu_{\mathrm{L}} \tag{2.2}$$

where ν_0 is the un-shifted frequency of the atomic transition. Noting that the probe-beam diameter is much smaller than the atomic-beam diameter, the fractional absorption $dP(y,\nu_\mathrm{L})/P$ is

$$\begin{aligned}\frac{dP(y,\nu_\mathrm{L})}{P} &= -\frac{h\nu_\mathrm{L}\Gamma}{2I_\mathrm{sat}}\int_{-\infty}^{\infty}\left(\frac{N(y,v_\mathrm{z})}{A}\right)\frac{1}{1+4\left(\frac{2\pi\nu_\mathrm{s}}{\Gamma}\right)^2}dv_\mathrm{z}\\ &= -\frac{h\nu_\mathrm{L}\Gamma}{2I_\mathrm{sat}}\int_{-\infty}^{\infty}\left(\frac{n_\mathrm{A}(y,v_\mathrm{z})}{\sin(\theta)}\right)\frac{1}{1+4\left(\frac{2\pi\nu_\mathrm{s}}{\Gamma}\right)^2}dv_\mathrm{z}\end{aligned} \tag{2.3}$$

where A is the probe-beam cross section and $n_\mathrm{A}(y,v_\mathrm{z})$ is the number of atoms per area element $dydz$ and per velocity element dv_z, *i.e.* n_A has units of $\mathrm{m}^{-2}(\mathrm{m/s})^{-1}$. Using the reasonable assumption that $n_\mathrm{A}(y,v_\mathrm{z})$ does not vary much over the velocity range over which the second factor under the integral in Eq. 2.3 is significant, we may replace $n_\mathrm{A}(y,v_\mathrm{z})$ by $n_\mathrm{A}(y,v_\mathrm{R})$, where

$$v_\mathrm{R} = \frac{\lambda}{\cos\theta}(\nu_\mathrm{L}-\nu_0) \tag{2.4}$$

is the velocity of atoms for which the probe laser beam is on-resonant,*i.e.* for which $\delta = 0$ in Eq. 2.2. The integral can then be calculated, yielding

$$n_\mathrm{A}(y,v_\mathrm{R}) = -\frac{dP(y,\nu_\mathrm{L}(v_\mathrm{R}))}{P}\frac{4I_\mathrm{sat}\sin(2\theta)}{hc\Gamma^2} \tag{2.5}$$

Denoting the peak absorption by $\left(\frac{dP}{P}\right)_0$ and the peak value of n_A by n_0, it is $n_0 = -\left(\frac{dP}{P}\right)_0\frac{4I_\mathrm{sat}\sin(2\theta)}{hc\Gamma^2}$. Noting that the volume density of atoms $n_\mathrm{V} \approx n_0\Delta v_\mathrm{z}/\Delta x$, and assuming that the PMOT atomic beam is symmetric about its axis (*i.e.* the FWHM spreads of the atomic beam $\Delta x = \Delta y$), the estimated atomic flux is

$$\begin{aligned}\Phi_\mathrm{PMOT} &\approx n_\mathrm{V}\,\Delta x\,\Delta y\,\langle v_\mathrm{z}\rangle = n_0\Delta v_\mathrm{z}\Delta y\langle v_\mathrm{z}\rangle\\ &= -\frac{4I_\mathrm{sat}}{hc\Gamma^2}\left(\frac{dP}{P}\right)_0\Delta v_\mathrm{z}\Delta y\langle v_\mathrm{z}\rangle \quad ,\end{aligned} \tag{2.6}$$

where $\theta = \pi/4$ has been used. Using the measurement result $\left(\frac{dP}{P}\right)_0 = -0.22\%$ and the above values for the average velocity, the velocity spread and the height of the

PMOT beam, we find $\Phi_{\mathrm{PMOT}} \approx 3 \times 10^9\ \mathrm{s}^{-1}$. Due to the approximations made in the analysis, we expect the result to be accurate to within 30% of the stated value. It was also observed that the flux for higher PMOT laser powers was higher. For example, a PMOT laser power of 130 mW resulted in a flux of around $5.3 \times 10^9 \mathrm{s}^{-1}$.

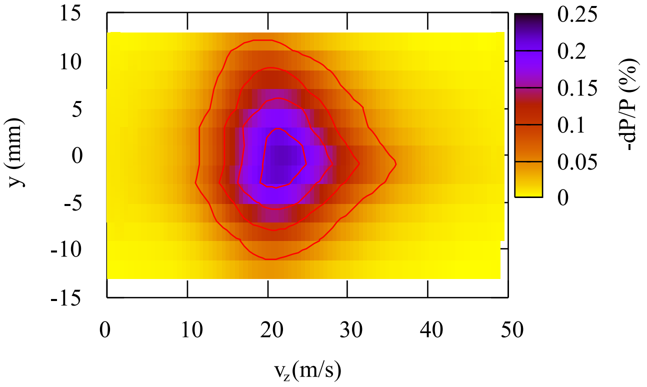

Figure 2.4: Absorption measurement of LVIS atomic beam. This figure shows a contour plot of the relative absorption $-dP/P$ due to the primary atomic beam as a function of vertical position y and velocity v_{z}.

2.2.2 Injection into the magnetic guide

The atomic beam emitted by the PMOT propagates into the differentially pumped UHV ($\sim 10^{-10}$ Torr) section of the setup that contains the vertical portion of the atom guide. As seen in Fig. 2.1, the horizontal atomic beam emitted by the PMOT side-loads the vertical injection/launch section of the atom guide at a right angle. The injection into the guide is accomplished using a “Moving MOT” (MMOT [9, 10]). As shown in Fig. 2.1, the four coplanar copper tubes that provide the magnetic guiding fields throughout most of the apparatus also create the two-dimensional magnetic quadrupole field necessary for the MMOT. The inner tubes are spaced at a center-to-center distance $a_1 = 3.7$ cm and carry parallel currents, while the outer tubes are spaced at a distance $a_2 = 5.7$ cm and provide the current return-path. For a current of $I = 300$ A, the radially symmetric field gradient near the guide axis,

$$\frac{\partial B}{\partial \rho} = \frac{4\mu_0 I}{\pi}\left[\frac{1}{a_2^2} - \frac{1}{a_1^2}\right] \quad , \tag{2.7}$$

is about 20 G/cm at the location of the MMOT. Four laser beams are directed at the intersection point of the atomic beam incident from the PMOT with the vertical launch section of the guide. All beams are aligned at an angle of 45^o relative to the vertical guide axis. As Fig. 2.1 shows, the four MMOT beams consist of a pair with upward and a pair with downward directions. The planes spanned by these beam pairs are orthogonal to each other and contain the vertical axis. The beams with downward direction are operated at a slightly lower frequency than those with upward direction. All beams are red-detuned from the ^{87}Rb $5S_{1/2}$ $F = 2 \rightarrow$ ^{87}Rb $5P_{3/2}$ $F' = 3$ transition. The beams are circularly polarized in a suitable manner and have intensities of about 5 mW/cm^2. This configuration of magnetic fields and laser beams results in a two-dimensional MMOT that compresses the divergent atomic beam emitted by the PMOT into a small-diameter cylindrical region ($\sim$ 200 μm) around the guide axis (which is vertical in the launch section). The average velocity v_0 (= launch velocity) of the atoms leaving the MMOT is parallel to the guide axis and can be tuned by varying the frequency difference of the up-going and down-going MMOT beams. In the frame of reference of the moving atoms, the frequencies of the MMOT are Doppler-shifted such that all beams appear at the same frequency. Thus, $v_0 = \delta\lambda/\cos(\theta)$, where δ is half the frequency difference between the up-going and down-going beams, λ is the wavelength of the atomic transition (780.244 nm) and $\theta = 45^o$ is the angle between the MMOT beams and the vertical. Typically, the relative de-tuning is adjusted such that the MMOT launches the atoms at $v_0 = 2.2$ m/s, which is within the range of velocities where MMOTs have proven to operate well [18–22].

An absorption scheme similar to the PMOT characterization was implemented to determine the performance of the MMOT as a function of detuning and gradient. In this case, because of limited optical access the probe beam had to be aligned perpendicular to the atomic flow and the guide field naturally had to be on. While these boundary conditions prevented us from measuring the velocity distribution, the output flux of the MMOT could be determined using the method explained in the following.

A low-power ($\sim 0.15\ I_{\rm sat}$), circularly polarized probe laser beam was aligned to intersect the topmost portion of the MMOT, just before the extraction zone. The diameter of the probe was made appreciably larger than the diameter of the atom flow in the MMOT. The MMOT was run in a pulsed fashion in which the MMOT light was on for 88 ms. During this time, the probe laser was off and atoms were cooled into the moving reference frame of the MMOT until steady-state conditions were reached. After the MMOT light was switched off, the probe laser was turned on and the relative absorption dP/P observed immediately after the turn-on of the probe was recorded. This procedure was repeated for different probe-laser frequencies $\nu_{\rm L}$.

For simplicity, we first consider the case where Zeeman effects can be neglected. In this case, the absolute power dP absorbed from the probe laser is, in the limit of weak absorption, given by

$$\begin{aligned} dP &= -N\gamma h\nu \\ &= -N\frac{\Gamma}{2}\frac{I/I_{\rm sat}}{1+4\left(\frac{2\pi\delta}{\Gamma}\right)^2}h\nu. \end{aligned} \tag{2.8}$$

where N is the number of atoms in the probe beam. Noting that $I = P/A$, where A

is the area of the circular probe beam, rearranging Eq. 2.8 gives

$$\begin{aligned}\frac{dP}{P} &= -\frac{N}{A}\left(\frac{\Gamma h\nu}{2I_{\mathrm{sat}}}\right)\\ &= -n_{\mathrm{l}}\left(\frac{\Gamma h\nu}{I_{\mathrm{sat}}\pi r}\right)\end{aligned} \tag{2.9}$$

where $A = \pi r^2$, $n_{\mathrm{l}} = N/(2r)$ is the linear number density of atoms, and r is the probe-beam radius. Thus, the number of atoms emitted from the MMOT per second is given by

$$\begin{aligned}\Phi &= n_{\mathrm{l}}v_0\\ &= \left(-\frac{dP}{P}\right)\left(\frac{I_{\mathrm{sat}}\pi r}{\Gamma h\nu}\right)v_0.\end{aligned} \tag{2.10}$$

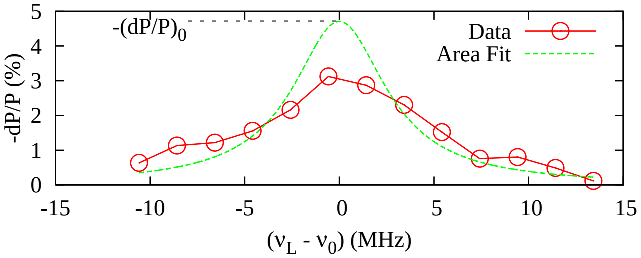

Figure 2.5: Absorption measurement of atomic beam exiting the MMOT. This figure shows the relative absorption $-dP/P$ of a probe beam passed through the atomic beam exiting the MMOT vs the frequency detuning of the probe laser $\nu_{\mathrm{L}} - \nu_0$. The red circles show measured data, while the green line shows a Lorentzian of 6 MHz FWHM that has the same area as the data curve.

Because the MMOT magnetic fields were actually on during the probe pulse, the peak absorption $(dP/P)_0$ is reduced due to line broadening caused by the Zeeman effect. To account for this effect, the following procedure was used. The relative absorption (dP/P) observed immediately after turn-on of the probe pulse was measured as a function of the laser frequency ν_{L} (circles in Fig. 2.5). While the Zeeman effect moderately broadens the absorption line, it does not significantly affect the integral of the absorption line because the Larmor frequency of the atoms ($\lesssim$ 500 kHz) is of order or less than the optical-pumping rate of the probe laser (∼2 MHz on-resonance).

Therefore, the absorption signal that would be measured if the magnetic field were off is given by a Lorentzian with 6 MHz FHWM linewidth and an area equal to that of the measured absorption line. This Lorentzian is shown by the dashed line in Fig. 2.5. The output flux of the MMOT is obtained by inserting the peak value of the Lorentzian ($-(dP/P)_0$ in Fig. 2.5) into Eq. 2.10. Typical obtained MMOT flux values are $\Phi_{\rm MMOT}(v_0 = 2.2~{\rm m/s}) = 5.4 \times 10^8~{\rm s}^{-1}$ and $\Phi_{\rm MMOT}(v_0 = 2.5~{\rm m/s}) = 4.8 \times 10^8~{\rm s}^{-1}$ for a MMOT field gradient of $\partial B/\partial \rho \approx 20$ G/cm. Because of the uncertainty of the area under data curves like that shown in Fig. 2.5, we estimate the uncertainty of these flux values to be about 30%. The results indicate that the transfer efficiency from the primary PMOT atomic beam into the cold, concentrated beam emitted by the MMOT is 16% to 18%. Further, the quoted flux values are a sum over all magnetic sublevels of the output atoms.

For MMOTs operated with gradients of $\partial B/\partial \rho = 15$ G/cm (225 A guide current) and $\partial B/\partial \rho = 10$ G/cm (150 A) we find MMOT flux values that are $\sim 90\%$ and $\sim 60\%$ of the above quoted ones, respectively. We further find that, while the average de-tuning $\delta_{\rm MMOT}$ of our MMOT laser beams from resonance typically is of order two line-widths, the MMOT output flux does not vary significantly over a range of $-2.5\Gamma \lesssim \delta_{\rm MMOT} \lesssim -1.5\Gamma$.

2.2.3 Dark-state extraction

Each atom emerging from the MMOT must traverse through the fringe fields of the four MMOT laser beams. This fact poses a problem, because accurate control of beam shapes and intensities in the fringe-field regions of the four MMOT beams is virtually impossible. Therefore, any extracted atom would experience strong, random differential radiation pressures in the fringe fields of the MMOT beams, causing the velocity to change in an erratic manner. The solution to this problem is dark-state extraction, *i. e.* optical pumping of the atoms into a "dark state" that does not scatter any MMOT photons. The optical pumping into the dark state needs to occur inside the MMOT volume, *before* the atoms reach the fringe fields of the MMOT laser beams. As explained in [23], the location of optical pumping into the dark state is defined through a layered arrangement of a MMOT re-pumper beam with a well-defined upper knife-edge and a de-pumper beam with a well-defined lower knife-edge. Any overlap between the re-pumper and the de-pumper beams needs to be avoided, while a small gap is allowable. The knife-edge planes are oriented orthogonal to the vertical guide axis. The MMOT re-pumper beam is resonant with the ^{87}Rb $5S_{1/2}$ $F = 1 \rightarrow 5P_{3/2}$ $F' = 2$ transition, while the de-pumper is resonant with the $5S_{1/2}$ $F = 2 \rightarrow 5P_{3/2}$ $F' = 2$ transition. This arrangement ensures that all atoms are transferred into the dark state $F = 1$ after traversal of the de-pumper knife-edge. Statistically, approximately one-third of the dark-state atoms will exit the MMOT in the magnetically guided sublevel $|F = 1, m_{\mathrm{F}} = -1\rangle$.

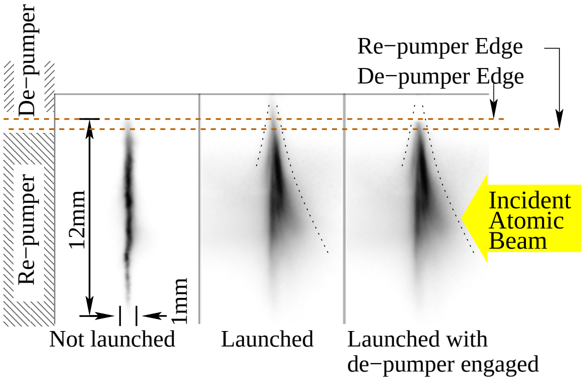

Figure 2.6: Fluorescence images of the MMOT (guide-axis vertical). The exposure times are chosen such that the images do not saturate. Left: Launch velocity $v_0 = 0$ m/s. The fluorescence rapidly diminishes above the re-pumper knife-edge. Middle: Launch velocity $v_0 = 1.6$ m/s and de-pumping beam blocked. Atoms are transported upward out of the range of the MMOT, leaving a thin trail of fluorescence along the guide axis above the re-pumper edge. Right: Launch velocity $v_0 = 1.6$ m/s and de-pumping beam active. The fluorescence abruptly diminishes above the de-pumper edge, as the de-pumper optically pumps all atoms into the dark state $F = 1$. The dotted lines in the middle and right images outline a narrowing of the MMOT as a function of height.

Fluorescence images of the MMOT in launch-mode show a characteristic narrowing shape, indicated by the dotted lines in Fig. 2.6. As the atoms travel upward along the extraction trajectory, their transverse excursions away from the guide axis diminish. The narrowing reflects the progression of laser cooling into the moving reference frame of the MMOT as a function of height in the guide. Thus, optimal operation of the MMOT shows a chevron-like pattern where the tip is completely narrowed, indicating optimal cooling in the transverse directions at the extraction point.

Also characteristic in these images is that fluorescence is absent (left image) or diminished (middle image) above the re-pumper cutoff. This reflects off-resonant optical pumping of the atoms into the dark extraction state $F = 1$ once they have left the range of the re-pumper beam. We have found that a small fraction of the atoms can be extracted from the MMOT in the dark state $F = 1$ just by ensuring that the upper edge of the re-pumping region is located well within the MMOT region, as in the middle image. The flux of atoms extracted in the dark state is drastically improved by employing the de-pumper beam, as in the right image of Fig. 2.6. The sharp fluorescence cutoff at the lower edge of the de-pumper beam, seen in the right image, shows that all atoms still reaching the de-pumper region in the bright $F = 2$ state are transferred into the $F = 1$ dark extraction state by rapid on-resonant optical pumping. We have found experimentally that the presence of the de-pumping beam increases the yield of guided atoms by at least a factor of five over the yield obtained in the absence of the de-pumper (this contrast is relevant in Fig. 4.3 below).

2.3 Gravitational slowing and magnetic compression

The vertical launch section of the guide has a height of 0.2 m from the de-pumper knife-edge to the top end of the 90° bend. In the launch section, the atoms are slowed down by gravity as they travel upward. Using the MMOT laser frequencies as a velocity tuning parameter, the MMOT extraction velocity v_0 is adjusted such that the atomic flow has a reasonably low velocity at the top of the launch section while maintaining a high atomic flux. We have found a useful extraction velocity range of 2.2 m/s $\leq v_0 \leq$ 2.8 m/s, corresponding to a velocity range 1 m/s $\leq v \leq$ 2 m/s near the top end of the 90° bend.

The atom guide is tapered [24, 25], *i.e.* the center-to-center distance between the inner pair of guide tubes decreases from about 3.7 cm at the location where cold atoms are transferred from the MMOT into the guide down to 5.17 mm in the 90° bend. Taking the fields of both the inner and outer tube pairs into account, from Eq. 2.7 it follows that the field gradient increases from about 20 G/cm at the MMOT to 1.7 kG/cm in the 90° bend. A crucial benefit of the gradient increase is that the atomic distribution becomes magnetically compressed in the transverse directions as the atoms propagate through the tapered region. The compression enhances the collision rate and will thus, in future, facilitate evaporative cooling.

Under absence of collisions, the action of the transverse motion of the magnetically guided atoms, $S_\perp = \oint \mathbf{p}_\perp \cdot \mathbf{dq}_\perp$, is adiabatically conserved [24, 25]. The adiabatic invariance entails a partial conversion of forward kinetic energy into transverse energy in the magnetic-compression region. Consequently, atoms in the vertical launch section of the guide are decelerated due to gravity and an additional retarding force that grows with increasing transverse energy. Simulations show that due to this effect about half the atoms in the magnetically guided state $|F = 1, m_{\mathrm{F}} = -1\rangle$ are reflected backward. The reflected atoms are partially re-cycled, because they fall back into the MMOT. It is also noted that an increased collision rate will break the adiabatic conservation of the transverse action, and therefore reduce the fraction of reflected atoms.

Once in the narrow region of the vertical guide section (5.17 mm center-to-center wire separation), additional velocity filtering occurs due to gravity and the 90° bend. While the fastest atoms overshoot the bend, the slowest atoms fall back into the MMOT. From simulations, we expect this filtering to further reduce the flux by about 15%.

The total coupling efficiency from the MMOT into the horizontal guide section is given by the fraction of atoms that exit the MMOT in the magnetic sublevel $m_{\mathrm{F}} = -1$ (33%) times the probability that an atom does not become reflected in the vertical guide section (40 to 50%). Thus, an initial estimate of the flux into the horizontal guide section is $\Phi_{\mathrm{Hor}} = 0.15 \times \Phi_{\mathrm{MMOT}} = 8 \times 10^7$ s^{-1}.

In this chapter, I have describe the experimental setup for the magnetic guide. To summarize, a cold atomic beam is generated by the Pyramidal MOT. This beam is captured by a 2D+ MOT operating in a continuous manner. The 2D+ MOT launches the atomic beam into the magnetic guide. However, due to the extreme change in the restoring force on the atoms as they leave the optical cooling zone, there is a significant mode mismatch between the atomic optical injection and the magnetic guide. This causes atoms to be sprayed upwards, very much like spraying water upwards from a hose into an inverted funnel. Only the atoms which have trajectories close to the guide axis are injected into the guide, and are detected at the end of the guide, as described in Chapters III and IV.

CHAPTER III

Imaging Atoms in High-gradient Magnetic Field

As we have seen in Chapter II, the atomic beam is injected into a very high gradient magnetic guide. The biggest challenge in characterizing this guided atomic beam lies in the fact that it is very difficult to obtain images of the beam which can be easily and unambiguously analyzed. One method is to turn of the guiding field and use resonant fluorescence imaging. However, the process of switching fields involves switching large currents. This leads to rapid thermal cycling effects that may cause micro-leaks to appear at the vacuum feedthroughs [11] and also to transients in the current loop due to high inductance. We also want to measure the steady-state distribution of cold atoms in the guide. But switching the fields off in order to acquire an image will necessitate a long waiting time for the system to attain steady state again for the next image to be taken. Consequently, an unacceptably low measurement repetition rate will result. Therefore, a robust imaging method is needed that delivers true representations of cold-atom distributions with the trapping fields left on.

At least two methods exist from which a signal that is directly proportional to the density of the sample can be delivered. The first, phase-contrast imaging (a non-destructive scheme), allows one to measure the change of the index of refraction for far-off-resonant light propagating through an atomic sample that is optically dense at resonant frequencies. The disadvantage of this method lies in the requirement to have atomic samples of very high density, which in many cases are not available. A second method relies on the optical pumping of atoms using an open transition. This open-channel imaging method is occasionally used to measure the total atom number in optically thick samples [26, 27]. As discussed in this paper, in certain cases it also is the best method to characterize non-optically thick samples [11, 28].

We characterize the performance of the open-channel cold-atom imaging method in cases where Zeeman shifts change significantly through the detection region. The method yields accurate atomic density distributions and should be applicable to other trapping situations as well as to the trapping of molecules (which do not offer closed optical transitions).

3.1 Closed-channel imaging

3.1.1 Continuous atomic-beam probing

To most readily observe the atomic beam, continuous re-pump and probe lasers are co-aligned such that they illuminate a small portion of the atomic flow. The re-pump laser, tuned to the $F = 1 \rightarrow F' = 2$ transition, optically pumps the guided atoms in the $|F = 1, m_{\mathrm{F}} = -1\rangle$ state into an $F = 2$ state. The re-pumped atoms generate abundant fluorescence from the probe laser, which is tuned on-resonance with the closed-channel $F = 2 \leftrightarrow F' = 3$ cycling transition. The fluorescence imaged onto a CCD camera enables continuous, spatially resolved, real-time atomic-beam observation (see Fig. 3.1, left image).

Continuous imaging of the atomic distribution has certain drawbacks. The radiative force from the probe laser accelerates atoms quickly out of resonance and causes a diminishing signal in the atomic beam direction. Further, due to re-pumping of the atoms into the $F = 2$ bright state and the subsequent closed-channel fluorescence on the $F = 2 \leftrightarrow F' = 3$ transition, a mixture of low- and high-magnetic-field seeking sub-levels is populated. The magnetic-dipole force in the guide is different for these various magnetic sub-levels. In addition, the atoms are exposed to the diffusive component of the radiative force due to the probe laser. Hence, the atomic flow is significantly diffused in a complicated manner during the imaging. Therefore, the observed image profile transverse to the atom flow is wider than the actual atomic distribution in the guide. The widening of the beam profile increases in the direction of the atomic flow. These effects lead to images a of broadened and distorted atomic-beam, as shown in the left panel of Fig. 3.1.

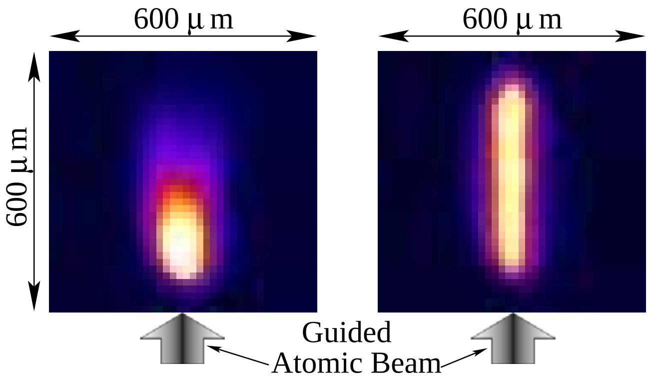

Figure 3.1: Contrasting images of flashed and non-flashed probe. (Left) Fluorescence image of a distorted atomic beam obtained with a continuous probe. (Right) Non-distorted atomic beam imaged via strobed probe pulses of 20 μs duration and 1 ms separation.

3.1.2 Elimination of image distortion using a strobe technique

In order to obtain undistorted images of the atomic distribution, the re-pump and probe beams in the imaging region are pulsed. The duration of each strobe pulse is short enough such that particle motion during the strobe-pulse duration can be neglected. The waiting time between subsequent strobe pulses is chosen sufficiently long that each strobe pulse interacts with an entirely undisturbed section of guided atomic beam.

For ^{87}Rb, the scattering rate at saturation intensity (about 10^6 s^{-1}) corresponds to an average acceleration of 6×10^4 m/s^2 for atoms resonant with the probe light. Assuming that an atom starts from rest, its displacement during the 20 μs long detection pulse is ≤ 12 μm. Because this displacement is much smaller than the atomic-beam diameter (about 200 μm), atomic-motion-induced blurring can be neglected for strobed atomic-beam images. To obtain a high signal-to-noise ratio in the strobed fluorescence images, typically 1000 strobed images are accumulated (which takes only of order 1 second). The strength of the strobing technique becomes apparent by comparing the left (continuous) and right (strobed) panels of Fig. 3.1. The strobed image is not blurred in the direction transverse to the atomic flow and extends in an unabated manner over the whole length of the illuminated atomic-flow segment.

3.1.3 Influence of Zeeman effects

In a high-gradient magnetic guide such as ours, atoms are tuned out of resonance from the probe laser frequency at distances of only a few tens microns away from the guide axis. Due to the spatial variation of Zeeman shifts, the number of closed-channel probe photons scattered per atom varies in a complicated manner throughout the detection region. The spatial variation in the number of probe photons scattered per atom becomes even more significant because of the position-dependence of the probe-beam intensity, the position-dependence of the angle between laser polarization and magnetic field, and optical pumping among magnetic sublevels. Consequently, fluorescence images produced by a strobed, monochromatic, closed-channel probe laser differ strongly from the density profile of cold atoms in the magnetic guide. Thus, it is highly impractical to extract the atomic density profile from the measured closed-channel fluorescence images.

3.2 Open-channel imaging

3.2.1 Outline of the method

The difficulties described in Sec. 3.1 are circumvented by using an imaging method that produces a constant photon yield per atom, independent of atom location and detailed laser parameters. The method relies on the use of an open-channel transition to probe the atoms. In the present case, in which ^{87}Rb atoms are traveling in the $|F = 1, m_{\mathrm{F}} = -1\rangle$ state, the open-channel transition is the $F = 1 \rightarrow F' = 2$ re-pump transition. An atom in $F = 1$ scatters a re-pump photon and decays into one of the two hyper-fine ground levels $F = 1$ and $F = 2$. If the atom decays into the $F = 1$ level, the scattering process is repeated. If the atoms decays into the $F = 2$ level, it ceases to scatter more probe photons because the $F = 2 \rightarrow F' = 2$ transition is 6.83 GHz red-detuned from the re-pump transition. In Sec. 3.2.2, we find that, on average, an atom scatters 2.5 photons before being transferred into the non-resonant $F = 2$ state, independent of laser intensity and Zeeman shift. To ensure a uniform photon yield throughout the atomic sample, we only require the excitation rate on the open-channel re-pump transition $F = 1 \rightarrow F' = 2$ to be $\gtrsim 2.5$ times the inverse imaging-pulse width (10^5 s^{-1} under the conditions of Fig. 3.1). Assuming an intensity of $10 I_{\mathrm{sat}}$, where $I_{\mathrm{sat}} = 1.6\ \mathrm{mW/cm}^2$ is the saturation intensity, this condition is satisfied well for magnetic fields up to at least ~ 60 G. If the atomic distribution samples magnetic fields less than this value, as in Fig. 3.1, almost all atoms will have sufficient time to become optically pumped into the non-resonant $F = 2$ state during their interaction with the open-channel imaging pulse. Consequently, the photon yield per atom will be uniform throughout the atomic sample, and the fluorescence images will be proportional to the atomic distribution projected onto the image plane. The only disadvantage of this method is that the average yield of 2.5 photons per atom is quite low. Hence, a sensitive camera is required to detect the open-channel images.

3.2.2 Simulation

We have simulated the open-channel detection process of cold ^{87}Rb atoms in the $|F = 1, m_{\rm F} = -1\rangle$ state in the magnetic field generated by two parallel current-carrying wires (as in Fig. 1.3). Using the quantum Monte-Carlo wave function (QMCWF) technique [29], we simulate the time evolution of the atoms in a laser field tuned close to the $F = 1 \rightarrow F = 2$ open-channel probe transition. In the simulation, we include the ground state hyperfine levels $F = 1$ and $F = 2$ and the excited-state levels $F' = 0, 1$, and 2. The exact magnetic field of appropriately placed infinitesimally thin wires is used, resulting in a transverse gradient of 2.7 kG/cm at the minimum of the guiding potential, as shown in Fig. 1.3. Zeeman shifts are assumed to be linear throughout the detection region. For the ground-state manifold ($F = 1$, g-factor $g_{\rm F} = -1/2$), this approximation is very well satisfied due to the large hyperfine splitting (6.83 GHz) between $F = 1$ and $F = 2$. The coupled excited-state manifolds ($F' = 0$, 1, and 2 with $g_{\rm F'} = 2/3$) have separations of 72 MHz (between 0 and 1) and 157 MHz (between 1 and 2). Zeeman shifts of these F' levels are approximately linear for magnetic fields less than about 60 G, corresponding to radial displacements from the guide axis of $\rho \lesssim 220$ μm. As seen in Fig. 1.3, the atomic distribution is mostly contained within this radius. Within the region of interest, the approximation of linear Zeeman shifts is therefore valid not only for the $F = 1$ ground state, but also for the relevant excited states. As in the experiment, the polarization of the simulated open-channel imaging beam is linear, transverse to the guide wires, and in the plane spanned by the guide wires. The temperature of the guided atomic beam is low enough that Doppler shifts ($\lesssim 1$ MHz) are entirely negligible.

In the simulation, we average 500 quantum trajectories at each point on a uniform grid in a plane transverse to the magnetic-guide wires within the detection region. Each quantum trajectory is propagated until the atom is transferred from the $F = 1$ into the $F = 2$ sub-level, or until the simulation time reaches the end of the 20 μs imaging pulse. During the imaging pulse, the atoms are assumed to be stationary. The observables of primary interest are the average photon yield per atom and the probability that an atom is transferred into the $F = 2$ state, each as a function of position.

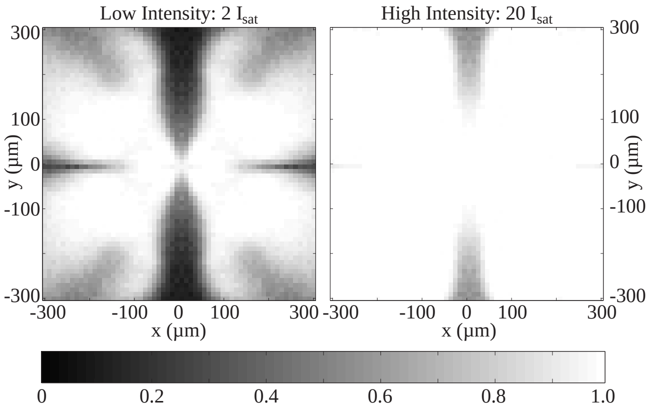

Figure 3.2: Probability of an atom being transferred into the $F = 2$ state during the 20 μs open-channel imaging pulse vs position (x, y), for probe intensities $2I_{\mathrm{sat}}$ (left) and $20I_{\mathrm{sat}}$ (right). The detection laser field is detuned by -15 MHz from the $F = 1 \rightarrow F = 2$ probe transition and is linearly polarized in x-direction. In the high-intensity case, it is apparent that nearly 100% transfer is achieved throughout the displayed spatial range.

The results show that, for a sufficiently intense probe, atoms become transferred into the $F = 2$ state with near 100% probability, as can be seen in the right panel of Fig. 3.2. In a crude approximation, one may assume that in the simulated open-channel detection process the atoms are predominantly excited into the $F' = 2$ level. By summing over the transition probabilities, one can see that the decay probabilities from $F' = 2$ state into the ground hyperfine levels $F = 1$ and $F = 2$ are 50% each. Thus, neglecting off-resonant excitation into the $F' = 1$ and $F' = 0$ levels, the probability $P(n)$ that an atom scatters n photons while being transferred into the

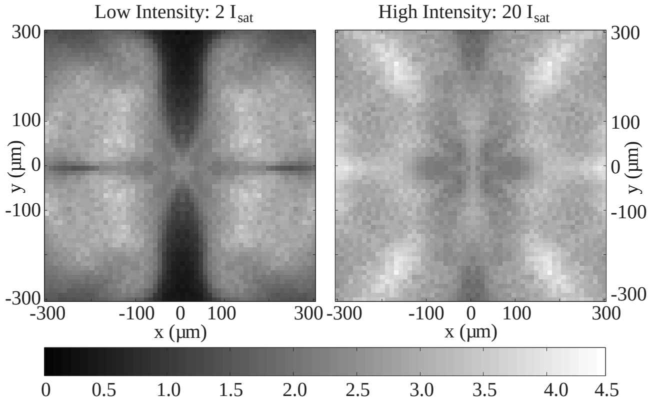

Figure 3.3: Simulated average number of photons vs position (x, y), scattered by magnetically trapped Rb atoms illuminated by an open-channel imaging pulse of 20 μs duration and a constant intensity of $2I_{\text{sat}}$ (left) and $20I_{\text{sat}}$ (right). The imaging geometry used in the experiment corresponds to an observer located on the negative y-axis. !!!The experimental signal corresponds an integral of the product of the atomic density distribution and in the y-direction.!!!

$F = 2$ ground state is $P(n) = 2^{-n}$. The average photon number then is expected to be $\langle n \rangle = \sum_{n=1}^{\infty} nP(n) = 2$.

However, the results from the simulation show that, for magnetic field magnitude $\gtrsim$ 30 G, the average number of photons required to optically pump atoms into the $F = 2$ ground state is larger than 2. This can be explained as follows. For higher magnetic field values, the magnetic sub-components of the $F = 1 \rightarrow F' = 2$ transition tune out of resonance due to Zeeman shifts, and photon scattering due to the $F = 1 \rightarrow F' = 1$ transition becomes more significant. The probability that an atom excited into the $F' = 1$ level decays back into the $F = 1$ ground state is 5 times greater than that of decaying into the $F = 2$ ground state. Thus, for higher magnetic fields, as the $F = 1 \rightarrow F' = 1$ transition becomes more important, an atom scatters more photons before becoming optically pumped into the $F = 2$ ground state. The simulation results shown in Fig. 3.3 indicate that for an atomic beam of ~ 200 μm diameter and $I = 20I_{\text{sat}}$, each atom scatters on average 2.5 photons, with a variation of less than ± 0.5 photons. Under these conditions, almost all atoms are optically pumped into the $F = 2$ ground state, as shown in the right panel of Fig. 3.2.

It is apparent in Figs. 3.2 and 3.3 that low illumination intensity results in a strong position dependence of the transfer efficiency and photon yield, respectively. The radial dependence is largely due to the increase of the Zeeman shift as a function of radial position in the magnetic guide. The structures present in the angular degree of freedom reflect the fact that the angle between laser polarization and the magnetic field varies throughout the detection region. This leads to variations in the relative importance of π, σ^+ and σ^- transitions and in optical pumping among the magnetic sublevels of $F = 1$.

Overall, the QMCWF simulations verify that for a sufficiently high probe intensity the open-channel imaging technique yields a nearly uniform number of photons per atom throughout the probe region. For trap-field-induced shifts of the open-channel probe transition $\lesssim 100$ MHz and a imaging-pulse duration of 20 μs, the simulations show that an imaging-pulse intensity of 10 I_{sat} is sufficient.

3.2.3 Imaging setup

The utilized imaging setup is shown in Fig. 3.4. A laser locked 15 MHz below the $F = 1 \rightarrow F' = 2$ transition provides both re-pumping light for laser-cooling as well as the open-channel probe light for imaging of the magnetically guided atoms. An acousto-optic modulator (AOM) in a double-pass configuration allows for fast switching of the imaging pulse. The probe beam is aligned through the AOM such that its frequency is not shifted during its on-phase, while a complete extinction is achieved during its off-phase (see bow-tie beam path through AOM in Fig. 3.4). The time interval between adjacent imaging pulses is chosen sufficiently long that each imaging pulse interacts with a completely undisturbed sample of the atomic beam. For the results presented here, 20 μs detection pulses are followed by waiting intervals ranging from 1 ms at low imaging-beam intensity to 4 ms at high intensity.

The output of the AOM is passed through a single mode fiber and collimated to obtain a clean spatial Gaussian mode of about 5 mm diameter. This beam is then used to illuminate an aperture ≈1 mm in diameter. This filtering technique creates an approximate top-hat intensity profile immediately after the aperture. By imaging the plane of the aperture directly into the atomic beam, as indicated in Fig. 3.4, the intensity profile of the probe beam in the detection region also represents a top-hat profile, with minimal diffraction effects. Two benefits of this illumination method are that the intensity throughout the detection region is uniform and that scattering of probe light on the guide wires is minimized.

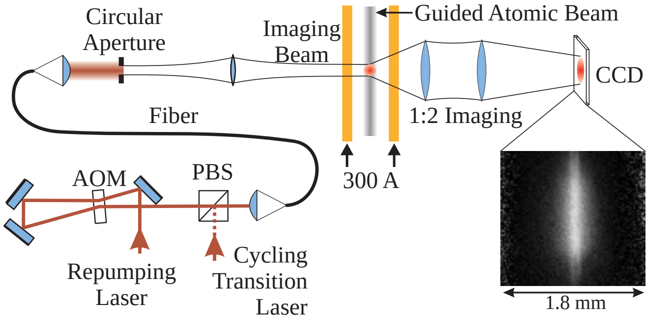

Figure 3.4: Imaging setup. The imaging light first passes through an acousto-optic modulator (AOM) which provides fast switching for the imaging pulse. The pulsed imaging light is then passed through a fiber, collimated, and directed onto an aperture of ≈ 1 mm diameter. By imaging the aperture into the probe region of the magnetic guide, an approximate top-hat intensity profile of the imaging beam is achieved. Each probe pulse optically pumps the atoms from $F = 1$ into $F = 2$, thereby generating ≈ 2.5 photons per atom. This open-channel fluorescence is observed using a lens system that images the guided atomic beam onto a sensitive CCD camera with a 1:2 magnification ratio.

Because one probe pulse yields only ≈ 2.5 photons per atom emitted over a solid angle of 4π steradians, and because there are only about 9000 atoms in the probe volume, an efficient imaging of the atomic fluorescence is critical. The imaging system consists of two 2-inch diameter achromatic lenses with an object-side numerical aperture of 0.3 and magnification factor of 2. We further use a back-illuminated CCD (quantum efficiency ≈75% at 780 nm) from Andor Technology to detect the atomic fluorescence (Part number iXon DV-887 ECS BV). This CCD has an on-chip charge-amplifying gain element that enables near-single-photon detection capability.

3.2.4 Open-channel imaging results

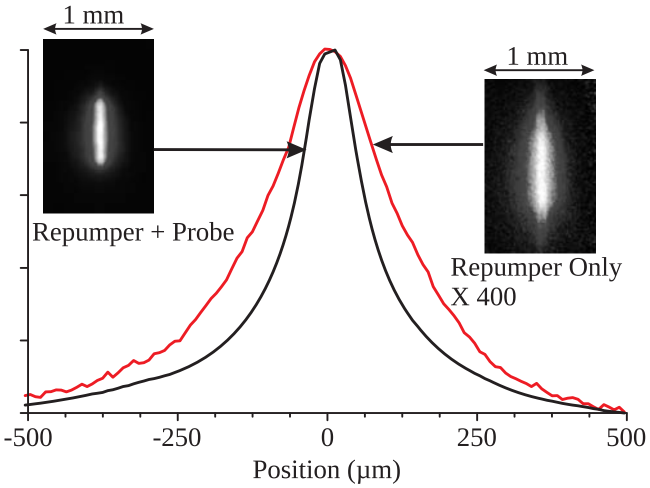

Figure 3.5: Contrasting open-channel and closed-channel imaging. (Top Curve) Fluorescence profile of a magnetically guided beam of cold atoms obtained by open-channel ($F = 1 \rightarrow F' = 2$) fluorescence imaging. (Bottom curve) Corresponding fluorescence profile obtained by measuring fluorescence from the closed-channel $F = 2 \leftrightarrow F' = 3$ cycling transition.

In Fig. 3.5 we show a comparison between atomic-beam fluorescence profiles measured using either a closed-channel image or an open-channel image. The profiles are obtained by integrating images such as the ones shown in Fig. 3.1 along the atomic-beam direction, defined to be the z-axis (vertical axis in Fig. 3.1). In order to eliminate the influence of diffraction effects and of the circular shape of the illumination region on the beam profiles, the integration range is limited to a region in which the measured fluorescence does not significantly depend on z. While the closed-channel measurement in Fig. 3.5 has a high signal strength and a high signal-to-noise ratio, it does not reflect the true atomic distribution, as explained in Sec. 3.1.3. The open-channel profile in Fig. 3.5 reveals that the atomic-beam density profile is significantly wider than suggested by the closed-channel profile. Thus, Fig. 3.5 reiterates the advantages of using images obtained with an open-channel probe over those obtained with a closed-channel probe for determining atomic distributions. In the following, we demonstrate experimentally that for sufficiently high probe intensity, open-channel imaging provides fluorescence images that are approximately proportional to the underlying atomic-beam density profiles.

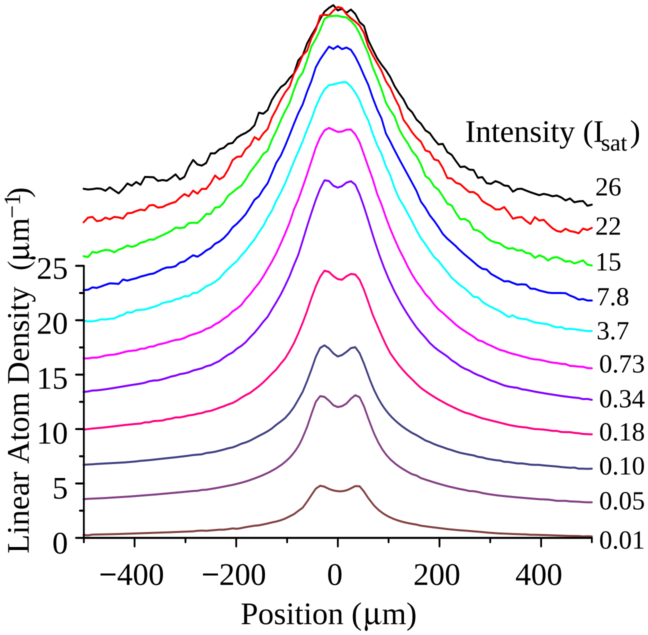

Figure 3.6: Linear atomic density for various repumper intensities. The linear density plots of detected atoms derived from fluorescence images obtained with the indicated intensities of the open-channel imaging laser are shown. With increasing intensity, the profile converges towards the atomic density distribution. At high intensity, the noise level increases due to an increasing amount of stray light (which scales linear in intensity).

To obtain uniform photon yield in the magnetic guide, one must ensure that *all* atoms in the detection region are transferred into the $F = 2$ state during the probe pulses. This condition necessitates a sufficiently intense open-channel imaging pulse such that $\gamma\tau \gtrsim 2.5$ throughout the atomic sample, where γ is the photon scattering rate on the open-channel transition and τ is the duration of the detection pulse. In Fig. 3.6, we show the apparent linear atom density derived from open-channel fluorescence profiles for different imaging-laser intensities. In the conversion of fluorescence profiles into linear atom densities it is assumed that each atom isotropically scatters 2.5 photons on average. This means that, at low intensity, the atoms are actually under-counted because the average photon yield per atom is less than 2.5. The data shown in Fig. 3.6 demonstrates that with increasing probe intensity the open-channel image actually converges to an intensity-independent result, which approximately reflects the actual atomic distribution. In the measurement shown in Fig. 3.6, the open-channel imaging laser was slightly detuned from the atomic resonance for technical reasons. This detuning causes the open-channel imaging laser light to be resonant with an $F = 2 \rightarrow F' = 2$ transition at a distance of approximately 30 μm from the center of the trap. At low intensity, a combination of intrinsic scattering behavior and detuning results in a double-peak structure, as can be seen in Fig. 3.6 for $I \lesssim 1I_{\mathrm{sat}}$. As the imaging-beam intensity and thus the scattering rate γ increase, the double-peak structure disappears, while the linear density of counted atoms converges towards a limiting distribution which is identified with the atomic density distribution. In Fig 3.6, the atomic-beam profile is seen for intensities $I \gtrsim 5I_{\mathrm{sat}}$.

The integrals of the profiles in Fig. 3.6 equal the total number of atoms counted in the detection volume. As shown in Fig. 3.7, the fraction of atoms detected increases as the intensity of the probe pulse is increased. The detected fraction saturates around $5I_{\mathrm{sat}}$, indicating that under this condition all atoms become optically pumped from the $F = 1$ to the $F = 2$ ground state and deliver, on average, 2.5 photons each. On the plateau, the open-channel imaging is fully effective throughout the probe volume. Based on this conclusion and using appropriate calibration procedures, we find that the plateau in Fig. 3.7 corresponds to 9000 atoms present in the detection volume.

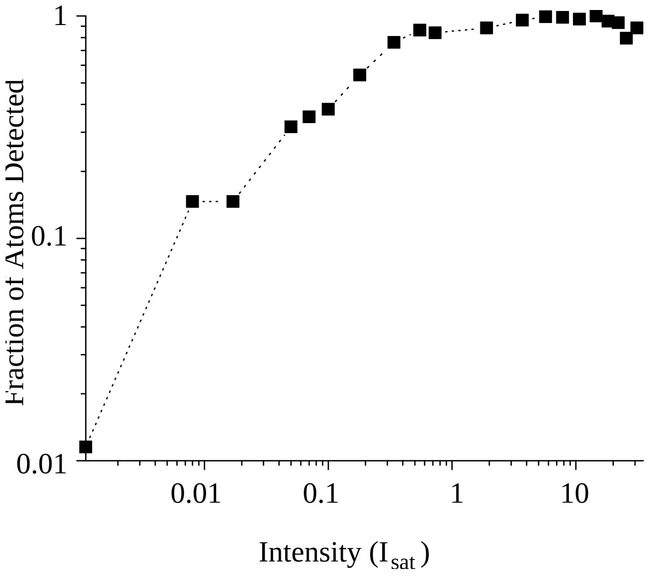

Figure 3.7: Fraction of detected atoms as a function of the intensity of the open-channel imaging pulse. The data are obtained by integrating the curves in Fig. 3.6 and by normalizing with the result obtained in the high-intensity limit (which corresponds to 9000 atoms).

3.3 Conclusion

In this chapter, we have characterized an open-channel detection technique for measuring atomic distributions in high-gradient magnetic traps. This technique does not require the trapping field to be switched off and therefore is most useful for static-field traps. This technique is easy to implement in any existing imaging setup and can be generalized to traps that involve both electric and magnetic fields, as well as AC electric-dipole traps (far-off-resonant laser traps).

CHAPTER IV

Characterization of Magnetically Guided Atomic Beam

We have so far seen how the atoms are injected into the atomic guide, and how the atomic beam in the high-gradient region is imaged so as to make the analysis as clear as possible. Some of the important parameters characterizing the atomic beam in the guide are the temperature of the atomic flow and the flux of the atoms through the guide. We use the term “temperature” in order to quantify the velocity spread of the atoms, even though the collision rate is too small to establish a local thermal equilibrium in the atom flow. This deliberate use of the term temperature is common in laser-cooling applications.

As we have seen in Chapter III, the most direct method to measure the transverse temperature is to only use re-pumper light in the probe region, with an intensity exceeding about one saturation intensity of the cycling transition ($I_{\mathrm{sat}} = 1.6$ mW/cm^2). The duration of the strobe intervals (20 μs) is sufficiently long that all atoms inside the detection volume scatter of order two re-pumper photons and become optically pumped into the $F = 2$ state. Notably, this even applies to the atoms traveling in the wings of the atomic flow, which experience the largest Zeeman shifts. Each atom in the probe volume therefore produces the same amount of fluorescence signal during detection, independent of the magnetic field at which the atom is located.

Due to this uniformity of the signal obtained per atom, images obtained with only re-pumper light are proportional to the atomic-flow density projected onto the image plane. This property makes re-pumper-only images particularly easy to analyze.

4.1 Atomic-beam analysis at the knee bend

4.1.1 Measurement of the transverse temperature

A typical re-pumping-only fluorescence image and its profile are displayed in Fig. 4.1.

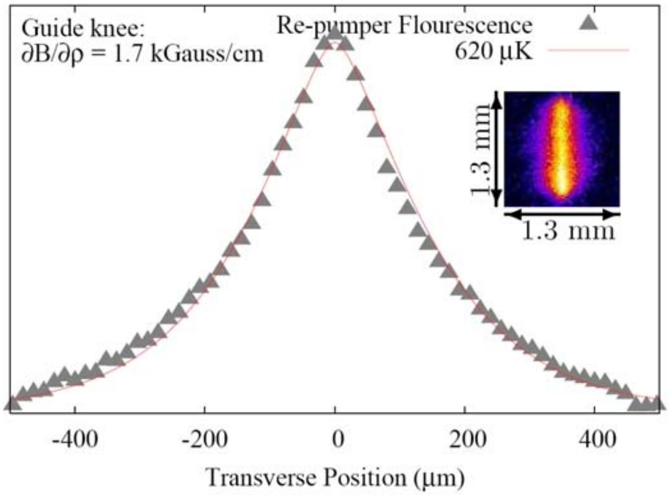

Figure 4.1: Atomic-beam image and corresponding profile transverse to the guide axis. The image (inset) is obtained at a location just below the atom-guide knee with re-pumping light only. In the image, the guide axis is vertical. The line through the data points represents a fit for a temperature of 620 μK.

Assuming a thermal distribution in the degrees of freedom x and y transverse to the guide axis, the profile data can be fitted with a function

$$P(x) \propto \int_{-\infty}^{\infty} \exp\left[-\frac{V(x,y)}{k_{\mathrm{B}}T_{\perp}}\right] dy \tag{4.1}$$

where the magnetic-dipole potential $V(x,y) = \frac{1}{2}\mu_{\mathrm{B}}B(x,y)$, and μ_{B} is the Bohr magneton. $B(x,y)$ is the exact magnetic field for a pair infinitesimally thin wires separated by the center-to-center distance of the guide wires. A small longitudinal component ($\gtrsim$ 200 mG) generated by a combination of the Earth's magnetic field and other environmental fields is also present. The transverse temperature $T_\perp$ is the fit parameter of interest. The data in Fig. 4.1 are fit best with $T_\perp = 620\ \mu\text{K} \pm 15\ \mu\text{K}$.

If the atoms are illuminated with both re-pumper and probe light, the fluorescence on the cycling transition entirely dominates the photon yield per atom. Using a probe intensity of order ten saturation intensities, atoms located at a magnetic field at which the applied probe light is resonant with the cycling transition scatter of order 300 photons during a strobe pulse of 20 μs duration. By de-tuning the frequency of the probe light, the Zeeman shift 1.4 MHz/G of the cycling transition $|F = 2, m_\text{F} = 2\rangle \rightarrow |F' = 3, m'_\text{F} = 3\rangle$ manifests itself as shown in Fig. 4.2: for zero de-tuning of the probe laser from the field-free transition frequency, mostly atoms traveling very close to the guide axis, where the magnetic field is low, are observed. For significant de-tunings, the images mostly show atoms traveling at a distance from the guide axis where the magnetic field is such that the cycling transition is resonant. The signal from these outlying atoms depends strongly on the polarization of the probe light. To balance optical pumping effects on both sides of the guide axis in the image plane, a linear probe light polarization was used. Taking multiple atomic-beam profiles at different de-tunings (and equal intensities), the *envelope* of the entire set of curves gives a representation of the transverse extension of the atomic beam. Assuming a thermal distribution in the transverse degrees of freedom, the transverse temperature $T_\perp$ can be determined by fitting the envelope to the function

$$P_\text{E}(x) \propto \int_{-\infty}^{\infty} w(x,y) \exp\left[-\frac{V(x,y)}{k_\text{B} T_\perp}\right] dy \tag{4.2}$$

where $w(x, y)$ is the position-dependent number of photons scattered per atom. For a linear probe-laser polarization transverse to the guide axis, the probed atoms tend to be optically pumped into the magnetic sublevels $|F = 2, m_\text{F} = \pm 2\rangle$ (quantization axis parallel to the laser direction). Thus, approximately half of the probe-light intensity I drives the atoms on the cycling transition, and $w(x, y)$ is given by

$$w(x, y) = \frac{\Gamma}{2} \frac{s}{(s+1)} \tau \tag{4.3}$$

where Γ is the excited-state decay rate ($2\pi \times 6$ MHz), τ is the strobe interval, s is given by

$$s = \frac{I}{2I_{\mathrm{sat}}} \frac{1}{1 + 4\left(\delta(x, y)/\Gamma\right)^2}, \tag{4.4}$$

and

$$\delta(x, y) = \frac{\mu_{\mathrm{B}}}{h} (B(x, y) - B(x, 0)) \tag{4.5}$$

is the detuning of the probe laser from the Zeeman-shifted atomic resonance at location $(x, 0)$. Note that the fitting function in Eq. 4.2 does not represent a profile for a single laser frequency. Rather, Eq. 4.2 represents the envelope of the peaks from a set of profiles obtained with different laser frequencies. Using fit functions of the type in Eq. 4.2, the envelope of the data in Fig. 4.2 is found to correspond to a transverse temperature $T_{\perp} \approx 420$ μK.

In all measurements where the frequency of the probe laser was varied and the temperature $T_{\perp}$ was obtained by fitting the envelope of the peaks in the fluorescence profiles (such as in Fig. 4.2), the fit results for $T_{\perp}$ were notably lower than those found using the repumper-only scheme. This discrepancy is explained as follows. Since the repumper frequency was not detuned with the probe, the repumping rates in the wings of the atomic beam were notably lower than those near the core of the atomic distribution. Thus, atoms in the wings require a significant fraction of the probe-pulse duration to become re-pumped, and produce less net fluorescence on the cycling transition than atoms traveling near the guide center. This effect leads to systematically reduced values for $T_{\perp}$ in the temperature fits. Therefore, temperatures

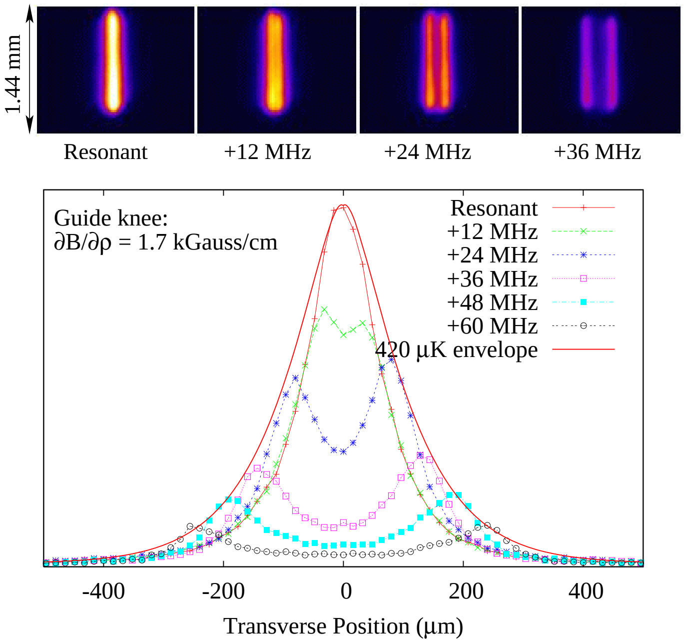

Figure 4.2: Atomic beam images obtained by detuning the probe beam. Top row: Atomic-beam images with both re-pumper light and probe light present in the detection region for the indicated de-tunings of the probe laser relative to the field-free transition frequency. The images are obtained at a location just below the atom-guide knee and with a horizontal linear polarization of the probe laser. In the images, the guide axis is vertical. Lower panel: Profiles of atomic-beam images transverse to the guide axis for the indicated de-tunings of the probe laser relative to the field-free transition frequency. By fitting the *envelope* of the profiles with curves of the type Eq. 4.2, a transverse temperature of $T_\perp \approx 420\ \mu$K is obtained.

obtained using the repumper-only scheme (as in Fig. 4.1) are considered more reliable than those obtained with the probe-repumper scheme (as in Fig. 4.2).

4.1.2 Measurement of the longitudinal temperature

To determine the longitudinal temperature of the guided atomic beam, we have performed a time-of-flight analysis. This was done by observing the turn-on behavior of the atomic-beam density after a sudden enhancement of the atom flow out of the MMOT. The atomic flow is suddenly enhanced by about a factor of five by turning on the de-pumping beam located in the MMOT exit region. The data were obtained by varying the time over which the atomic-beam fluorescence is integrated. Data sets for two different launch velocities, displayed in Fig. 4.3, show that the signal varies linearly with integration time until the enhanced atomic flow reaches the probe region, at which point the slope changes due to the increase in atomic flux. The time-of-flight distribution is obtained by differentiating the curves shown in Fig. 4.3 twice.

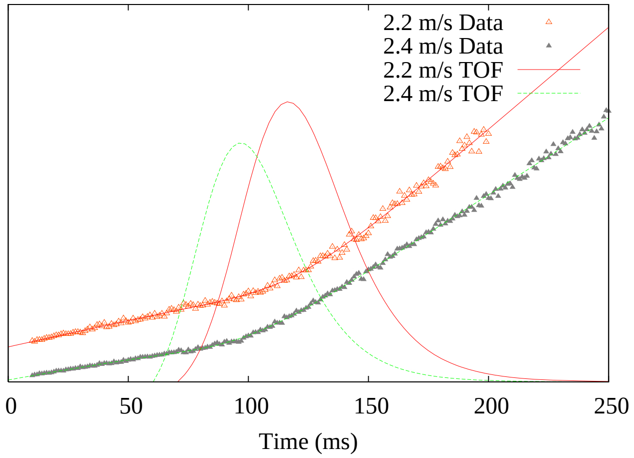

Figure 4.3: Time-of-flight experiment in the vertical launch section. The time-integrated atomic-beam fluorescence (triangles) is shown vs the integration time for the indicated launch velocities. At time zero, the atomic flux out of the MMOT is suddenly increased by about a factor of five. The time-of-flight distributions (curves peaking at about 100 ms) are obtained by twice differentiating the smoothed curves laid through the data points.

Neglecting magnetic retardation effects [25] in the compression region of the magnetic guide, it is straightforward to convert the time-of-flight curves in Fig. 4.3 into a distribution of velocities at the observation point. The corresponding estimate for the longitudinal temperature $T_{\|}$ of the atoms is found to be $T_{\|} \sim 900\ \mu$K. Since the retardation depends on the transverse energy distribution [25], it broadens the time-of-flight signal relative to the signal one would obtain without retardation. Thus, the estimate $T_{\|} \sim 900\ \mu$K provides an upper limit of the actual value $T_{\|}$. We have performed simulations in which the exact guide fields were used and thus retardation effects were fully accounted for. Assuming MMOT temperatures $T_{\|} = 300\ \mu$K and $T_{\perp} = 250\ \mu$K ($T_{\perp} = 150\ \mu$K is the Doppler limit for Rb), the simulations yield $T_{\|} = 890\ \mu$K in the probe region, which is compatible with the experimentally obtained upper limit.

It is noted that in our current MMOT configuration a value of $T_\perp$ greater than the Doppler limit is expected. Images of the MMOT, such as those shown in Fig. 2.6, typically show incomplete narrowing of the atomic beam at the extraction point of the MMOT. As discussed in Sec. 2.2.3, this observation indicates less than optimal cooling in the transverse directions.

4.2 Atomic-beam analysis at the end of the atom guide

4.2.1 Measurement of the transverse temperature

The vertical injection/launch section of the guide is connected with the 1.5 m long horizontal section via a 90° bend with a radius of 1 inch. Considering this geometry as well as the centrifugal force and the transverse gradient of the atom guide in the bend region, it is found that atoms with launch velocities in the range 2 m/s $< v_0 <$ 3.8 m/s will be able to transit into the horizontal guide section. Experimentally, a smaller useful range of 2.2 m/s $< v_0 <$ 2.8 m/s is found. We believe that on the low-velocity side the useful v_0-range is limited by reflection of slow atoms in the magnetic-compression region [25], while on the high-velocity side it is caused by limitations in the MMOT operation. In view of the long-term goals of our work, we are mostly interested in the low-velocity end of the useful v_0-range.

In the horizontal guide section, the center-to-center distance between the guide tubes linearly decreases from 5.18 mm after the bend to 4.18 mm at the end. Thus, at 300 A guide current the magnetic-field gradient increases from 1.7 kG/cm to 2.7 kG/cm, leading to a further moderate adiabatic compression of the atom flow.

Using the same methods as described in Sec. 4.1.1, atomic-beam images and corresponding temperature fits have been performed at the end of the guide. Fitting the data from a repumper-only measurement, as shown in Fig. 4.4, with functions of the type Eq. 4.1, we find a transverse temperature $T_\perp = 420\ \mu\text{K} \pm 40\ \mu\text{K}$. Also, as shown in Fig. 4.5, a temperature fit of $T_\perp = 350\ \mu$K was determined by the probe-repumper type measurement. Following the discussion in Sec. 4.1.1, the temperature obtained with the probe-repumper method is considered less reliable.

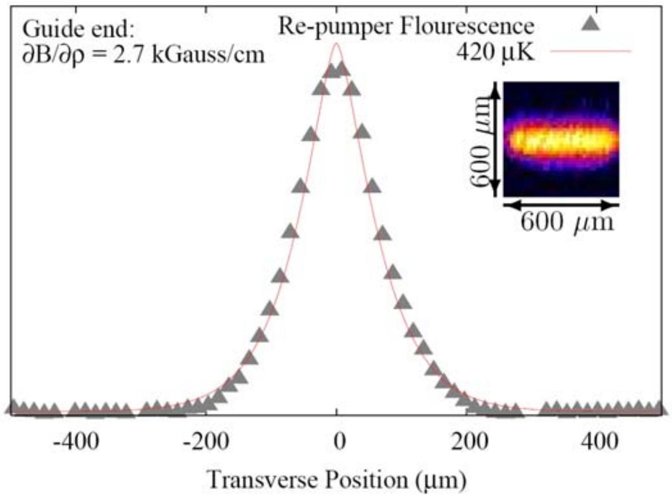

Figure 4.4: Fluorescence image of the atomic beam at the end of the guide. Atomic-beam image obtained at the end of the atom guide with re-pumping light only (inset), and corresponding profile transverse to the guide axis (data points) are shown in the figure. In the image, the guide axis is horizontal. The line through the data points represents a fit for a temperature of 420 μK.

4.2.2 Measurement of the longitudinal temperature

In the horizontal section of the guide, a time-of-flight experiment has been performed. At a location 50 cm ahead of the detection region, a laser beam tuned to the re-pumping transition ($F = 1 \rightarrow F' = 2$) is introduced. This beam is on most of the time and strongly attenuates the atomic beam. An interruption of this re-pumper beam for 50 ms defines a short pulse of guided atoms that is allowed to propagate through the length of the guide into the probe region located at the end of the guide. By measuring the temporal spread of the atom pulse, the longitudinal velocity distribution of the atomic beam is derived. A typical result is shown in Fig. 4.6. Fitting the velocity distribution with functions of the type

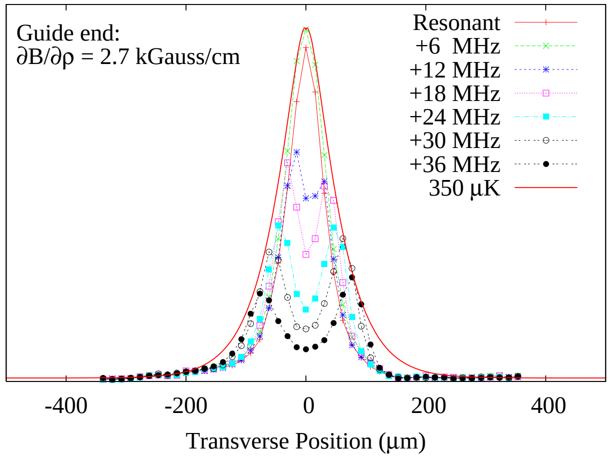

Figure 4.5: Measurement of the atomic beam temperature using the probe laser detuning. This figure shows the profiles of atomic-beam images transverse to the guide axis with both re-pumper light and probe light present in the detection region for the indicated de-tunings of the probe laser relative to the field-free transition frequency. The estimate $T_{\perp} \approx 350$ μK is obtained by fitting the *envelope* of the profiles with curves of the type from Eq. 4.2.

$$P(v) \propto \exp\left[-\frac{M(v-v_{\mathrm{c}})^2}{2k_{\mathrm{B}}T_{\parallel}}\right] \quad ,$$

we find, for the case displayed in Fig. 4.6, a longitudinal temperature of $T_{\parallel} \approx 1$ mK and an average forward velocity of $v_{\mathrm{c}} \approx 1.2$ m/s. Since in this measurement the tapering of the atom guide along the lime-of-flight stretch was minimal, the values of $T_{\parallel}$ and v_{c} are reliable.

4.2.3 Temperature changes along the guide

In the following, the changes in transverse temperature that occur along the guide are discussed. The first notable change in temperature occurs between the MMOT and the upper end of the magnetic-compression zone in the vertical launch section of the guide. While maintaining the phase-space density of the atoms, the compression has the side effects of retarding their forward motion and heating them both transversely and longitudinally. In a trajectory simulation in which temperatures of $T_{\parallel} = 300$ μK and $T_{\perp} = 250$ μK at the exit of the MMOT are assumed, the transverse

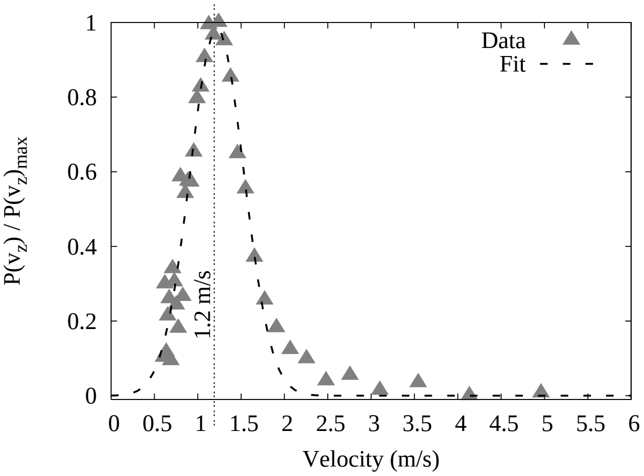

Figure 4.6: Longitudinal velocity distribution obtained from a time-of-flight experiment in the horizontal section of the atom guide. The MMOT launch velocity is $v_0 = 2.2$ m/s. The velocity distribution yields a longitudinal temperature of ≈1 mK and an average forward velocity of ≈ 1.2 m/s.

temperature shows an increase to $T_\perp$ to 600 μK $\pm$ 40 μK at the observation point used in Sec. 4.1.1 (the error bar arises from statistical noise in the simulation). This simulation result is in reasonable agreement with the experimental result.

The results of Sec. 4.1.1 and Sec. 4.2.1 further indicate a considerable decrease in $T_\perp$ between the respective observation points. This decrease is a secondary consequence of magnetic compression. Since the action of the transverse motion is adiabatically conserved, during the compression longitudinal energy becomes partially converted into transverse energy [25]. Thereby, the amount of energy that is converted increases with increasing transverse energy. Due to this interdependence, the longitudinal velocity distributions and the transverse positions in Figs. 4.1 and 4.4 are not independent. The further off-axis an atom travels the slower it is longitudinally. Since between the observation points of Figs. 4.1 and 4.4 the atoms undergo a final 1.6 cm vertical climb, the further out an atom is in Fig. 4.1 the higher the chance that it does not make the climb and falls back into the MMOT. Thus, there is a trend that between the observation points of Figs. 4.1 and 4.4 the outermost atoms fall back. This effect causes the transverse temperature to decrease. Simulations show that the transverse temperature decreases from $T_\perp \approx 600\ \mu$K to $425\ \mu\text{K} \pm 35\ \mu$K during the final 1.6 cm of vertical climb. This simulation result agrees well with the experimentally observed temperature drop.

4.3 Flux measurement

Using atomic-beam images obtained with the re-pumper only, a measurement of the atomic flux in the guide has been performed. The method relies on the fact that the total photon yield per atom for re-pumper light is quite well known (simulations show about two photons per atom). Important parameters entering into the calculation are the geometric collection efficiency of the camera lens, as well as the pixel yield of the camera per photon reaching the CCD chip.

An analysis along these lines for a launch velocity of 2.5 m/s has yielded an atomic flux of $1.9 \times 10^7\ \text{s}^{-1}$ and a central volume density of about $1.2 \times 10^9\ \text{cm}^{-3}$ at the end of the guide, with uncertainties less than a factor of two. The s-wave elastic collision rate (cross section $\sigma = 700\ \text{nm}^2$) at this density and at a temperature of $500\ \mu$K is about 0.5 per second, corresponding to of order one elastic collision of any given atom during its passage through the atom guide. Therefore, under the present conditions collisions will barely affect the dynamics of the atomic flow and of RF-induced atom removal, discussed next.

The flux measured at the end of the guide amounts to approximately 4% of the MMOT output flux. This result is about a factor of four less than our initial estimate at the end of Sec. 2.3. We attribute this disparity to the depleting effect of stray repumper light in the vertical section of the guide, which optically pumps atoms from the guided state $|F = 1, m_\text{F} = -1\rangle$ into other states. We have found very recently that this effect can be alleviated by de-tuning the re-pumper laser that is coupled into the MMOT region. Using a de-tuned re-pumper, a flux increase of about a factor of five at the end of the guide was observed.

4.4 Continuous RF-induced energy-selective removal of atoms

An RF-current is coupled onto one of the guide tubes in the horizontal guide section. Since most of the RF-induced magnetic field is confined to the region between the tubes, this RF-coupling scheme requires little RF power and minimizes RF interference. The RF magnetic field is transverse to the guide axis and has a component transverse to the local static magnetic field practically everywhere on the evaporation surface. RF induced removal of atoms has been performed previously using a different antenna geometry [11, 12].

Fig. 4.7 shows profiles of the atomic beam at the end of the guide for continuously applied RF-currents at a frequency of 9 MHz and the indicated estimated values of the RF magnetic-field amplitude. At 9 MHz RF frequency, a large portion of the atomic beam is above the evaporation threshold $2\pi\hbar\times 9$ MHz (= the "RF knife-edge") and should become removed if the RF-coupling scheme is effective. Fig. 4.7 shows that an applied RF field of $B_{\mathrm{RF}} = 500$ mG is sufficient for continuous RF-induced removal of practically all atoms above the "RF knife-edge". In the figure, we also compare the measured fluorescence profiles with a fit for a thermal distribution function ($T_\perp = 500\ \mu$K, red curve in Fig. 4.7) and the same distribution truncated at an energy of $2\pi\hbar \times 9$ MHz. There is reasonably good agreement between the calculated curves and the respective measured profiles with no RF and $B_{\mathrm{RF}} = 500$ mG.

It is noted that the experimental curves are wider than the calculated ones by $\sim 20\ \mu$m. The experimental broadening is due to diffraction effects and image smearing associated with the camera pixel size. Integrating the experimental data in Fig. 4.7, it is found that 16% of the atoms are left after energy-selective removal of atoms exceeding a transverse energy of $2\pi\hbar \times 9$ MHz. Using a calculation, the average potential energy of the atoms remaining after the RF-induced atom removal is found to equal ≈11 % of the average potential energy without RF-induced atom removal.

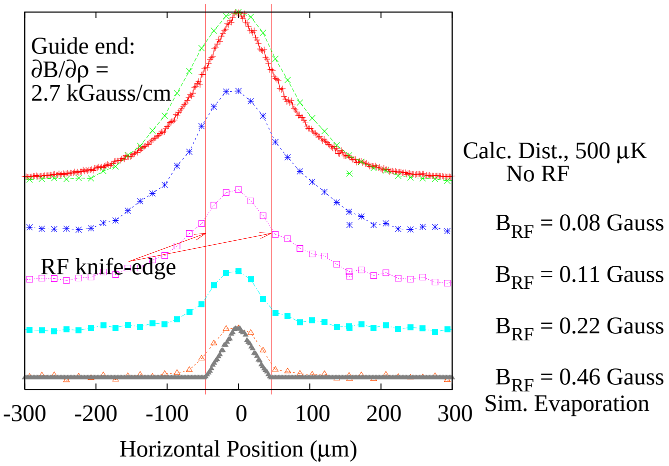

Figure 4.7: Radio-frequency filtering of the atomic beam. Atomic-beam profiles transverse to the guide axis at the end of the atom guide, obtained with re-pumping light only and with a continuous radio-frequency (RF) current of 9 MHz frequency, are shown in this figure. The RF current is coupled onto a guide tube in the horizontal guide section and is generated with the indicated drive voltages. RF-induced removal of atoms outside the indicated "RF knife-edges" is clearly visible. The RF-induced atom removal saturates at about $B_{\mathrm{RF}} = 500$ mG. The experimental data agree reasonably well with calculations for a thermal distribution with $T_{\perp} = 500\ \mu$K (red curve) and the same thermal distribution truncated at the "RF knife-edge" (gray curve). Both theoretical curves are scaled with the same factor to match the experimental data.

4.5 Discussion

We have realized a continuous flow of atoms in a 1.7 m long magnetic atom guide and measured longitudinal and transverse temperatures of the guided atomic beam. Continuous RF-induced removal of the most energetic atoms from the guide has been demonstrated. There is no evidence that elastic collisions play a role in the observed atomic-flow dynamics.

To further evaluate the currently achieved performance, we calculate the number of quantum-mechanical atom-guide modes in the plane transverse to the guide axis via a semi-classical analysis in cylindrical coordinates. The number of modes with an outer turning point less than ρ_0 is given by

$$N_{\mathrm{modes}} = \sum_{m=-\infty}^{\infty} \frac{2}{h} \int_{\rho_{\mathrm{min}}}^{\rho_0} \sqrt{2M\left(E_{\mathrm{m}}\left(\rho_0\right) - E_{\mathrm{m}}\left(\rho\right)\right)} d\rho$$

where the potential energy

$$E_{\mathrm{m}}\left(\rho\right) = \frac{\hbar^2\left(m^2 - 1/4\right)}{2\rho^2} + \left|\frac{\partial B}{\partial \rho}\mu_{\mathrm{B}} g_{\mathrm{F}}\right| \rho \quad ,$$

the angular momentum about the guide axis $l_{\mathrm{z}} = \hbar m$, and ρ_{min} is defined via $E_{\mathrm{m}}\left(\rho_{\mathrm{min}}\right) = E_{\mathrm{m}}\left(\rho_0\right)$ (let $\rho_{\mathrm{min}} \to 0$ for $m = 0$). To estimate the number of modes that carry a significant flow, from Fig. 4.7 we estimate for the case where no RF is applied $\rho_0 = 100$ μm and obtain $N_{\mathrm{modes,noRF}} = 3.5 \times 10^8$, while for the case of RF-induced energy filtering we estimate $\rho_0 = 40$ μm and obtain $N_{\mathrm{modes,withRF}} = 3.6 \times 10^7$. Assuming that the atom flux is the same in all significant guide modes, the flux per mode is about $\Phi_1 = 0.2\ \mathrm{s}^{-1}\mathrm{mode}^{-1}$. Assuming that one were to build an atom interferometer based on filtering the atomic beam in a way that only the fundamental guide mode enters the interferometer, this flux per mode would correspond to the count rate. Reasonable experiments will require a count rate of order $10^3\mathrm{s}^{-1}$. Therefore, an increase of the phase-space density by a factor of order 10^4, combined with mode filtering techniques, will be sufficient to perform atom-interferometric experiments in the guide. This increase could be obtained by implementing a larger initial flux, using for instance a Zeeman slower, and some degree of evaporative cooling enabled by an improved collision rate. Further, the present phase-space density, estimated to be $h\Phi_1/(M\Delta v_{\mathrm{z}}\langle v_{\mathrm{z}}\rangle) \sim 10^{-9}$, needs to be increased by a factor of order 10^9 to reach a quantum-degenerate atomic flow.

CHAPTER V

Zeeman Slower

The pyramidal magneto-optical trap (PMOT) is the current low velocity intense source of atoms for the guide, as seen in Chapter II. The flux from the PMOT is 1×10^9 atoms-s^{-1}. This input flux to the guide yields a throughput flux of $\sim 10^7$ atoms-s^{-1} through the guide. We found that this gives rise to a nearly ballistic flow of atoms through the guide, with each atom undergoing 1-2 collisions during travel. However, for evaporative cooling to be efficient through the length of the guide, each atom has to undergo at least 500 collisions in the guide for effective re-thermalization to take place. Simulations have shown that if the atomic flux through the guide is 3×10^9 atoms-s^{-1}, for certain evaporative ramp configurations, the guided atomic beam can reach quantum degeneracy. However, because the input flux to the guide is less than the desired guide throughput, a new source of low velocity atoms with an output flux of at least 10^{11} atoms-s^{-1} is needed, assuming constant transfer efficiency. A Doppler-slowed beam of atoms provides just the solution to this problem. This source, popularly known as the Zeeman Slower, can be tuned to achieve flux as high as 3×10^{12} atoms-s^{-1}, making it an ideal choice for the low velocity intense source of atoms for the next generation of the magnetic guide. In this chapter, I describe how the Zeeman Slower works. In section 5.1, I briefly describe the theory of operation of the Zeeman Slower, along with the different configurations in which it can be implemented. The next section 5.2 gives details of the design of the Zeeman Slower we have implemented in this lab. Section 5.3 gives the details of the oven used to generate the input atomic beam to the Zeeman Slower. The characteristics of the slowed atomic beam along with the method of characterization are given in Section 5.4. Section 5.5 discusses the improvements that can be made in the Zeeman Slower to improve its performance even further.

5.1 Theory of operation

5.1.1 Radiation pressure

The Zeeman slowing technique is based on the principle of radiation force, described below. When an atom scatters a photon, the atomic momentum by $\hbar(\vec{\mathbf{k}}_l - \vec{\mathbf{k}}')$, where $\vec{\mathbf{k}}_l$ is the laser wave-vector and $\vec{\mathbf{k}}'$ is the wave-vector of the photon scattered in a random direction [1]. Over $n \gg 1$ scattering events, $\sum_n \vec{\mathbf{k}}' = 0$ and the change in the momentum of the atom is $n\hbar\vec{\mathbf{k}}_l$, The corresponding change in speed is given by $\delta v_a = n\hbar k_l/m = nv_{recoil}$, where $v_{recoil} = \hbar k_l/m$ is the recoil velocity. For ^{87}Rb, $v_{recoil} = 6.02$ m-s^{-1}. For example, to slow down an atom from 300 m-s^{-1} to 15 m-s^{-1} requires $\sim$ 47000 photons to be scattered off of the atom.

This dissipative force F_{rad} an atom experiences due to spontaneous emission , called the radiation force, can be derived from the Optical Bloch Equations [8] and is given by:

$$F_{rad} = \hbar k \frac{\Gamma_{scat}}{2} \frac{s_0}{1 + s_0 + (2\delta/\Gamma_{scat})^2} \tag{5.1}$$

Here, $\Gamma_{scat} = \tau^{-1}$ is the photon scattering rate, τ is the excited state lifetime, δ_{total} is the detuning of the laser from the atomic transition frequency, and

---

[1] The emission direction is not entirely random but follows the dipole radiation pattern, which depends on the incident light polarization and the exact scattering parameters.

$s_0 = \mathrm{I}/\ I_{sat}$ is the saturation parameter. I_{sat} is the saturation intensity given by:

$$I_{sat} = \frac{\pi h c}{3\lambda_0^3 \tau} \tag{5.2}$$

where λ_0 is the wavelength of the atomic transition. It is then apparent that for incident laser intensity much higher than saturation intensity, that is $s_0 \gg 1$, the force due to spontaneous emission saturates at a value ${F_{rad}}^{max} = \hbar k \Gamma_{scat}/2 = \hbar k/2\tau$. This can be intuitively explained as follows[30]. When the atomic transition is saturated, an atom spends half the time in the excited state and half the time in the ground state. Hence, on average, the atom scatters one photon every 2τ and gets a momentum kick of $\hbar k$. Thus, the maximum force is simply change in momentum per unit time or $\hbar k/2\tau$ giving a maximum acceleration due to radiation force of $a_{max} = \Gamma_{scat}\hbar k/2m$, m being the mass of the atom. For ^{87}Rb, $\Gamma_{scat} = 2\pi\ 5.98{\times}10^6 \mathrm{s}^{-1}$ giving a maximum accleration of $a_{max} = 1.13 \times 10^5$ m-s^{-2}.

5.1.2 Doppler detuning

Just using radiation force to slow an atomic beam down, however, is not very efficient due to Doppler detuning. Doppler detuning is the change in the observed frequency of an oscillating field due to the relative motion between the source and the observer.

The frequency of a laser beam in the frame of reference of an atom moving with a velocity $\vec{\mathbf{v}}_a$ is given by $\omega_l' = \omega_l - \vec{\mathbf{k}}_l \cdot \vec{\mathbf{v}}_a$. This change in the laser frequency seen by the atom is known as the Doppler detuning $\delta_D = \vec{\mathbf{k}}_l \cdot \vec{\mathbf{v}}_a$. As an atom gets decelerated due to radiation force, the Doppler detuning experienced by the atom increases, that is the term δ in Equation 5.1 increases, decreasing the radiation force. If an intense laser beam is used, the atoms quickly slow down and get Doppler-tuned out of resonance. For ^{87}Rb, the change in speed required to increase δ from 0 to 3 Γ_{scat} is just

$3\Gamma_{scat}/\vec{\mathbf{k}}_l$ ~14 m-s^{-1}, corresponding to just 14m-s$^{-1}/v_{recoil}$~2300 photon scattering events. Hence, to slow an atomic beam down from 300 m-s^{-1} to 20 m-s^{-1} at which speed it can be captured by a MOT, either the laser detuning has to be changed as the atomic velocity decreases or the atomic transition frequency has to be modified such that the atomic transition is always in resonance with the laser frequency.

The method of changing the laser frequency, or chirping, was used to slow atomic beams by Ertmer, *et al* [31]. In this method, the laser frequency is changed to compensate for the changing Doppler detuning as the atoms are decelerated so as to maintain the resonance condition. However, the main disadvantage of this scheme is that only pulses of slow atoms can be produced. Using electric fields to change the atomic frequency through Stark effect has also been demonstrated by Gaggl, *et al* [32]. The high values of electric fields involved to produce the Stark shift limit the usefulness of this method in common applications. The most common method to compensate for the Doppler detuning by far has been using magnetic fields to tune the atomic transition using the Zeeman effect. In this scheme, a spatially varying magnetic field is applied along the atomic trajectory. The magnetic field is designed such that as the atoms in the beam slow down, the change in Doppler detuning is compensated by a corresponding change in the Zeeman shift of the atomic transition, thus ensuring that the atoms scatter photons at a maximal rate and experience the maximum possible deceleration along the atomic beam.

5.1.3 Zeeman tuning of atomic transition

As seen in Chapter II, the energy of an atom in the hyperfine state $|F, m_F\rangle$ in a magnetic field $\vec{\mathbf{B}}$ is perturbed by an amount $V_M = g_F m_F \mu_B \left|\vec{\mathbf{B}}\right|$, where g_F is the electron gyro-magnetic ratio for the hyperfine manifold and μ_B is the Bohr magneton. Here, we have chosen the direction of the local magnetic field as the quantization axis. Thus, if the ground and excited states of the atoms experience different Zeeman shifts for a given magnetic field $\left|\vec{\mathbf{B}}\right| = \mathrm{B}$, then the magnetic field can be used to vary the transition frequency. For ^{87}Rb, the same cycling transition used in a MOT, as described in II is used to slow the atoms. The ground state for this transition is $|g\rangle = \left|{}^5S_{1/2}, F = 2, m_F = \pm 2\right\rangle$ and the excited state is $|e\rangle = \left|{}^5P_{3/2}, F = 3, m_F = \pm 3\right\rangle$, with the g-factors being $g_{F=2} = 1/2$ and $g_{F'=3} = 2/3$ respectively. Hence, in presence of a magnetic field, the Zeeman shifts for the ground and the excited states are as follows:

$$\begin{aligned} V_M^{|g\rangle} &= \pm\frac{1}{2}2\mu_B B = \pm\mu_B B \\ V_M^{|e\rangle} &= \pm\frac{2}{3}3\mu_B B = \pm 2\mu_B B \end{aligned} \tag{5.3}$$

This leads to a perturbation in the transition energy of:

$$\Delta V_M = V_M^{|e\rangle} - V_M^{|g\rangle} = \pm\mu_B B$$

or a frequency shift of

$$\omega_{field} = \Delta V_M/\hbar = (\mu_B/\hbar)\, B.$$

The constant $\mu_B/\hbar$ =1.4 MHz-G^{-1}.

Figure 5.1 shows the Zeeman shifts of the ground and the excited hyperfine manifold of ^{87}Rb. The hyperfine basis is an orthogonal basis for the ground state for magnetic fields up to 5 kG. In other words, F is a good quantum number for describing an atom in ground state in magnetic fields up to 5 kG. However, for the excited state, the hyperfine approximation breaks down even for moderately high magnetic fields or >60 G and the $|m_I, m_J\rangle$ basis need to be used, as was seen in Chapter III. But the extreme hyperfine states $|F' = 3, m_{F'} = \pm 3\rangle$ can only be decomposed into $|m_I = 3/2, m_J = 3/2\rangle$ and $|m_I = -3/2, m_J = -3/2\rangle$. Consequently, these remain

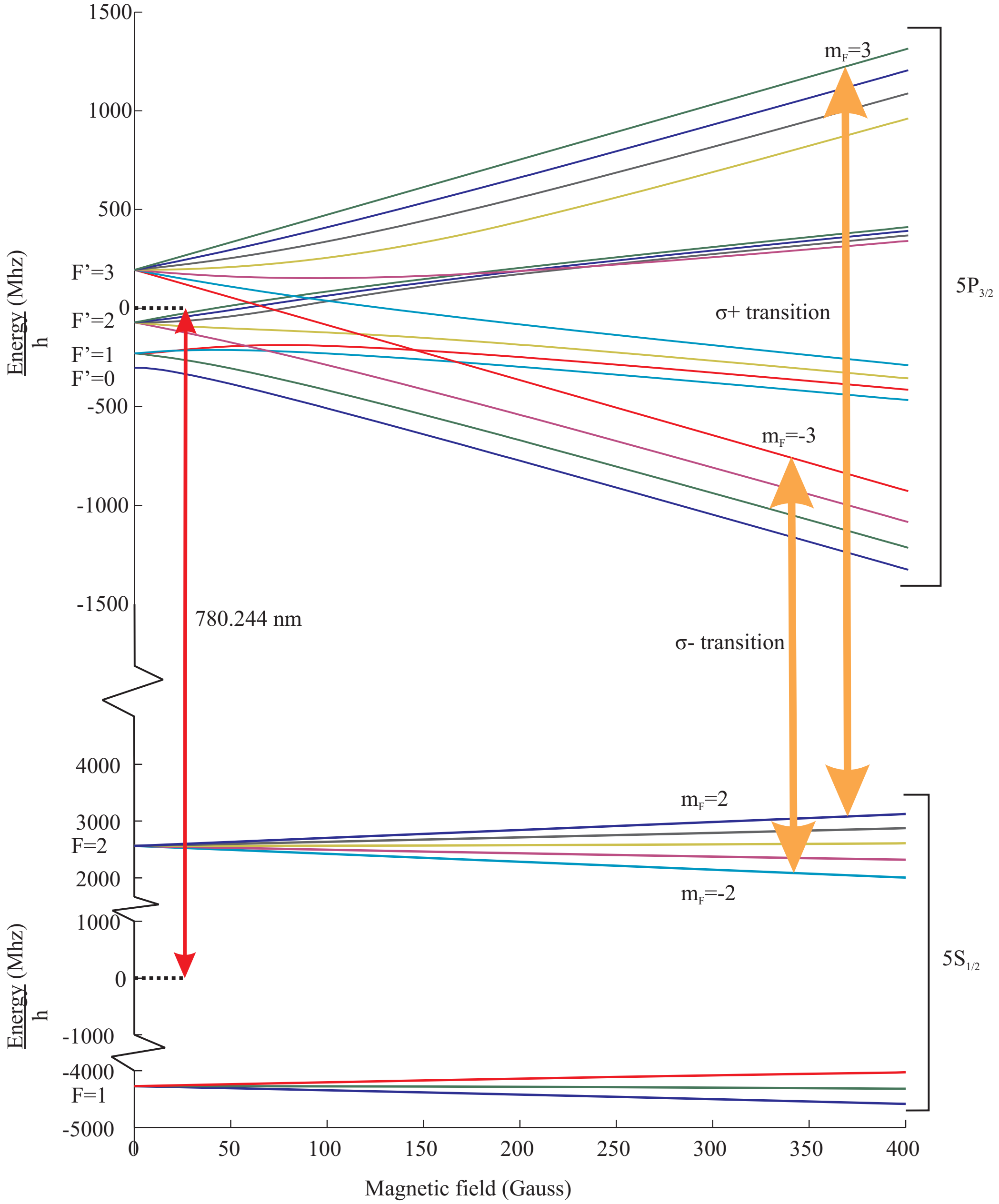

Figure 5.1: Zeeman effect and cycling transitions. The Zeeman shifts of atomic states calculated for the ground state $5S_{1/2}$ and excited state $5P_{3/2}$ hyperfine manifolds are shown with reference to the fine-splitting. The two cycling transitions are indicated. These transitions are used to slow the atoms down using radiation force. The calculations were done in the $|m_I, m_J\rangle$ basis. The effect of the quadratic Zeeman splitting can be explicitly observed in the excited state energies.

stationary states of the Hamiltonian even in presence of relatively strong magnetic fields, as is seen in Figure 5.1. Hence, the Equation 5.3 remains valid even in this regime.

Thus, for an atom traveling with a velocity $\vec{\mathbf{v}}_a$ in presence of laser light of frequency ω_l and a magnetic field $\vec{\mathbf{B}}$, the total atom-field detuning can be written as:

$$\begin{aligned} \delta_{total} &= \omega_l - \omega_a - \delta_D \\ &= \omega_l - \omega_0 - \omega_{field} - \vec{\mathbf{k}}_l \cdot \vec{\mathbf{v}}_a \\ &= \delta_l \mp \frac{\mu_B}{\hbar} B - \vec{\mathbf{k}}_l \cdot \vec{\mathbf{v}}_a \end{aligned} \tag{5.4}$$

Substituting the resonance condition $\delta_{total}= 0$ in Equation 5.4, for a laser beam and an atomic beam in the counter-propagating configuration:

$$\delta_l \mp \frac{\mu_B}{\hbar} B + k_l v_a = 0 \tag{5.5}$$

Here, the negative sign on the Zeeman shift represents driving the $\Delta m_F = 1$ transition using σ^+-polarized light and the positive sign represents driving the $\Delta m_F = -1$ transition using σ^--polarized light.

5.1.4 Calculating the magnetic field profile

The Zeeman slower consists of an atomic beam propagating in vacuum subjected to a designed magnetic field and a counter-propagating laser beam such that the resonance condition described in Equation 5.5 is satisfied. To calculate the magnetic field profile, we assume that the atoms enter the Zeeman slower at $z = 0$ with velocity $\vec{\mathbf{v}}_a(0) = v_0$ and undergo a constant deceleration a which is a fraction $\eta \sim 75\%$ of the maximum acceleration a_{max}. Thus, the velocity of the atoms at any location along the Zeeman slower axis is $\vec{\mathbf{v}}_a(z) = sqrt(v_0^2 - 2az)$. If the laser detuning $\delta_l = 0$, using the resonance condition from Equation 5.5, the magnetic field profile can be written as:

$$B'(z) = B_0\sqrt{1 - 2\eta a_{max} z \frac{\vec{\mathbf{k}}_l^2 \hbar^2}{{\mu_B}^2 B_0^2}} \tag{5.6}$$

This profile, as shown in curve (A) of Figure 5.2, corresponds to slowing an atomic beam with laser tuned to the field-free atomic resonance with σ^+ polarization. However, the disadvantage of this scheme is that as the atoms exit the slower, they scatter the resonant photons and are pushed back into the slower [33]. To overcome this disadvantage, a bias field is added to the magnetic field profile. The bias field is constant throughout the slowing region and has a sharp drop-off at the end where the atoms exit the slower, such that the atoms cannot follow the magnetic field any more and are tuned out of resonance. Thus, for a specified input velocity v_0, exit velocity $v_L = \vec{\mathbf{v}}_a(L)$ and the field-free laser detuning δ_l, the peak magnetic field B_0 of Equation 5.6, the bias magnetic field B_{bias} and the length L of the slower can be calculated using the following set of equations:

$$\begin{aligned} k_l v_0 &= \delta_l + \frac{\mu_B}{\hbar}(B_0 + B_{bias}) \\ k_l v_L &= \delta_l + \frac{\mu_B}{\hbar} B_{bias} \\ v_L &= \sqrt{v_0^2 - 2aL} \end{aligned} \tag{5.7}$$

The length of the slower is thus calculated to be:

$$L = \frac{v_0^2}{2\eta a_{max}}. \tag{5.8}$$

The bias magnetic field is:

$$B_{bias} = \frac{\hbar}{\mu_B}(k_l v_L - \delta_l) \tag{5.9}$$

and the peak magnetic field is:

$$B_0 = \frac{\hbar k_l}{\mu_B}(v_0 - v_L) \tag{5.10}$$

Thus, putting it all together, the slower magnetic field follows the profile:

$$B(z) \quad = \quad B_{bias} + B_0\sqrt{1 - 2\eta a_{max} z \frac{k_l^2 \hbar^2}{{\mu_B}^2 B_0^2}} \tag{5.11}$$

The laser detuning is selected so as to provide a stable lock-point for the laser. For ^{87}Rb, the 2-3 cross-over peak provides such a stable lock-point, with a detuning δ_l=$2\pi\times$134 MHz. To slow an atomic beam from an initial velocity of v_0 =355 m-s^{-1} to a final velocity of v_L =15 m-s^{-1} hence requires the length of the slower to be 75 cm, with B_{bias} = 82 G and B_0 = 310 G. The ideal magnetic field for the Zeeman slower was designed with these parameters, and is shown in curve (d) of Figure 5.2.

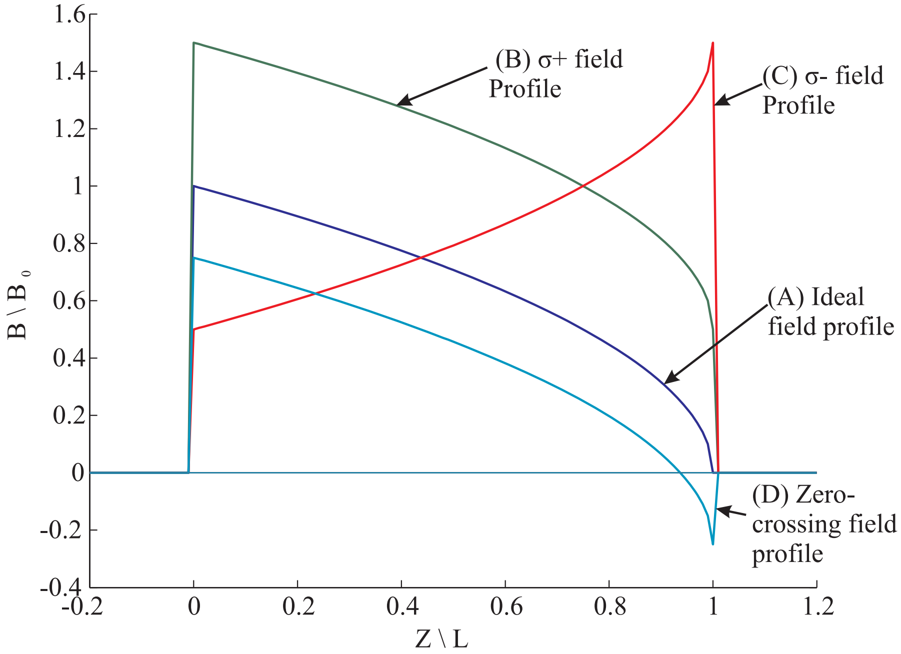

Figure 5.2: Magnetic field profiles for different configurations. This figure shows the magnetic field profiles for various configurations as labeled. The magnetic field is normalized to B_0 given by Equation 5.10 and the length of the slower is normalized to the length of the slower L given by Equation 5.8. The offset field is 0.5B_0 for the σ^+ and σ^- configurations and -0.25B_0 for the zero-crossing configuration.

Depending on the direction and the magnitude of the bias field, three magnetic field configurations are possible.

- σ^+ **configuration:** This is the "decreasing field" configuration where the laser beam wave-vector is co-aligned with the magnetic field. The laser beam has σ^+

polarization, hence the name. The magnitude of the magnetic field decreases along the slower as shown in curve (B) of Figure 5.2. However, implementing a very sharp magnetic field drop-off at the slower exit, which is necessary to prevent the slowed atoms from being pushed back into the slower, is very difficult in this configuration. Hence, this configuration is rarely used.

- σ^- **configuration:** This is the "increasing field" configuration where the laser beam wave-vector is counter-aligned with the magnetic field. The laser beam has σ^- polarization. The magnitude of the magnetic field increases along the slower, as shown in curve (C) of Figure 5.2. This configuration has the advantage that the slowed atomic beam is less sensitive to fluctuations in laser frequency and intensity [34]. Also, the implementing a large magnetic field gradient at the slower exit is relatively simple. However, this configuration suffers from the disadvantage that the magnetic field value is very high at the slower exit. This high value needs to be offset further downstream if the beam is used to load a MOT, or if transverse optical molasses cooling is to be performed, which requires sub-Gauss stray magnetic fields. Secondly, the Zeeman shifted energy levels of the excited state for high values of magnetic fields at the exit mix, leading to inefficiencies in the slowing process and requiring the presence of a repumping beam to offset consequent optical pumping into dark state.
- **Zero-crossing configuration:** As the name suggests, the magnetic field crosses zero along the axis of the slower in this configuration, as shown in curve (D) of Figure 5.2. At the slower entrance, the magnetic field is co-aligned with the laser beam wave-vector, defined to be positive value, and at the exit, the magnetic field is counter-aligned with the laser beam wave-vector, defined to be negative value. The location along the slower where the magnetic field switches

sign (direction) depends on the exact parameters of the slower. This configuration avoids the disadvantages of the σ^- configuration, as the magnetic field at the slower exit is localized and has a relatively low value. However, the presence of a magnetic field zero along the slower leads to optical pumping into the dark state and a repumping beam has to be used. We have chosen to use this configuration for implementing our Zeeman slower.

An important constraint in designing the magnetic field is that the deceleration a that the atoms experience has be be less than a_{max} throughout the slower. This can be written as:

$$a = \frac{dv_a}{dt} = \frac{dv_a(z)}{dz}\frac{dz}{dt} = v_a(z)\frac{dv_a(z)}{dz} < a_{max} \tag{5.12}$$

Using Equation 5.4, this imposes the following condition on the magnetic field gradient:

$$\left|\frac{dB(z)}{dz}\right| < \frac{\hbar k_l a_{max}}{\mu_B v_a(z)} \tag{5.13}$$

Thus, designing the magnetic field with $a = \eta a_{max}$, where $\eta \sim 0.75$ ensures that the constraint imposed in equation 5.13 is satisfied throughout the slower, even in presence of small deviations of the actual magnetic field from the calculated ideal field profile given by Equation 5.11. Thus, the atoms experience a radiation force $F_{eff} = \eta F_{rad}$ corresponding to a non-zero total detuning given by:

$$\delta_{total} \;=\; \frac{s_0}{2}\sqrt{s_0+1}\sqrt{\frac{s_0}{s_0+1}\frac{a_{max}}{a} - 1} \tag{5.14}$$

One more advantage of having $a = \eta a_{max}$ is that the atomic beam is not only slowed but also cooled, i.e. the velocity distribution of the slowed atomic beam is compressed. This mechanism is described in detail by Bagnato *et al.* [35]. In summary, the deceleration that the atoms experience along the length of the slower will deviate from the ideal, designed value due to imperfections in the actual magnetic field profile as well as due to the stochastic nature of the slowing process due to spontaneous emission. Now, if the atoms at a particular location in the slower experience higher than expected deceleration, their velocity decreases such that the total laser detuning given by equation 5.4 decreases. Due to this, the deceleration decreases until the velocity of the atoms approaches the design velocity. A similar process ensures that the faster atoms experience higher deceleration and are slowed down more than the atoms at the average designed velocity. Thus, the slowing process is self-regulating and leads to cooling of the atomic beam along the axis of the Zeeman slower.

5.2 Design and Construction

5.2.1 Designing magnetic coils

The ideal magnetic field profile for the Zeeman slower is calculated as using Equation 5.11 with parameters $B_{bias} = -82\text{G}$, $B_0 = 310\text{G}$, $\eta = 0.75$ and length $L = 0.75\text{m}$. The Zeeman slower is of the "Zero-crossing" type. The magnetic field is implemented in the laboratory in two sections. The first section, called the positive coil, generates the slowly varying positive magnetic field along the Zeeman slower axis and is modeled by concentric solenoids of decreasing lengths, as shown in Figure 5.3. The rapidly varying negative magnetic field is generated by an annular disc called the extraction coil, shown in red in Figure 5.3. It consists of a thin wire wrapped around a coil form. The magnetic field along the Zeeman slower axis due to each of the concentric solenoids is calculated using the formula [36]:

$$B_{solenoid}(z) = \frac{\mu_0 N I_{solenoid}}{2} \left(\cos\left(\theta_1(z)\right) + \cos\left(\theta_2(z)\right) \right) \tag{5.15}$$

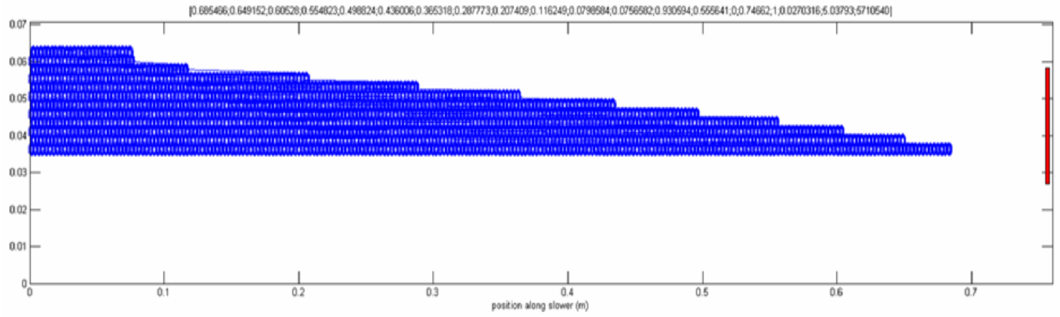

Figure 5.3: Section of the positive coils and the extraction coil. This figure shows the section of the positive and the extraction coils. The layered structure of the positive coils, referenced to the left edge, which is the input to the Zeeman slower, can be clearly seen. The bottom surface of the positive coil is at a radius of 1.375 in from the guide axis. The extraction coil is shown in red on the right side of the figure. Note the narrow dimensions, which help localize the extraction magnetic field.

where N is the number of turns per unit length, I is the current and $\theta_1(z)$ and $\theta_2(z)$ are the angles subtended by the point z on the slower axis with the ends of the solenoid, as shown in Figure 5.4. We modeled the extraction coil as a stack of current carrying loops. The magnetic field due to each of the loops at a position z along the axis is given by:

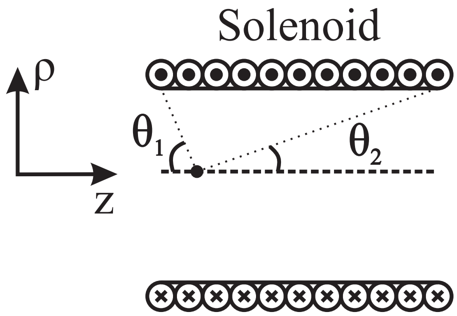

Figure 5.4: Schematic of a solenoid. The geometry considered in calculating the magnetic field on the axis of a solenoid is shown.

$$B_{loop}(z) = \frac{\mu_0}{4\pi} \frac{\pi R^2 I_{loop}}{\left(z^2 + R^2\right)^{3/2}} \tag{5.16}$$

where R is the radius of the loop. Eric Schomburg automated the process of finding the right physical parameters for the solenoids and the annular disc to match the ideal field profile as closely as possible using a genetic algorithm implemented by

Spencer Olson. It is clear that to closely match the ideal field profile, a very thin wire with a large number of layers and a large number of turns per unit length would be preferred. However, fabricating such a solenoid becomes very complicated, time consuming and prone to errors. We decided to try a number of different wire diameters for the solenoids from AWG10 to AWG12, with each with 8 to 12 layers. The genetic algorithm optimizes the following parameters such that the magnetic field due to the current geometry is the best match with the ideal field profile:

- The current through the solenoids,
- The length of each solenoid,
- The location of the extraction coil relative to $z = 0$,
- The inner and outer radii of the extraction coil, and
- The current through the extraction coil loops.

The current through each of the solenoid layers is assumed to be equal so that it can be fabricated without cutting the wire. While calculating the best fit, the constraint on the magnetic field gradient given in Equation 5.13 is also taken into account. We found that the parameters enumerated in Table 5.1 result in a magnetic field which best matches the ideal field, while still keeping the wire size and the number of layers reasonable.

5.2.2 Zeeman slower construction

The Zeeman slower itself consists of a 1 in diameter, 80 cm long steel tube with $2\,\frac{3}{4}$ in ConFlat flanges (CFF)on each end. The initial 70 cm of this tube is enclosed in a hollow jacket. The jacket has $\frac{1}{4}$ in FNPT pipe-threaded water inlet and outlet and a partition on the inside to channelize the water flow. This jacket is wrapped in heat-consecutive PTFE sheet. The positive solenoid coils are wrapped around this

12 layers of 10 AWG magnet wire on 23/4” tube	
Wire outer diameter	2.76 mm = 0.1087 in.
Positive coil current	5.04 A
Positive coil voltage	7.66 V
Positive coil power dissipated	38.6 W
Length for wire for positive coil	464 m = 1522 ft.
Extraction coil inner diameter	5.4 cm = 2.13 in.
Extraction coil outer diameter	11.68 cm = 4.6 in.
Extraction coil thickness	0.3 cm = 1/8 in.
Extraction coil current	3.77 A
Extraction coil voltage	5.3 V
Extraction coil power dissipated	20 W

Table 5.1: Zeeman slower optimized parameters. The parameters as optimized using a genetic algorithm are tabulated. These parameters were used in construction of the Zeeman slower.

jacket, one layer at a time on a lathe. 10 AWG, polyimide-coated wire procured from MWS, Inc. is used for the coils. The length of each layer conforms to the calculated lengths as described in the above paragraph. Every layer is painted over with quick-setting heat-conductive epoxy and let to dry before winding the next layer over it. The layers are bound on the input side of the Zeeman slower by a close-fitting annular acrylic disc, which is slipped on the flange before the coils are wound. This disc is stabilized with an aluminum disc, which is screwed to the flange and provides a stable support to the acrylic disc, an inlet to the positive coil wire, protects the flange during the winding process as well as has a conical dimple at the center of the outer fact to provide a hold for the lathe tailstock. The flange on the exit side of the Zeeman slower has a blank bolted on it and is held in the lathe chuck. After the positive coil is wound, the epoxy is allowed to set for a week on the lathe.

The extraction coil is wound according to the specifications calculated as described above. The coil form is made using annular aluminum discs. The discs are cut in half and assembled as a coil form on the tube such that the cuts are staggered and screwed together such that the structure is self-supporting. 20 AWG enamel-coated wire is used to wind the extraction coil and is protected from scratches and shorts

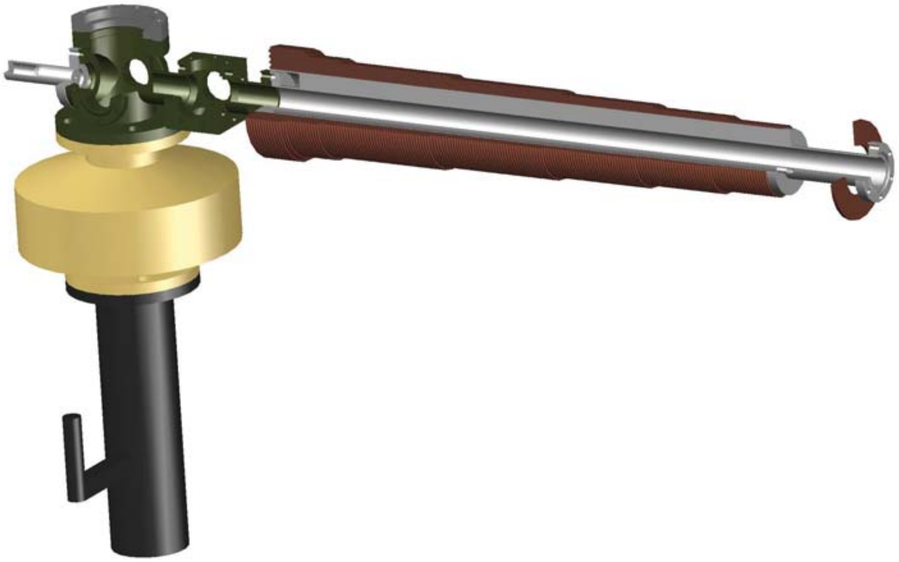

Figure 5.5: AutoCAD rendering of the Zeeman slower. This figure shows the vacuum construction of the Zeeman slower including the diffusion pump and the associated liquid Nitrogen cryotrap. The custom cross/cube vacuum part between the oven and the slower provides optical access for both the characterization and optical collimation of the the oven output atomic beam. The Zeeman slower positive and negative coils are shown on the vacuum tube and the baffle surrounding it for water-cooling the positive coils.

at the coil insertion point by wrapping PTFE tape around it. The extraction coil is water-cooled by wrapping the outside of the coil with a 0.125 in diameter copper tube, connected to the cooling-water loop. Good thermal contact is ensured by stuffing fine copper wool between the copper tube and the coil after wrapping the coil with heat-conducting polyimide sheet.

5.3 Recirulating oven design

5.3.1 Principle of operation

The source of the atomic beam to the Zeeman slower is a recirculating Rubidium oven, based on the design by Swenumson and Even [37]. The operation of this oven is based on the principles of baffling an atomic beam and capillary action. The oven essentially acts as a convection cell where the hot reservoir generates the Rubidium vapor. The relatively cooler baffles skim the atomic beam. The baffle temperature is maintained above the melting point of Rubidium which is 312.5 K. Combined gravimetric mass flow and capillary effect through the mesh surrounding the baffles provide the reflux action to transport the skimmed portion of the atomic beam from the baffles back to the reservoir.

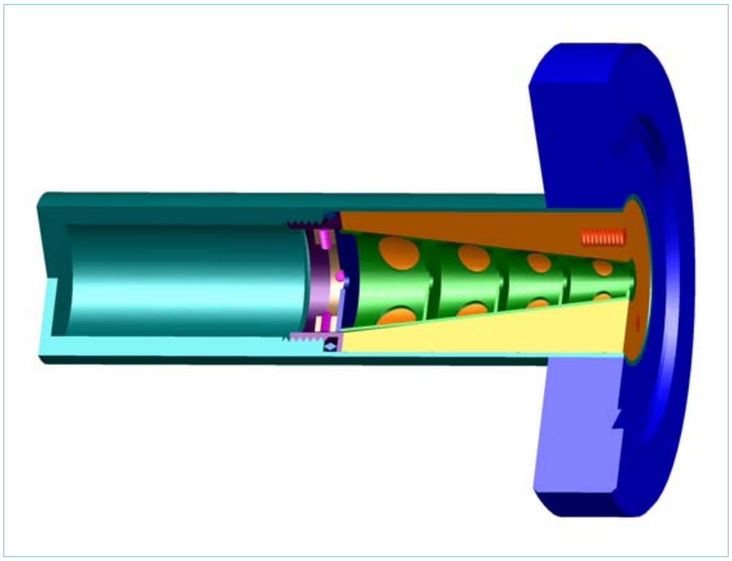

Figure 5.6: AutoCAD rendering of the recirculating Rb oven. This figure shows the schematic of the recirculating ^{87}Rb oven. The steel tube on the left houses a coil of steel mesh. When molten Rubidium is poured into this cavity, it wets the steel mesh and increases the exposed surface area. A layer of steel mesh is also inserted between the copper block and the baffles. This is required for the recirculation as it provides the capillary action to transport the excess Rubidium in the baffles back into the reservoir. All the effusive apertures are 0.125 in in diameter.

5.3.2 Oven Construction

A schematic of the recirculating oven design is shown in Figure 5.6. The oven is housed in a steel tube 1 in in diamater, with a 2.75 in CFF on side and the other side is closed, forming a reservoir. The housing is manufactured by appropriately machining a 1 in steel rod, 3.5 in in length. The bore of the housing has two sections: the reservoir section on the sealed end having an inner diameter of 0.75 in and the baffle container with an inner diameter of 0.94 in. The two sections are separated by a $\frac{13}{16}$-24 female pipe thread. The reservoir is stuffed with loosely coiled steel mesh procured from TWP, Inc., and has 325 grids per square inch with 1.4 mil wire diameter and 29% open area. In addition to increasing the Rubidium retention capacity of the reservoir, the steel mesh also improves the heat contact and the exposed surface area of molten Rubidium, aiding in temperature control, and prevents the molten Rubidium from forming a pool and sloshing in the reservoir. The increase in surface area inside the reservoir also significantly reduces the hydrostatic pressure, thus preventing back flow of liquid from the reservoir to the baffles.

The baffle container section houses a copper cylinder with a conical cavity, which contains the four skimming baffles. An aperture separates the reservoir from the baffled section. The aperture as well as the axial holes in the baffles have a diameter of 0.125 in. Thus, after the skimming action of the four baffles, a well-collimated atomic beam exits the oven. The baffles are conical, and are designed to fit the conical cavity in the copper block, with some slack worked in for the steel mesh. Each baffle is shaped like a bucket and has four holes in the side where the steel mesh is exposed to the skimmed atomic beam. The steel mesh provides reflux action through capillary effect to aid the transport of Rb from the baffles to the reservoir, and extends into the reservoir, overlapping the with steel mesh coiled inside the reservoir. The copper block provides excellent heat conduction between the baffles and the steel tube, thus making it easier to regulate the temperature of the baffles externally. The copper block has steel threads brazed on to it, and mate with the threads inside the steel housing. A knife edge made of hardened steel is sandwiched between the copper block and the ledge formed by the threads inside the steel housing. This knife edge compresses tantalum gaskets on each side, sealing the outside of the copper block from the reservoir. The baffles and the aperture are held in place inside the copper block using a retaining ring, which is attached to the inside of the brazed threads using three set-screws.

5.3.3 Oven assembly and observations

Before assembling the oven, all the parts are throughly cleaned, with sequential detergent, acetone, methanol and propanol washes in an ultrasonic cleaner, each for about 15 minutes. The steel mesh has to be especially well cleaned so that rubidium can completely wet the mesh. A mild acid wipe-down is recommended before the detergent wash to get rid of any oxide layers. The baffle and aperture are pre-assembled inside the copper block with the surrounding steel mesh cut to exact dimensions such that it does not overlap in the region between the baffles and the copper block. The entire assembly is then fixed with the retaining ring. An aluminum handle is screwed to the outside of the copper block to provide leverage while screwing the baffle assembly into the steel housing. The cleaned steel mesh is rolled and placed in the reservoir. Initially, a 5 gram load of Rubidium was used to charge the oven. The Rubidium was obtained in an ampule from Alfa Aesar, Inc. All the components were transferred to a glove box with Argon atomsphere. The Rubidium ampule is heated until all the metal has melted, then the top is broken off and the liquid Rubidium is poured into the reservoir. The copper block and baffle assembly is immediately screwed in and the oven is sealed with a rubber gasket and 2.75 in blank CFF. The assembled oven is then removed from the glove box and immediately cooled in liquid nitrogen to prevent the rubidium from oxidizing any impurities inside the oven. The oven is then uncapped near the Zeeman slower under nitrogen atmosphere and screwed on, and the Zeeman slower is immediately evacuated.

The reservoir section of the oven is enclosed in a 200 W mineral-insulated band heater (Hi-Watt, Inc., Part No. MB1A1JN4-B12), with a layer of copper mesh between them to improve thermal contact. The heater is controlled by a solid-state power control module form (Payne Engineering, Inc, Part No. 18TP-1-5), which gives a very fine control over the oven temperature. The oven temperature is monitored using a thermocouple probe. The baffle section of the oven need to be just above the melting point of Rubidium, and is force-air-cooled using a fan, to regulate its temperature to ~320 K. The oven temperature is maintained between 430-440 K generating a flux of $\sim 10^{15}$ atoms-s^{-1}, as determined by resonant light (probe) absorption measurements detailed in Chapter II. For a 5 gram Rubidium charge, the typical operational time is found to be approximately 300 hours. However, with a charge of 10 grams, the operation time is expected to be several thousand hours [37]. This is because it takes a minimum quantity of Rubidium ~4 gram to maintain the reflux action, and the oven does not operate below that charge.

5.4 Experimental parameters and results

5.4.1 Experimental setup

The experimental setup for the Zeeman slower is shown in Figure 5.5. It consists of the slower tube (see Section 5.2) and the oven (see Section 5.3) attached to a custom vacuum piece composed of a vacuum cube on the Zeeman slower side, a 4-1/2 in viewport on top, two 2-3/4 in viewports on sides near the oven and a 4-5/8 in CFF on the bottom. The Zeeman slower tube is attached to the custom vacuum piece using a copper gasket with a 1 cm diameter hole in it to provide differential pumping between the oven side and the slower side of the setup. An oil diffusion pump is attached through a cryo-trap to the 4-5/8 in CFF port. The vacuum cube is meant to provide optical access to optically collimate the atomic beam input to the slower. The optical access at the oven is used to measure the oven output, and the vertical viewport is used to visually inspect the oven nozzle for any clogging or malfunction. The diffusion pump attached (NRC Model HS4-750, type 161) has a pumping speed of 750 liters-s^{-1} and is pumped using a dual stage mechanical forepump (Varian DS-102). The cryo-trap between the diffusion pump and the vacuum chamber consists of a hollow baffle which is filled with liquid nitrogen during operation and prevents the diffusion pump oil from backstreaming into the vacuum chamber. However, it significantly reduces the effective pumping speed of the diffusion pump. On the output of the Zeeman slower, a four-way cross is attached, with the transverse ports occupied by an ion-getter pump with 40 liter-s^{-1} pumping speed (Varian model Vacion Plus 40 Starcell) and an ion guage (Varian model UHV-24P). A cube and a vacuum nipple are attached inline to the opposite side of the four-way cross. The cube has four viewports and is used to provide optical access for probe measurements of the slow atomic beam. The vacuum nipple has a viewport on other end through which the Zeeman slower laser beam is introduced.

The oven is heated to a temperature of 430 K in the normal course of operation, generating an effusive atomic flow. The velocity distribution of the atomic beam from an effusive source is given by [38]:

$$f(v) \quad = \quad \left(\frac{m^2 v^3}{2(k_B T)^2} e^{-\frac{1}{2}\frac{mv^2}{k_B T}} \right) \tag{5.17}$$

The mean and the standard deviation of the effusive distribution respective are:

$$\bar{v} \quad = \quad \sqrt{\frac{9\pi k_B T}{8m}} \tag{5.18}$$

$$\sigma_v \quad = \quad \sqrt{\frac{0.466 k_B T}{m}} \tag{5.19}$$

Thus, for the oven temperature of 430 K, the average atomic beam velocity is $\sim$

380 m-s^{-1}, with a standard deviation of 138 m-s^{-1}. The effusive velocity distributions for three different velocities and their averages are illustrated in Figure 5.7.

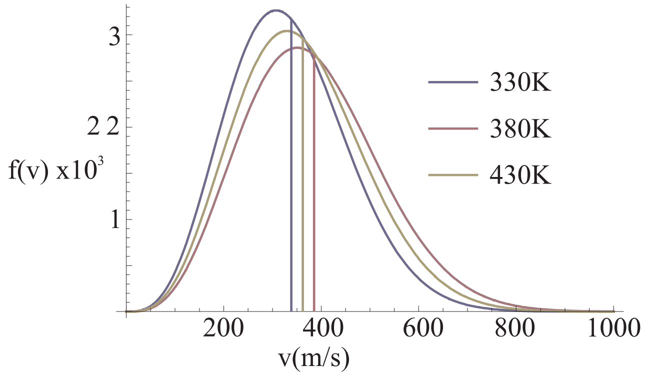

Figure 5.7: Effusive velocity distributions. The effusive velocity distributions for three different velocities is illustrated. The vertical lines correspond to the average velocities of the corresponding distributions.

Two different diode lasers are used to provide the slower beam and the repumper beam. The lasers are referenced to atomic spectra of ^{87}Rb and frequency stabilized using PI feedback circuits. The slower beam is locked to the red side of the F=2→F'=2 and F=2→F'=3 crossover and is detuned from the F=2→F'=3 transition by ∼145 MHz. The repumper laser is locked to the peak of the F=1→F'=2 and F=1→F'=1 crossover using a lock-in amplifier. The slower laser light and the repumper laser light are orthogonally polarized and coupled into the same polarization-maintaining single-mode fiber. The output of the fiber is circularly polarized using a quarter-wave plate and focused on the oven nozzle using an 8 cm focal length achromatic lens. The probe is derived from an independent laser and scans over the entire F=2→F' spectrum of ^{87}Rb.

5.4.2 Slowed atomic beam characterization

Absorption of the probe beam propagating through the slowed atomic beam at an angle of 68° is used to determine the flux and the velocity of the slowed beam. The intensity of the probe beam I_0 is maintained below the saturation intensity of the atomic transition, i.e. for ^{87}Rb, $I_0 <(I_{sat}=1.6$ mW-cm^{-2}). The transmitted intensity is then given by:

$$I_t = I_0 e^{-\frac{\Gamma_{scat}\hbar\omega_a}{2I_{sat}}} N_a \tag{5.20}$$

where N_a is the atomic area density. Thus, substituting the numbers for ^{87}Rb, the flux can be calculated as:

$$\Phi_a = N_a \bar{v} A_{beam} = \left(-3.3 \times 10^8\ cm^{-2}\right) ln\left(\frac{I}{I_0}\right) \bar{v} A_{beam} \tag{5.21}$$

Here, $\bar{v}$ is the average velocity of the atomic beam and A_{beam} is the cross-section area of the probe beam. The probe beam used in this case had an area of 3 mm^2 and power 30 μW, giving an intensity of 1 mW-cm^{-2}, which is less than 1 I_{sat}. The average velocity can be inferred from the Doppler shift the absorption signal suffers with respect to resonance due to the relative motion of the atomic beam and the probe beam. Given the difference between the frequency at which the maximum probe absorption through the slowed atomic beam occurs and the atomic resonance frequency obtained from Doppler-free saturated absorption spectroscopy $\Delta\nu$, the average atomic beam velocity can be calculated as:

$$\bar{v} = \frac{\lambda\Delta\nu}{\cos\theta} \tag{5.22}$$

Here, $\theta = 68°$ is the angle between the atomic beam and the probe beam wave-vector.

The maximum flux obtained for the Zeeman slower was 3×10^{11} atoms-s^{-1} for a velocity of 40 m-s^{-1}. Figure 5.8 shows the dependence of the absorption profile on extraction coil magnetic field. As can be inferred from the Equation 5.5, the output velocity of the Zeeman slower varies linearly with the magnetic field. However, as the extraction field changes, the effective magnetic field deviates significantly from the ideal magnetic field, leading to deviation from a linear change in output velocity with

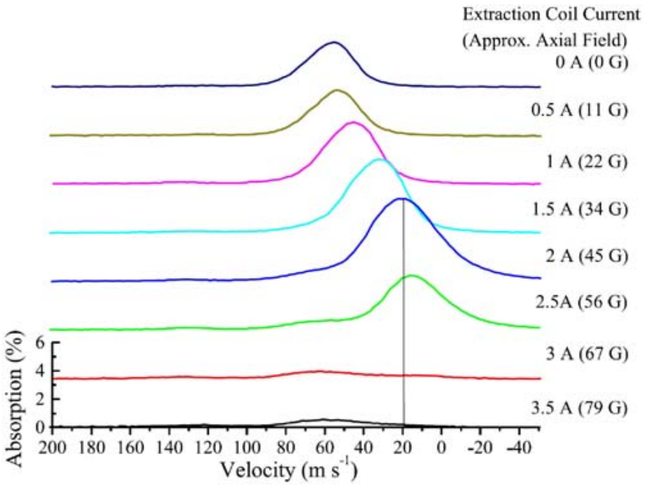

Figure 5.8: Absorption profile as a function of extraction field. The absorption profiles are plotted as a function of the extraction magnetic field. As the extraction magnetic field is increased, the velocity of the slowed atoms drops.

respect to the extraction magnetic field. For values of the extraction magnetic field higher than the ideal, the atoms are exactly in resonance with the slowing laser beam at some location inside the slower and are pushed back into the slower. Secondly, for even higher extraction field, the condition imposed on the magnetic field gradient by Equation 5.13 is also violated. Hence the absorption due to the slowed atoms vanishes.

The output velocity of the atoms can also be tuned using the frequency of the slowing laser, as can be seen from Equation 5.7. This is illustrated in Figure 5.9. As the slower laser frequency ω_l is increased, the laser detuning δ decreases, thus decreasing the final velocity. However, beyond a certain δ, the atoms start getting pushed back into the slower and the flux abruptly drops.

5.5 Conclusion and future improvements

A Zeeman slower was built and characterized as the primary source to the next generation of the atomic guide. As expected, we did find the output flux of the Zeeman slower to be a factor of 100 more than the PMOT flux. However, one

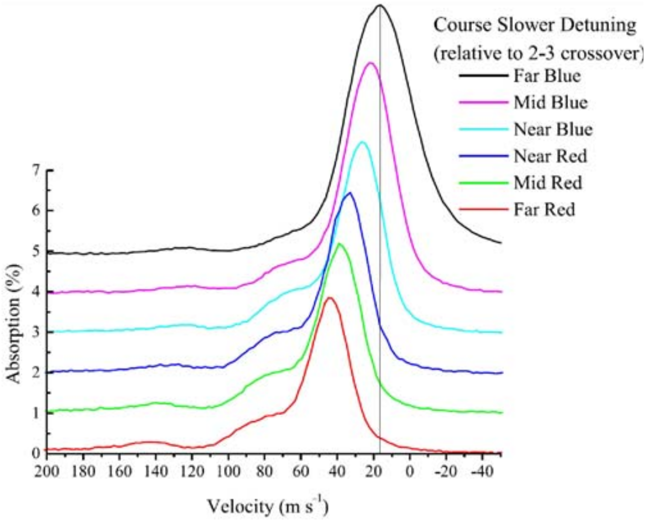

Figure 5.9: Absorption profile as a function of Slowing laser detuning.

inefficiency of the Zeeman slower stems from the fact that the atomic beam input to the slower has a finite transverse temperature. This causes ballistic expansion of the atomic beam as it propagates through the Zeeman slower. As the beam is decelerated, the ballistic expansion causes significant transverse spread of the atomic beam. In addition to this, photon scattering events give atoms random momentum kicks in the transverse direction leading to a random walk in the transverse velocity space and diffusion both in co-ordinate and velocity space. These factors combined lead to a decrease in the phase space density of the output atomic beam.

Focusing the slower laser beam on the oven nozzle alleviates this problem. However, to significantly reduce this effect, an input atomic beam collimation scheme using optical molasses [8], as invented by Slowe, *et al* [39], can be used. Even using a simple transverse optical molasses cooling on the atomic beam at the beginning of the slower can be helpful. However, the magnetic fields have to reduced significantly in the region of molasses cooling. This can be achieved by magnetically shielding the Zeeman slower coils using soft iron or μ-metal shields.

The range of the output atomic beam, i.e. how far from the slower output the atomic beam remains usable, can be enhanced by using the same transverse optical molasses cooling on the output side of the Zeeman slower. We did find that at a distance of $\sim$25 cm from the Zeeman slower output, the atomic flux was enhanced by a factor of 3 as opposed to without the transverse molasses cooling at the output.

Thus, there is a lot of scope for improvement in the Zeeman slower performance in the future, and I believe that it certainly would be possible to increase the atomic flux by an order of magnitude.

CHAPTER VI

Guiding Atoms in Rydberg State

The long, high gradient magnetic guide presents a unique system of quasi-one-dimensional gas of atoms with a high density of $\sim 10^9$ atoms-s^{-1}. This system can be utilized to study the dynamics of highly excited atoms, called Rydberg atoms, in a very steep two-dimensional trap. The study of Rydberg atoms is a very rich field in atomic physics owing to the extreme properties the Rydberg atoms have compared to atoms in ground state, such as very high dipole polarizabilities, magnetic moments and atom-atom interaction strengths. Due to these properties, the Rydberg atoms are very sensitive to electric and magnetic fields. Many diverse and interesting phenomena have been predicted and indeed observed in systems of interacting Rydberg gases due to these properties. The electron in the excited state is weakly bound to the ionic core, giving rise to a hygrogen-like atomic system, which can be described using simple physics of a hydrogen atom. The wave-numbers of the transitions to highly excited Rydberg states are given by the following formula:

$$\begin{aligned} \nu_{ryd} &= \nu_{\text{inf}} - \frac{Ry}{n^{*2}} \\ &= \nu_{\text{inf}} - \frac{Ry}{(n-\delta_l)^2} \end{aligned} \tag{6.1}$$

where ν_{inf} is the ionization wave-number, $n^* = n - \delta_l$ is the effective principal quantum number of the excited Rydberg state, n is the principal quantum number of the hydrogenic excited state, δ_l is the quantum defect, which depends on the angular momentum l of the excited state and Ry is the Rydberg constant. The quantum defect includes the effect of the interaction of the outer electron with the ionic core. The transition energy between two states can be calculated using the Bohr formula:

$$W_2 - W_1 = \frac{Z^2 e^4 m_e}{(4\pi\epsilon_0)^2 \, 2\hbar^2} \left(\frac{1}{n_1^{*2}} - \frac{1}{n_2^{*2}} \right) \tag{6.2}$$

Thus we find that the Rydberg constant is simply $Ry = \frac{Z^2 e^4 m_e}{(4\pi\epsilon_0)^2 2\hbar^2 c}$.

For an atom excited to a Rydberg state with principal quantum number n, the possible values of the angular quantum number are $l = 0 \ldots (n-1)$. The magnetic quantum number in this case can take on any value $|m| = 0 \ldots l$, with a maximum value $m = n - 1$ for the manifold $|n, n-1\rangle$. From analysis in Chapter V, we see that the magnetic moment of an atom in this state is $\mu = m\mu_B$, where μ_B is the Bohr magneton. Hence, if a ^{87}Rb atom is excited to a state $n = 51$, the atom can have a maximum magnetic moment of $\mu^{max} = 50\mu_B$, which is a factor of 50 higher than the magnetic moment of an atom in the $\left|{}^5\mathrm{S}_{1/2}, \mathrm{F} = 2, \mathrm{m_F} = 2\right\rangle$ ground state. This would lead to a 50 times stronger confinement for the Rydberg atom in a quadrupole magnetic field, as compared to an atom in the ground state. We can use this fact to magnetically guide Rydberg atoms in a 2D quadrupole guiding field generated as described in Chapter II. The behavior of Rydberg atoms in 2D quadrupole magnetic field have been studied extensively [40–42]. This experiment can be used to validate some of the findings in the above theoretical studies.

How to excite Rydberg atoms and populate these high-angular momentum states will be the subject of Section 6.1. The experimental setup and the Rydberg atom excitation scheme are described in Section 6.2. I give the details of the ion detection scheme, along with some simulation results of the ion detection in Section 6.3. The current state of the experimet and the next steps toward observing guided Rydberg atoms are detailed in Section 6.4.

6.1 Guiding High-Angular Momentum states

We use a three-step excitation scheme to excite the ^{87}Rb atoms in the ground state to the Rydberg state. The atoms are initially in the $\left|5S_{1/2}, F = 1, m_F = -1\right\rangle$ magnetically guided dark state. They are optically pumped into the bright state manifold $\left|5S_{1/2}, F = 2\right\rangle$ using the repumper laser tuned to the $\left|5S_{1/2}, F = 1\right\rangle \rightarrow \left|5P_{3/2}, F = 2\right\rangle$ transition. A probe laser pulse tuned to the $\left|5S_{1/2}, F = 2\right\rangle \rightarrow \left|5P_{3/2}, F = 3\right\rangle$ cycling transition is simultaneously incident on the atoms in the excitation region. The intensity of the laser pulse is very high, such that the transition is saturated. In this case, the atoms spend half the time in the excited state manifold $\left|5P_{3/2}, F = 3\right\rangle$. A blue Rydberg excitation beam tuned to the $\left|5P_{3/2}, F = 2\right\rangle \rightarrow \left|nD_{5/2}\right\rangle$ then excites the atoms to the $\left|nD_{5/2}\right\rangle$ Rydberg state. The magnetic moment of the atoms in the $\left|nD_{5/2}\right\rangle$ Rydberg state is not very high, and because the magnetic field direction in the guide varies over the excitation region, it is not possible to excite a particular m-state. Hence, we end up with a distribution of m-quantum numbers in the Rydberg atoms, only a few of which are low-field seeking and hence can be guided.

There exists a mechanism called l-mixing, which populates the high-angular momentum states [43]. These high-l states have many advantages over the optically excited low-l Rydberg states. Due to the high angular momentum, these states can have very high magnetic moments. An ensemble of Rydberg atoms in high-l states will be in a statistical mixture of m-states. However, the average m-quantum number of the atoms in the ensemble is still significantly higher than that of the initial optically excited state. Consequently, the atoms are confined more tightly toward the guiding center. Secondly, the high-l states can radiative decay only to states allowed by the angular momentum selection rules: $\Delta l = \pm 1$. Thus, the lowest n-state an atom in a high-l state can decay to is $n' = l$, which is energetically very close to the original n-state and thus has very low transition frequency $\omega_{nl,n'l'}$ in the microwave regime. The Einstein A-coefficient, which gives the probability of radiative decay, is proportional to $\omega^3_{nl,n'l'}$, as well as the square of the spatial overlap of the radial wave-functions [44], i.e. the dipole matrix element. For optical transitions, the lifetime of the excited states is proportional to n^3. Circular states with angular momentum $l = n - 1$, however, can only decay to $n - 1, l - 2$ state. The frequency of this transition goes as $1/n^3$, thus contributing a factor of $1/n^9$ to the Einstein A-coefficient. The radial matrix element is proportional to n^2, contributing to a factor of n^4. Combining these two effects, the transition probability for the decay of a circular state, and hence the lifetime goes as $1/n^5$. For an ensemble of Rydberg atoms in a statistical distribution of l-states, the average excited state lifetime is then proportional to $1/n^{4.5}$. The average excited state lifetimes for these ensembles is in the range of milliseconds. Thus, the atoms in the high-angular momentum states are prime candidates for magnetic trapping and guiding, owing to their long lifetimes and high magnetic moments. These high-l states also have higher ionization potential, $1/4n^4$ as compared to low-l states which have an ionization potential of $1/16n^4$, in atomic units.

These high-l states are populated primarily through electron-Rydberg atom collisions, though Rydberg-Rydberg collisions also contribute [45]. If the density of excited Rydberg atoms is high ($> 10^8$ atoms-cm^{-3}), some of the Rydberg atoms auto-ionize due to Rydberg-Rydberg collisions, generating cold electrons. Most of the cold electrons leave the excitation region. This creates a positive space charge due to the remaining ions, and the remaining electrons are trapped in by the space charge effect. These electrons then collide with the Rydberg atoms which did not ionize to populate the high-l states.

A energy of Rydberg atom in presence of an electric field is shifted due to the Stark effect. For high values of electric field in the range of hundreds of V/cm, the Rydberg state mixes with the nearby hydrogenic manifold as shown in Figure 6.1. If the electric field is turned on and off diabatically, the atom ends up in a superposition of states, which is dominated by the states in the hydrogenic manifold. The redistribution of the states in the hydrogenic manifold is uniform and happens over a very short time-scale [46], leaving the atom in a high-l state. Such a situation occurs when an electron interacts with a Rydberg atom. In this case, the Coulomb field of the electron causes l-mixing to take place, thus generating a Rydberg atom in a high-l state.

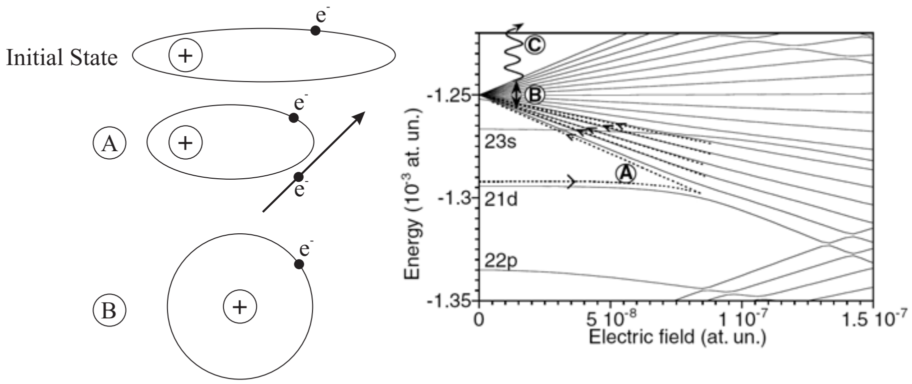

Figure 6.1: The process of l-mixing is illustrated in this figure. The initial state in the Stark map is 21D. As an electron collides with the atom, as shown in A, the initial state mixes with the hydrogenic manifold, and after the collision, the atom is left in a superposition of hydrogenic high-l states, as shown in B. These can then ionize via couling through the black-body radiation to the continuum, as shown in C.

6.2 Experimental Setup

The experimental setup for guiding the Rydberg atoms consists of an assembly of two electrodes as shown in Figure 6.2. The electrodes are precision machined out of

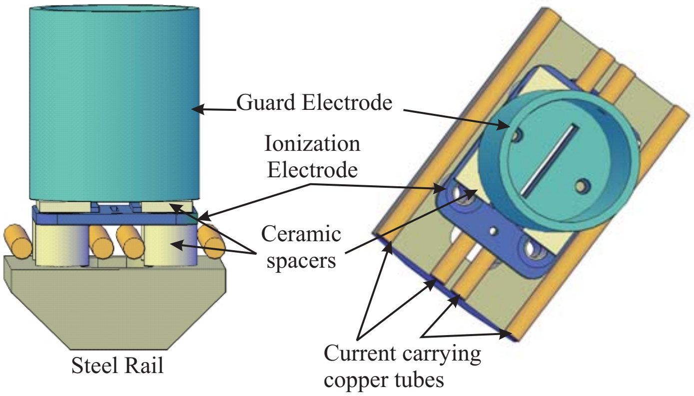

Figure 6.2: Electrodes for ionization of Rydberg atoms is shown in the figure. The ionization electrode is 3 mm above the surface of the wires. The guard electrode is 2 mm above the ionization electrode. The ionization electrode is at ground potential during excitation phase and at -1.4 kV during the ionization and extraction phase. The guard electrode is always maintained at -1.4kV and protects the multi-channel plate (MCP) above it from the electric field of the ionization electrode. The ions are extracted by a large electric field generated by the ionization electrode in the region of the guided atomic beam, are pass through the slits in the electrodes to be detected on the MCP above.

brass such that the ion extraction slits line up exactly. The ionization electrode (IE) is mounted on the steel rail 3 mm above the guide tubes, on four Macor stand-offs and centered on the threaded holes in the steel rail by using counter-sunk screws. The IE has a slit of dimensions 1 mm×10 mm along the length, which is aligned with the guide axis. The guard electrode (GE) is a brass cup with diameter 1 inch and 1 mm wall thickness. The GE also has a slit in the bottom of dimensions 2 mm×10 mm, which is co-aligned with the slit in the IE. The electrodes are positioned such that the slit is centered on an optical viewport in the guide and situated above an optical access aperture in the guide-supporting steel rail. The the ion detector is a custom-ordered dual multi-channel plate (MCP) detector (Beam Imaging Solutions BOS-18) with 5 mini high-voltage (MHV) feedthrough connectors. A multi-channel plate (MCP) is mounted on top of the GE, such that the shield of the MCP is concentric with the GE. Four of the MCP MHV connectors are used internally for the front, middle, back and phosphor screen electrodes. The spare connector is connected to the IE using a Macor tube insulated steel wire. The GE is electrically shorted with the MCP shield and front electrode so as to maintain zero electric field in the vicinity of the MCP front plate.

6.3 Rydberg Excitation and Ion Imaging

As described in Section 6.1, the excitation of the atoms in the magnetic guide proceeds in three simultaneous steps, and lasts for 10 μs. The first step is optical pumping from the magnetically guided dark state $\left|5S_{1/2}, F=1, m_F=-1\right\rangle$ to the bright state manifold $\left|5S_{1/2}, F=2\right\rangle$ using the repumper laser tuned to the $\left|5S_{1/2}, F=1\right\rangle \rightarrow \left|5P_{3/2}, F=2\right\rangle$ transition. A probe laser is simultaneously incident in the excitation region and tuned to the $\left|5S_{1/2}, F=3\right\rangle \rightarrow \left|5P_{3/2}, F=3\right\rangle$ cycling transition. The probe laser has high intensity $\sim$ 100 $\mathrm{I_{sat}}$ where I_{sat} is the saturation intensity, such that the cycling transition is saturated and an atom spends half the time in the excited state. A blue Rydberg excitation beam tuned to the $\left|5P_{3/2}, F=2\right\rangle \rightarrow \left|nD_{5/2}\right\rangle$ then excites these atoms to the $\left|nD_{5/2}\right\rangle$ Rydberg state, where n is the principal quantum number of the excited Rydberg state. The oscillator strength of the transition to the Rydberg state is very low [47], giving rise to low absorption cross-section for transition to a bound excited state, and is given by:

$$\sigma_R = \frac{\sigma_{PI}}{n^3 \Delta\omega} \tag{6.3}$$

Here, $\sigma_{PI} = 1.2 \times 10^{-17}$ cm^2 is the photoionization cross-section of ^{87}Rb from the $\left|5P_{3/2}, F=2\right\rangle$ state. This equation assumes that the laser linewidth $\Delta\omega > 1/n^3$ in atomic units, such that the neighboring states cannot be resolved [45]. For excitation into $n = 53$ state, with a laser line-width of 1 MHz, we get the absorption cross-section of $\sigma_R = 5.3 \times 10^{-15}$ cm^2. Using 5 mW of power in the blue excitation pulse of duration 10 μs and focusing the beam to a spot-size of 100 μm, we get

$\sim 10^{15}$ photons-cm^{-2} per pulse. From this, we can estimate that the transition to the Rydberg state would be saturated! Given the atomic beam velocity of 1 m-s^{-1} and a flux of $\sim 10^7$ atoms-s^{-1}, there are are 1000 atoms in the excitation volume in the guide of length 100 μm. Assuming that the red transition is saturated, we can excite a maximum of 500 Rydberg atoms in the guide. However, due to various inefficiencies in the laser polarizations and intensities, we can realistically expect about 100 Rydberg atoms per excitation. The IE is on ground during the excitation period.

The electric field during the excitation period it shown in Figure 6.3. From this figure, we can see that the electric field in the excitation region is less that 0.2V-cm^{-1}. Rydberg atoms can easily exist in such a low electric field. The IE is switched to -1.4kV after a variable time delay to ionize the Rydberg atoms and accelerate the ions toward the MCP. The electric field at the location of the guide axis during this extraction period can be as high as 1 kV-cm^{-1}, as shown in Figure 6.4. This

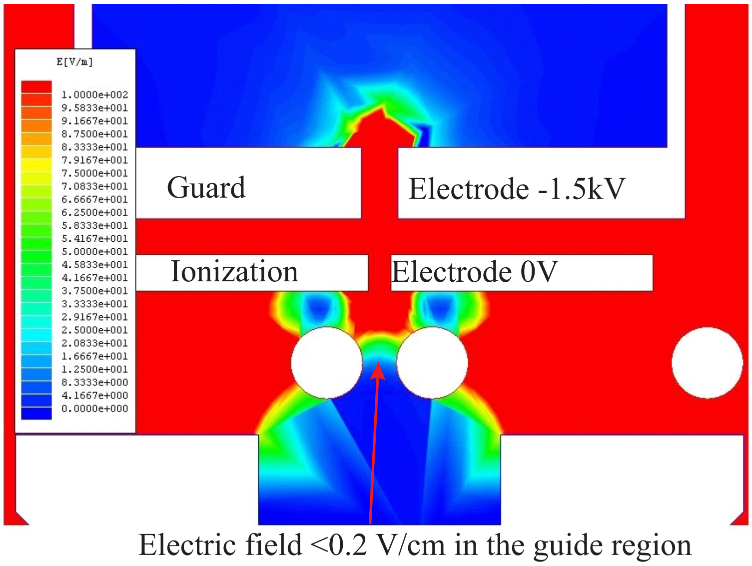

Figure 6.3: Electric field in the guiding mode is shown in this figure. The ionization electrode is at 0 V and shields the guide region from the electric potential of the guard electrode. The electric field in the guide region is less than 0.2V-cm^{-1}.

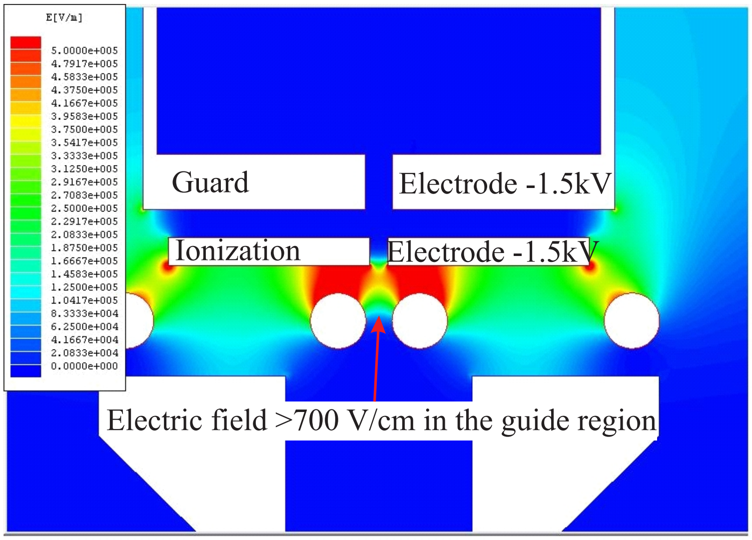

Figure 6.4: Electric field in the ionization/extraction mode is shown in this figure. The ionization electrode is at -1.5 kV and produces an electric field of 700 v-cm^{-1} in the guide region. This field is high enough to ionize the Rydberg atoms and accelerate the ions toward the MCP.

electric field is high enough to ionize Rydberg atoms in high-l states, which ionize at an electric field value of a few hundred V-cm^{-1}. The ions are accelerated upwards due to the electric field and acquire a significant kinetic energy of nearly a keV as they enter the field-free region in the guard electrode. The ions then follow ballistic trajectories in the volume of the guard electrode and impinge upon the MCP. The MCP amplifies the ion current by producing an electron avalanche per ion hit, which then produces phosphorescence on a phosphor screen. The image of the phosphor screen is obtained by a camera triggered simultaneously with the turn on of the ionization electric field. We have simulated the ion detection process using the exact electric and magnetic fields calculated for the geometry shown in the Figure 6.2. The results are shown in Figure 6.5. Trajectories of 100 ions are simulated and include the ion-ion Coulomb interactions. The initial longitudinal distribution of atoms is consistent with excitation due to a Gaussian laser beam focus. The transverse distribution is derived from the temperature of that atoms in the guide, as measured

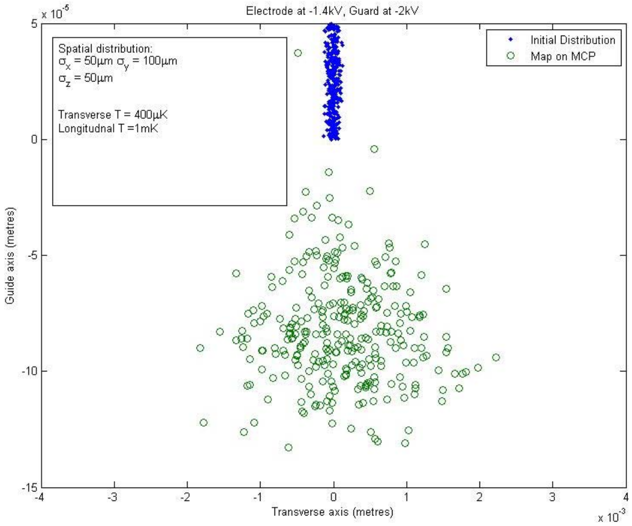

Figure 6.5: Simulation of ion imaging in the guide. The blue dots represent the starting positions of the ions in the guide. The green circles represent the location of the ions when they reach the MCP. We see that the ion imaging scheme has a magnification ration of $\sim$ 14. Image courtesy Varun Vaidya.

in II. The magnification factor of the ion imaging scheme is approximately 14. Thus ion distribution of width 0.2 mm in the guide are mapped on to a line which is 3 mm long, transverse to the guide. Also seen in the simulation is the effect of the motion of ions through a transverse magnetic field, which imparts a velocity to the ions in the direction opposite to that of the atomic flow.

6.4 Current Status

We have successfully excited plasma in the atomic guide by photo-ionization. The excitation pulses were 20 μs long and the repetition period was 1 ms. The wavelength of the blue laser was set above photoionization threshold. The ionization electrode was on in steady state and as not switched. The ions created by the photoionization were successfully detected on the MCP. A representative image of the detected ions on the phosphor screen of the MCP is shown in Figure 6.6, along with the atomic beam image. It is seen that the ions that are detected on the MCP form a discrete

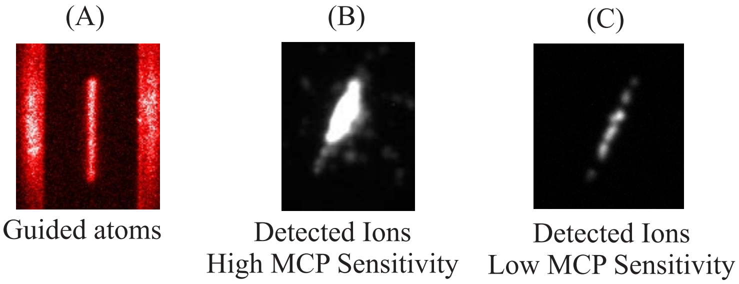

Figure 6.6: Image of detected ions on the phosphor screen. The panel (A) shows a fluorescence image of the guided atomic beam at the end of the magnetic guide. The panel (B) shows the image of the ions on the MCP phosphor screen with the sensitivity of the MCP at maximum. The panel (C) shows the image of the ions with the sensitivity of the MCP at minimum, where the image phosphorescence is still visible. Note the discrete structure of the image. The line of ions is transverse to the guide axis.

bead-like structure. The behavior of this structure as a function of the frequency and the intensity of the excitation laser needs to be studied to understand what it is caused by. We have put in place an electronic circuit to zero the electric fields in the excitation region so that the electrons produced due to auto-ionization can cause l-mixing in the Rydberg gas. This progress is happening as I write, and soon we should be able to observe guided Rydberg atoms.

CHAPTER VII

Next Steps Toward an Atom Laser

The atom guide could be a useful tool for many experiments. It provides a quasi-one-dimensional gas of atoms on a macroscopic scale. It also provides a large interaction length for a laser beam propagating along its axis, thus enhancing tiny non-linear effects in atom-light interaction. As we have seen in Chapter II, a filtered guided atomic beam can also be used to construct interferometers, such as those that use light from a mercury arc lamp. However, to utilize the atom guide to pump an Atom Laser, a number of challenges still have to be resolved. First and foremost, the guide throughput is currently too low at 3×10^7atoms-s^{-1} to achieve a hydrodynamic atomic flow. Simulations show that a throughput of 3×10^9atoms-s^{-1} would be able to sustain high enough collision rate of 500 collisions per atom through the length of the guide. Such high collision rate is necessary for the atomic beam to rethermalize in presence of forced evaporative cooling, and to maintain a negative temperature gradient along the guide. Simulations show that an input atomic beam with a temperature of 100 μK and a flux of 3×10^9atoms-s^{-1} should reach quantum degeneracy when evaporatively cooled. Currently, the atomic beam from the pyramidal MOT has a flux of 3×10^9atoms-s^{-1}. As the efficiency of transfer from the PMOT to the atomic guide cannot be 100%, we need to use another source of a cold atomic beam instead of the PMOT. The Zeeman slower, which is already implemented and tested, takes on the role of such a source. However, the inefficiencies in the transfer scheme using the 2D+ MOT are very high. We believe that due to the secondary emission of repumper stray light into the guide, many of the otherwise guided atoms are optically pumped out of the guided dark state into a possibly unguided bright state, where they scatter the MOT light. This leads to very high trap losses from the guide and these losses increase as the number of atoms in the 2D+ MOT increases. Hence, the Zeeman slower will have to be supplemented with an efficient transfer scheme for it to be effective. In addition to this, the vertical rise section increases the velocity spread of the guided atoms, and magnetic reflections in the compression region also limit the guide flux. To counter the gravitational and magnetic retardation, the atoms have to be launched with a significant kinetic energy. However, if the objective is to pump a stationary BEC, all the kinetic energy has to be dissipated through evaporative cooling, which is not possible in a guide of reasonable length. Thus, to maximize the transfer of atoms from the Zeeman-slowed beam to the guide, a new transfer scheme has to be designed.

7.1 Atom Injection

One such possible scheme for injecting atoms into the guide, shown in Figure 7.1, involves collecting atoms from the Zeeman slower and cooling them using a 3D MOT. The 3D MOT is constructed in the mirror MOT configuration, with the shutter baffle acting as the mirror surface, as described in the caption of Figure 7.1. The MOT coils are energized in the anti-Helmholtz configuration, such that the MOT coil closest to the guide generates magnetic field in the same direction as the guide bias magnetic field. A horizontal bias magnetic field is generated by the bias coils which lifts the

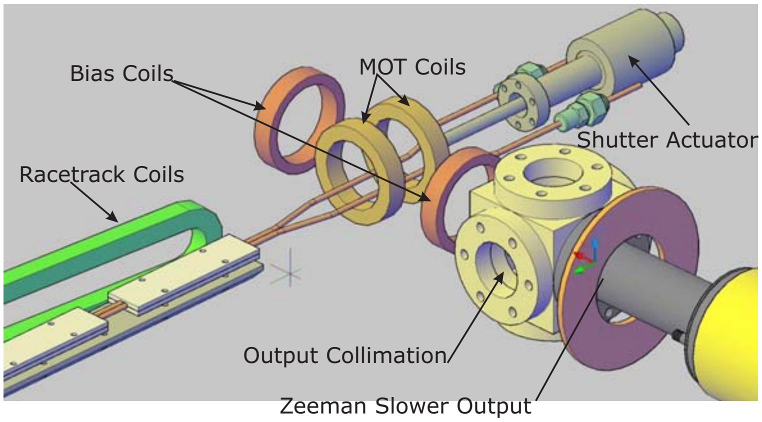

Figure 7.1: Proposed scheme to transfer atoms from the Zeeman slower to the guide. The optically collimated slow atomic beam from the Zeeman slower is captured by a 3D MOT. A baffle with a stuttered aperture is constructed above the guide wires directly below the MOT and is not shown for clarity. The shutter is closed during the collection period. The laser beams are then turned off and the shutter is opened. The atoms are transferred into the guide by appropriately manipulating the magnetic fields as described in the text.

guiding center to the MOT plane ∼1.5 cm above the plane of the wires. The magnetic field topology thus becomes that of a 3D MOT. Laser beams are incident upon the MOT region along the principle MOT axes during the collection phase which lasts for ∼200 ms. After the the collection phase, the MOT lights are turned off and the polarity of the MOT coil further away from the guide is reversed, so as to provide a longitudinal bias field. This converts the magnetic field topology into an Ioffe-Pritchard type trap geometry. An optical beam above and along the guide axis then optically pumps the atoms into the trapped state, which for ^{87}Rb is $|\mathrm{F}=2,\mathrm{m_F}=2\rangle$. The stutter is then opened and the bias coils are ramped down. This lowers the trap center into the guide axis. The MOT coil closest to the guide is then de-energized, injecting the atoms into the guide. After the injection phase, which lasts for ∼100 ms, the MOT coils ramped up in the anti-Helmholtz configuration and the cycle repeats again. There are two advantages of this scheme. Firstly, the shutter is closed and the guide is optically isolated from the MOT when the laser beams are on, thus eliminating the stray light to a large extent. Secondly, the atoms are always trapped from the collection phase through to the injection phase, thus minimizing trap losses due to ballistic injection. However, since the injection is pulsed, the repetition rate of the pulses has to be high to maintain a high atomic flux in the guide.

7.2 Surface Evaporative Cooling

Once the atomic flux is established in the guide, the atomic beam can be evaporatively cooled to lower its temperature. The usual method of evaporatively cooling atoms in a magnetic trap involves applying radio frequency electromagnetic field with frequency decreasing in time. It is, however, not possible to implement such a scheme in space and an alternative needs to be developed. Such an alternative was developed by Harber *et al* [48] at University of Colorado, using the adsorption of atoms on a dielectric surface to implement forced evaporative cooling. The Figure 7.4 is adapted from [48] and shows a thermal cloud being progressively brought closer to a silicon surface and shadow imaged. The last panel clearly shown the formation of a BEC, and the authors are of the opinion that this scheme is as efficient as the RF evaporation scheme described earlier. This scheme is very well

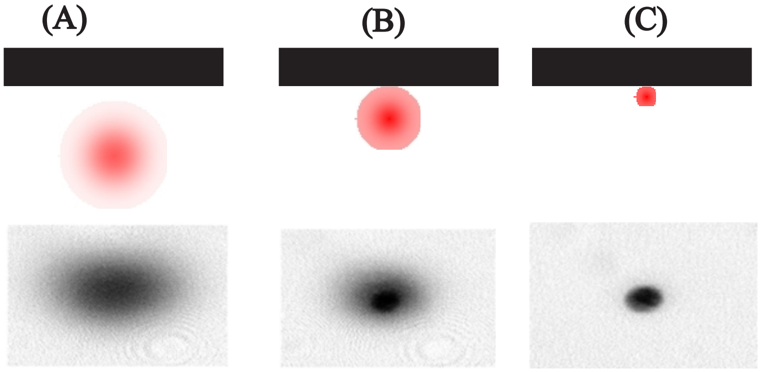

Figure 7.2: Surface adsorption forced evaporative cooling in a 3D trap. This figure is adapted from [48] and shows the implementation of surface adsorption forced evaporative cooling in a 3D trap. Panel (A) shows the thermal cloud in a magnetic trap. Panel (B) shows the partial onset of the quantum phase transition when the atom cloud is brought close to the surface. Panel (C) shows an almost pure condensate when the thermal cloud is brought to within 10 μm of the dielectric surface.

suited to be adapted to evaporatively cool a guided atomic beam, as shown in the schematic in Figure 7.3. By applying a high horizontal bias field at the entrance of the magnetic guide, and slowly reducing this bias field, the guiding center can be initially displaced above the plane of the wires and slowly lowered. By appropriately placing dielectric surfaces near the plane of the wires as shown in Figure 7.2, the atomic beam can be evaporatively cooled. The horizontal bias field can be applied externally, outside the vacuum, and can be dynamically configured to provide an optimal spatial evaporation ramp profile.

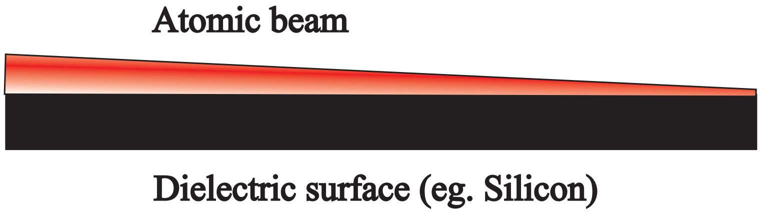

Figure 7.3: Surface adsorption forced evaporative cooling adapted for a guide geometry. This figure shows schematically how the surface adsorption forced evaporative cooling can be adapted to the guide geometry. The guiding center can be displaced closed to the dielectric surface using external bias magnetic fields.

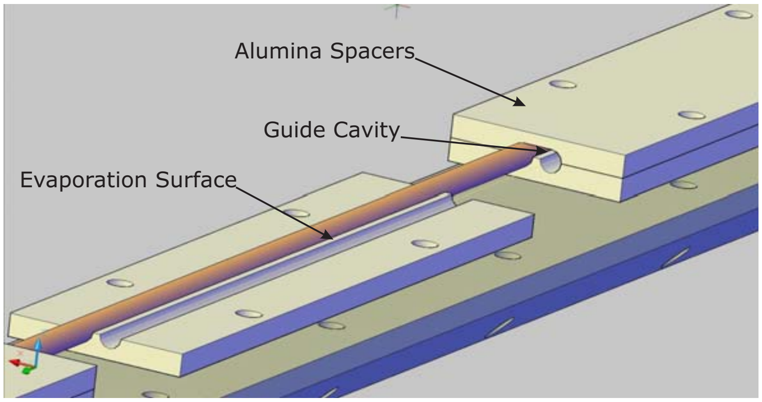

Figure 7.4: Implementation of surface adsorption forced evaporative cooling adapted for a guide geometry. This figure shows a rendering of the implementation of the surface adsorption evaporative cooling for the guide geometry. The alumina spacers, which support the guide-generating copper tubes, can themselves be used as the dielectric surface for evaporative cooling.

7.3 Output Coupling

The strategy we have chosen to implement an atom laser is to first generate a BEC, and then out-couple the BEC continuously as an atom laser, while simultaneously pumping it with cold atoms to achieve steady state. The transverse confinement for the BEC is provided by the magnetic guide fields. The longitudinal confinement is provided by slightly modulating the guide longitudinal bias field to form a shallow dimple in the potential landscape. A light-shift barrier is used on the output side of the trap, as shown in Figure 7.5.

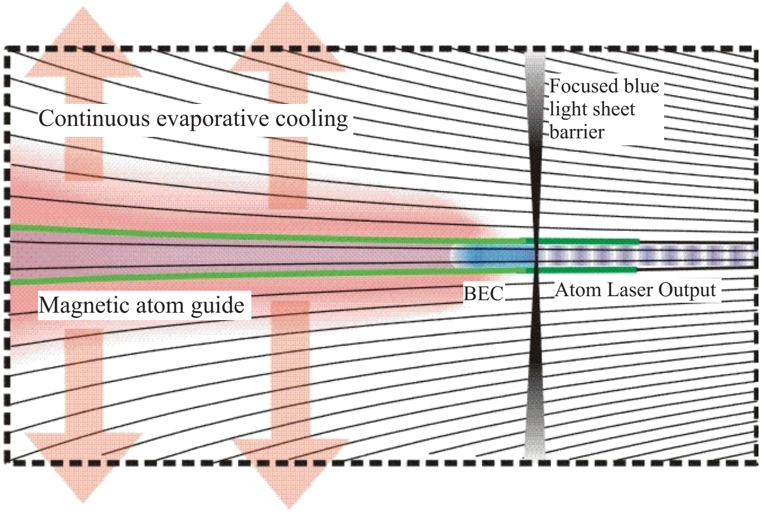

Figure 7.5: Atom laser output coupler. This figure shows the conceptual schematic of the output coupling scheme to out-couple the atom laser from a stationary BEC. The BEC is formed in a dimple produced by slightly modulating the guide longitudinal bias field. It is continuously replenished by the evaporatively cooled, guided atomic beam. A light-shift barrier confines the BEC on the output side, as shown. An atom laser output is generated by coherent tunneling of the BEC through the light-shift barrier.

The light-shift barrier is a sheet of light far blue-detuned from an atomic transition. When atoms encounter this sheet of light they experience a positive AC Stark shift [8]. The energy shift due to the AC Stark effect is given by:

$$\Delta E = \frac{e^2 E_0^2 \left|\langle e|r|g\rangle\right|^2}{2\hbar\delta_l} \tag{7.1}$$

Here, e is the electronic charge, δ_l is the detuning of the laser from the $|e\rangle \rightarrow |g\rangle$

transition, $\langle e|r|g\rangle$ is the corresponding dipole matrix element and E_0 is the laser electric field amplitude, which is related to the laser intensity I by the following formula:

$$I = \frac{1}{2}c\epsilon_0 E_0^2 \tag{7.2}$$

Thus, from Equation 7.1, the energy shift is seen to be positive for positive δ_l, leading to a repulsive potential barrier. The probability of coherent tunneling of the BEC through this barrier is non-zero and is dependent on the height and the length of the barrier. This gives a mechanism to control the tunneling rate of the BEC through the barrier. The tunneled portion of the BEC is the atom laser output. A steady state is reached when the tunneling rate equals the rate of stimulated collisions into the trap ground state, or the BEC. The tunneling rate can be varied by changing the intensity of the light-shift barrier laser. In steady state, a continuous guided atom laser beam can be generated.

7.4 Spiral Guide

However, for a BEC to form at the end of the guide and to be continuously replenished in a phase-coherent manner, the guided atomic beam need to occupy only the first few quantum states of the magnetic guiding potential. Any imperfections in the guiding potential, such as randomly varying magnetic field gradient or gravitational potential due to random variations in the height of the atomic guide, would lead to parametric heating of the guided atomic beam. We have estimated that to keep the parametric heating rate down, the variation in the height of the guiding potential has to be less than 100 μm. This requirement is very stringent and imposes a very strict constraint over the fabrication of the guide. Due to this, it is nearly impossible to construct a magnetic guide which is long, so as to allow efficient evaporative cooling to take place. The evaporative cooling cycle for 3D BECs usually requires 30 s for it be efficient in common geometries. In the guide geometry, for an atomic beam with a modest average velocity of 20 cm-s^{-1}, to allow for such a long evaporative cooling time would require a 6 m long guide. Keeping the variations in the height of the guide along the entire 6 m of its length would be a prohibitively expensive fabrication challenge and hence an alternative approach is needed.

Such an alternative is winding up the guide in a spiral geometry, as shown in Figure 7.6. Such a guide could be fabricated using micro-machining techniques and would be very easy to integrate into any applications and devices. Figure 7.6 shows the magnetic field due to two parallel wires of cross-section 0.5 mm×0.5 mm and wound as a spiral, carrying parallel current of 10 A. Fabrication of such a spiral guide of length 3 m can be achieved by having 10 turns in a spiral of diameter 10 cm, with a pitch of 0.5 cm.

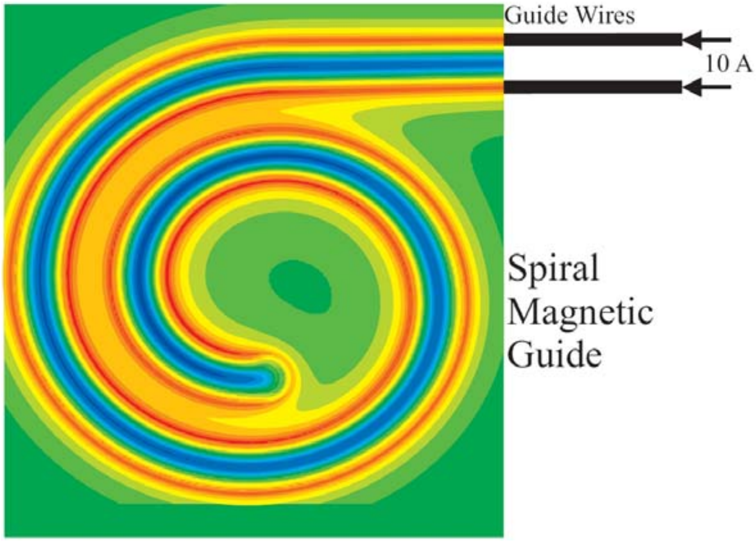

Figure 7.6: Spiral guide concept. The magnetic field due to two parallel wires of cross-section 0.5 mm×0.5 mm carrying parallel current of 10 A in a spiral configuration is shown. Blue color represents the magnetic field minimum, along which the atoms in a low-field seeking state that are injected into the guide will travel. This concept can be used to fabricate spiral guides with linear lengths of 3 m with 10 turns while keeping the diameter of the spiral as small as 10 cm.

The spiral geometry can also be implemented in a four-wire current topology, as shown in Figure 7.7. Such a four-wire guide using wires separated by 0.5 mm and

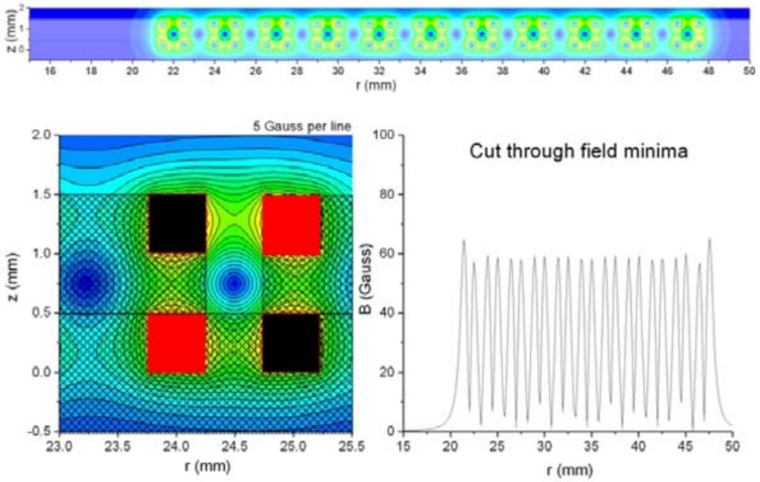

Figure 7.7: Radial cut through a four wire guide in spiral configuration. A radial cut of the four-wire guide is illustrated. The guide consists of four parallel wires of cross-section 0.5 mm×0.5 mm, carrying current of 10 A, and arranged in a spiral. For the geometry shown, the magnitude of the magnetic field is plotted versus the radial position in the spiral. Magnetic field gradient of as high as 1500 Gauss-cm^{-1} are obtained at the center of the guide.

having a cross-section of 0.5 mm×0.5 mm with a current of 10 A can generate a magnetic guiding potential with gradient as high as 1500 Gauss-cm^{-1}. This guide can be fabricated using micro-machined copper spirals held in place by alumina insulators. The atoms are injected on the outer entrance of the spiral and travel inwards. Because the velocity of the atoms is constantly changing, the longitudinal and the transverse components of the atomic velocity mix. This ensures that the longitudinal and transverse temperatures of the atomic beam are the same, and increases the efficiency of rethermalization upon forced evaporative cooling. The guiding channel can be displaced vertically by applying an external vertical bias field. This enables the use of surface-adsorption evaporative cooling in this geometry.

7.5 Outlook

The long-term goal of this project is to generate a continuous-wave, amplitude- and phase-stable coherent atomic beam extracted from a continuous Bose-Einstein condensate (cw-BEC), which will be the ideal atom source to operate interferometric devices. It has been proposed [9, 10, 49, 50] to produce quantum-degenerate atomic beams via forced evaporative cooling in long magnetic guides. The work presented in this paper lays important foundations for the realization of these ideas. Related work performed at ENS, Paris [12] has now recently resulted in the demonstration of evaporative cooling in a magnetic guide [11]. In this context, the next step in this project will be to demonstrate surface adsorption evaporative cooling in the horizontal section of the guide. The challenge will be to obtain collision rates high enough that the atom evaporation causes a strong increase in phase-space density of the atomic beam. Several modifications are planned to achieve this goal, as detailed in this chapter.

The project is poised to produce many great ideas and results. There are many directions one can take. The one I suggest is to test the surface adsorption evaporative cooling in the current linear guide setup. Even if the cooling mechanism does not work, it would be worthwhile to know that the idea of skimming away the most energetic atoms using a dielectric surface works! One more important step would be to interface the Zeeman slower with the guide. As having the largest atomic flux through the guide is the name of the game, trying and improvising different techniques to get the atoms from the Zeeman slower into the guide would have a significant pay-off, not to mention it would be a lot of fun! So, toward an Atom Laser we go....

BIBLIOGRAPHY

BIBLIOGRAPHY

[1] Stephan Wildermuth, Sebastian Hofferberth, Igor Lesanovsky, Elmar Haller, L. Mauritz Andersson, Sönke Groth, Israel Bar-Joseph, Peter Krüger, and Jörg Schmiedmayer. Microscopic magnetic-field imaging. *Nature*, 435:440, May 2005.

[2] J. M. McGuirk, G. T. Foster, J. B. Fixler, M. J. Snadden, and M. A. Kasevich. Sensitive absolute-gravity gradiometry using atom interferometry. *Phys. Rev. A*, 65:033608, February 2002.

[3] T. L. Gustavson, P. Bouyer, and M. A. Kasevich. Precision rotation measurements with an atom interferometer gyroscope. *Phys. Rev. Lett.*, 78(11):2046–2049, March 1997.

[4] J. Schmiedmayer, M. S. Chapman, C. R. Ekstorm, T. D. Hammond, S. Wehinger, and D. E. Pritchard. Index of refraction of various gases for sodium matter waves. *Phys. Rev. Lett.*, 74 (7):1043–1047, February 1995.

[5] Y. Shin, C. Spanner, G.-B. Jo, T. A. Pasquini, M. Saba, W. Ketterle, D. E. Pritchard, M. Vengalattore, and M. Prentiss. Interference of bose-einstein condensates on an atom chip. *preprint, arXiv:cond-mat/0506464 v2*, July 2005.

[6] Mark A. Kasevich. Coherence with atoms. *Science*, 298:1363, November 2002.

[7] G. Zabow, R. S. Conroy, and M. G. Prentiss. Coherent matter-wave manipulation in the diabatic limit. *Phys. Rev. Lett.*, 92(18):180404, May 2004.

[8] Harold J. Metcalf and Peter van der Straten. *Laser Cooling and Trapping.* Springer-Verlag New York, Inc., 1999.

[9] P. Cren, C. F. Roos, A. Aclan, J. Dalibard, and D. Guéry-Odelin. Loading of a cold atomic beam into a magnetic guide. *Euro. Phys. JD*, 20:107–116, July 2002.

[10] C. F. Roos, P. Cren, T. Lahaye, J. Dalibard, and D. Guéry-Odelin. Injection of a cold atomic beam into a magnetic guide. *Laser Physics*, 13(4):605, July 2003.

[11] T. Lahaye, Z. Wang, G. Reinaudi, S. P. Rath, J. Dalibard, and D. Guéry-Odelin. Evaporative cooling of a guided rubidium atomic beam. *Phys. Rev. A*, 72(033411):33411 – 1, September 2005. ISSN 1050-2947.

[12] T. Lahaye, J. M. Vogels, K. J. Günter, Z. Wang, J. Dalibard, and D. Guéry-Odelin. Realization of a magnetically guided atomic beam in the collisional regime. *Phys. Rev. Lett.*, 93(093003), August 2004.

[13] J. M. Vogels, T. Lahaye, C. F. Roos, J. Dalibard, and D. Guéry-Odelin. How to reach the collisional regime on a magnetically guided atomic beam. *Journal de Physique IV*, 116:259–264, October 2004.

[14] K. I. Lee, J. A. Kim, H. R. Noh, and W. Jhe. Single-beam atom trap in a pyramidal and conical hollow mirror. *Opt. Lett.*, 21(15):1177–1179, August 1996.

[15] E. L. Raab, M. Prentiss, Alex Cable, Steven Chu, and D. E. Pritchard. Trapping of neutral sodium atoms with radiation pressure. *Phys. Rev. Lett.*, 59(23):2631–2634, December 1987.

[16] R. S. Williamson III, P. A. Voytas, R. T. Newell, and T Walker. A magneto-optical trap loaded from a pyramidal funnel. *Opt. Exp.*, 3(3):111–117, August 1998.

[17] Z. T. Lu, K. L. Corwin, M. J. Renn, M. H. Anderson, E. A. Cornell, and C. E. Wieman. Low-velocity intense source of atoms from a magneto-optical trap. *Phys. Rev. Lett.*, 77(16): 3331, Oct 1996.

[18] S. Weyers, E. Aucouturier, C. Valentin, and N. Dimarcq. A continuous beam of cold cesium atoms extracted from a two-dimensional magneto-optical trap. *Opt. Comm.*, 143:30, 1997.

[19] K. Dieckmann, R. J. C. Spreeuw, M. Weidemüller, and J. T. M. Walraven. Two-dimensional magneto-optical trap as a source of slow atoms. *Phys. Rev. A*, 58:3891, 1998.

[20] P. Berthoud, A. Joyet, G. Dudle, N. Sagna, and P. Thomann. A continuous beam of slow, cold cesium atoms magnetically extracted from a 2d magneto-optical trap. *Europhys. Lett.*, 41(2): 141, 1998.

[21] P. Berthoud, E. Fretel, and P. Thomann. Bright, slow, and continuous beam of laser-cooled cesium atoms. *Phys. Rev. A*, 60:R4241, 1999.

[22] J. Schoser, A. Batär, R. Löw, V. Schweikhard, A. Grabowski, Yu. B. Ovchinnikov, and T. Pfau. Intense source of cold rb atoms from a pure two-dimensional magneto-optical trap. *Phys. Rev. A*, 66(023410), 2002.

[23] B. K. Teo, T. Cubel, and G. Raithel. A slow and dark atom beam. *Opt. Comm.*, 212:307–315, 2002.

[24] B. K. Teo and G. Raithel. Loading mechanism for atomic guides. *Phys. Rev. A*, 63:031402(R), 2001.

[25] B. K. Teo and G. Raithel. Atom reflection in a tapered magnetic guide. *Phys. Rev. A*, 65: 051401(R), 2002.

[26] K. E. Gibble, S. Kasapi, and S. Chu. Improved magneto-optic trapping in a vapor cell. *Opt. Lett.*, 17:526–528, apr 1992.

[27] Johannes Schuster. *Stosslawinen in einem Bose-Einstein-Kondensat*. PhD thesis, Universität Konstanz, 2002.

[28] Spencer Eugene Olson, Rahul Ramdas Mhaskar, and Georg Raithel. Continuous propagation and energy filtering of a cold atomic beam in a long high-gradient magnetic atom guide. *Phys. Rev. A*, 73(3):033622, March 2006. URL `http://link.aps.org/abstract/PRA/v73/e033622`.

[29] R. Dum, P. Zoller, and H. Ritsch. Monte carlo simulation of the atomic master equation for spontaneous emission. *Phys. Rev. A*, 45:4879–4887, apr 1992. doi: 10.1103/PhysRevA.45.4879.

[30] William D. Phillips and Harold Metcalf. Laser deceleration of an atomic beam. *Phys. Rev. Lett.*, 48(9):596–599, Mar 1982. doi: 10.1103/PhysRevLett.48.596.

[31] W. Ertmer, R Blatt, J. L. Hall, and M Zhu. Laser manipulation of atomic beam velocities: demonstration of stopped atoms and velocity reversal. *Phys. Rev. Lett.*, 54(10):966–999, Mar 1985.

[32] R. Gaggl, L. Windholz, C. Umfer, and C. Neureiter. Laser cooling of a sodium atomic beam using the stark effect. *Phys. Rev. A*, 49(2):1119–1121, Feb 1994. doi: 10.1103/PhysRevA.49.1119.

[33] John Prodan, Alan Migdall, William D. Phillips, Ivan So, Harold Metcalf, and Jean Dalibard. Stopping atoms with laser light. *Phys. Rev. Lett.*, 54(10):992–995, Mar 1985. doi: 10.1103/PhysRevLett.54.992.

[34] Thomas E. Barrett, Samuel W. Dapore-Schwartz, Mark D. Ray, and Gregory P. Lafyatis. Slowing atoms with σ^- polarized light. *Phys. Rev. Lett.*, 67(25):3483–3486, Dec 1991.

[35] V. S. Bagnato, A. Aspect, and S. C. Zilio. Study of laser deceleration of an atomic beam by monitoring the fluorescence along the deceleration path. *Opt. Comm.*, 72(1,2):76–81, Jul 1989.

[36] John David Jackson. *Classical Electrodynamics, Third Edition*. John Wiley & Sons, Inc., 1998.

[37] R. D. Swenumson and Even U. Continuous flow reflux oven as the source of an effusive molecular cs beam. *Rev. Sci. Instrum.*, 52(4):559–561, 1981. doi: 10.1063/1.1136639.

[38] Frederick Reif. *Fundamentals of Statistical and Thermal Physics*. McGraw-Hill Science, 1965.

[39] Christopher Slowe, Laurent Vernac, and Lene Vestergaard Hau. High flux source of cold rubidium atoms. *Rev. Sci. Instrum.*, 76(10):103101, 2005. doi: 10.1063/1.2069651. URL `http://link.aip.org/link/?RSI/76/103101/1`.

[40] Igor Lesanovsky, Jörg Schmiedmayer, and Peter Schmelcher. Rydberg atoms in a magnetic guide. *Phys. Rev. A*, 70(4):043409, Oct 2004.

[41] I. Lesanovsky, J. Schmiedmayer, and P. Schmelcher. Rydberg atoms in magnetic quadrupole traps. *Europhys. Lett.*, 65:478–484, Feb 2004.

[42] Igor Lesanovsky, Jörg Schmiedmayer, and Peter Schmelcher. Electronic structure of atoms in magnetic quadrupole traps. *Phys. Rev. A*, 69(5):053405, May 2004.

[43] S. K. Dutta, D. Feldbaum, A. Walz-Flannigan, J. R. Guest, and G. Raithel. High-angular-momentum states in cold rydberg gases. *Phys. Rev. Lett.*, 86(18):3993–3996, Apr 2001.

[44] Harald Friedrich. *Theoretical Atomic Physics*. Springer; 3rd ed. edition, 2005.

[45] A. Walz-Flannigan, J. R. Guest, J.-H. Choi, and G. Raithel. Cold rydberg gas. *Phys. Rev. A*, 69(6):063405, Jun 2004.

[46] Alisa Walz-Flannigan. *Cold Rydberg gas dynamics*. PhD thesis, University of Michigan, 2004.

[47] Thomas Gallagher. *Rydberg Atoms*. Cambridge University Press, 2005.

[48] D. M. Harber, J.M. McGuirk, J. M. Obrecht, and Cornell E. A. Thermally induced losses in ultra-cold atoms magnetically trapped near room-temperature surfaces. *J. of Low Temp. Phys.*, 133(3-4):229–238, Nov 2003.

[49] E. Mandonnet, A. Minguzzi, R. Dum, I. Carusotto, Y. Castin, and J. Dalibard. Evaporative cooling of an atomic beam. *Euro. Phys. JD*, 10(1):9–18, March 2000.

[50] Bulletin of the Research Corporation, Winter Issue, 1999.